PROPERTIES OF THE COLOR-MAGNITUDE DIAGRAMS OF TYPE IA SUPERNOVAE

A Thesis

by

LAUREN NICOLE ALDOROTY

Submitted to the Graduate and Professional School of
Texas A&M University
in partial fulfillment of the requirements for the degree of

DOCTOR OF PHILOSOPHY

Chair of Committee,	Lifan Wang
Committee Members,	Nicholas Suntzeff
	Peter Brown
	Elaine Oran
Head of Department,	Grigory Rogachev

May 2023

Major Subject: Astronomy

ABSTRACT

Type Ia Supernovae (SNe Ia) are the most precise distance indicators available for cosmological studies. Utilizing this characteristic in analysis led to the discovery of dark energy and the accelerated expansion of the Universe, and SNe Ia continue to be crucial for understanding modern cosmology. However, there are systematic uncertainties associated with SNe Ia that prevent use of these powerful tools to their full potential. The scatter observed in their standardized magnitudes is larger than can be explained by current knowledge. For example, it is difficult to separate the reddening effects of dust from SN Ia intrinsic color. Upcoming surveys like LSST and *Roman* will discover an unprecedented number of SNe Ia, shrinking the statistical contribution such that systematic error vastly outweighs statistics. In order to be prepared for these data, it is crucial that sources of systematic error in SN Ia standardization are better understood.

This dissertation concerns the variability among SNe Ia. This includes observational variability, the physical implications of these variations, and their effects on SN Ia cosmology. We find that the "bump" feature of the color-magnitude diagram (CMAGIC) diagram of SNe Ia is strongly correlated with the slope of the subsequent linear region. In addition, the slope and bump feature are correlated with both photometric and spectral parameters that are associated with decline rate. This result may be associated with chemical mixing due to large-scale Rayleigh-Taylor instabilities at the Si/Ni boundary. A preliminary Hubble residual analysis is described, which shows that these features may need to be considered in order to ensure a uniform sample for cosmological studies.

Chapter 2 describes the data used in this work, namely, the Nearby Supernova Factory (SNfactory) spectrophotometric dataset. Chapter 3 describes the analytical procedures used in this work. This includes both photometric and spectroscopic techniques. We focus on color-magnitude intercept calibration (CMAGIC) methods, introduced in Section 1.3, to quantify some aspects of SN Ia diversity. Chapter 4 discusses the results of the analyses

described in Chapter 3. CMAGIC-based diversity is discussed in terms of supernova physics, as well as cosmology. Finally, Chapter 5 summarizes the key results of this work, and recommendations for future work are detailed.

DEDICATION

For my dad, who might be a bigger nerd than I am, and for my mom, who loves us both anyway.

ACKNOWLEDGMENTS

This was a really wild time to be in graduate school, with 2020 happening in the middle of it all and whatnot. I don't know that I'd repeat doing something like this during a global pandemic/major political upheaval (but I also don't regret it), but I survived, and there are a lot of people to whom I owe gratitude for that.

Thank you to my scientific collaborators for their contributions to this work. Thanks to Nick Suntzeff for "rehoming" me when I wanted to switch research groups, Lifan Wang for accepting a surprise student, and Peter Brown for all the helpful discussions and answers to many questions. I would especially like to thank Jiawen Yang, whose analytical expertise, kindness, and friendship were indispensable. The support of my fellow TAMU Astronomy graduate students was irreplacable and uniquely valuable. I feel lucky to have ended up in a group of graduate students who actively foster such a healthy, supportive culture amongst themselves.

I love all of my friends to death, and I'm grateful for every single one of you. It feels unfair to choose a list of people, so if you're reading this and think "hey, that's me," then it's about you. However, I'd like to name *one* person. There aren't enough words to thank Tarini Konchady, who was an amazing friend and roommate all the way from the beginning of undergrad through grad school, and I'm sure she will be far beyond, as well. You're a beautiful, talented, brilliant, powerful musk-ox. Thank you to my Pearl Bar family, especially Ian, for giving me a reason to want to physically be in Texas when I felt like I had no reason to be here any more. Also, shoutout to my brother, whose promise/threat to read this wretched document has rendered my statements that "no one will ever read my dissertation" to be false.

Last, but certainly not least, Dips: sorry there is no discussion of aliens in this thesis.

CONTRIBUTORS AND FUNDING SOURCES

Contributors

This work was supported by a dissertation committee consisting of Prof. Lifan Wang (chair), Prof. Nicholas Suntzeff, and Dr. Peter Brown of the Department of Physics & Astronomy; as well as Prof. Elaine Oran of the Department of Aerospace Engineering.

The data analyzed in this work were provided by the Nearby Supernova Factory (SNfactory) collaboration.

The one-dimensional delayed-detonation simulation in Section 4.4 was completed by Dr. Peter Hoeflich of Florida State University's Department of Physics.

All other work conducted for this dissertation was completed by the student independently.

Funding Sources

Graduate study was supported by the Texas A&M University Dr. Dionel Avilés '53 and Dr. James Johnson '67 Fellowship Program (previously known as the Graduate Diversity Excellence Fellowship), the NASA Texas Space Grant Consortium Graduate Fellowship, NSF grant AST-1613455, and the Mitchell Institute for Fundamental Physics and Astrophysics.

The Nearby Supernova Factory was supported in part by the Director, Office of Science, Office of High Energy Physics of the U.S. Department of Energy under Contract No. DE-AC02-05CH11231. Support in France was provided by CNRS/IN2P3, CNRS/INSU, and PNC and French state funds managed by the National Research Agency within the Investissements d'Avenir program under grant reference numbers ANR-10-LABX-0066, ANR-11-IDEX-0004-02 and ANR-11-IDEX-0007. Additional support comes from the European Research Council (ERC) under the European Union's Horizon 2020 research and innovation program (grant agreement No 759194-USNAC). Support in Germany was provided by DFG through TRR33 "The Dark Universe" and by DLR through grants FKZ 50OR1503 and FKZ

50OR1602. In China support was provided from Tsinghua University 985 grant and NSFC grant No 11173017. Some results were obtained using resources and support from the National Energy Research Scientific Computing Center, supported by the Director, Office of Science, Office of Advanced Scientific Computing Research of the U.S. Department of Energy under Contract No. DE-AC02-05CH11231.

NOMENCLATURE

ΛCDM	Lambda-cold dark matter
BL	Broad line (Branch classification [1])
CMAGIC	Color-Magnitude Intercept Calibration
CL	Cool (Branch classification [1])
CN	Core normal (Branch classification [1])
DD	Double degenerate
DDT	Delayed-detonation
FLRW	Friedmann-Lemaître-Robertson-Walker
fPCA	Functional principal component analysis
IFS	Integral field spectrograph
IME	Intermediate mass element
LSST	Legacy Survey of Space and Time
MCMC	Markov chain Monte Carlo
MLE	Maximum likelihood estimation
PC	Principal component
pEW	Pseudo-equivalent width
RMS	Root mean square
SD	Single degenerate
SALT	Spectral Adaptive Light-curve Template
SED	Spectral energy distribution
SN, SNe	Supernova (singular), supernovae (plural)
SN(e) Ia	Type Ia Supernova(e)

SNIFS	SuperNova Integral Field Spectrograph
SNfactory	Nearby Supernova Factory
SS	Shallow silicon (Branch classification [1])
SUGAR	SUpernova Generator And Reconstructor
WD	White Dwarf
WRMS	Weighted root mean square

TABLE OF CONTENTS

Page

LIST OF FIGURES

FIGURE Page

LIST OF TABLES

TABLE Page

1. INTRODUCTION

A supernova (SN, pluralized as "supernovae", or SNe) is the explosion of a star at the end of its lifetime. They are among the most energetic events in the known Universe, and can be brighter than the total brightness of the host galaxy in which they reside. As a SN explodes and material propagates outward, its innermost material becomes visible to observers, providing a window into stellar interiors. They are a star's final contribution to the elemental content of the Universe—as the explosion's shockwave travels through the ejected material, it kickstarts nucleosynthesis and produces elements heavier than Fe, which could not otherwise be produced by nucleosynthesis in the interior of a main sequence star. It is impossible to understand the elemental abundances in the Universe without understanding SNe.

There are two ways a supernova can occur: via a thermonuclear explosion or core-collapse. Core-collapse SNe are the result of insufficient nuclear burning in the cores of massive stars. Once elements have been fused to Fe, there is insufficient energy to continue fusion. Thus, there is also insufficient energy support the star's mass against gravity. The star collapses and the material bounces off itself once it cannot collapse any further, causing a core-collapse supernova.

Type Ia Supernovae (SNe Ia) are thermonuclear runaway explosions that originate in a stellar binary system in which at least one of the members of the system is a white dwarf (WD). A WD gains mass from either a degenerate or non-degenerate companion star, and becomes too massive for electron degeneracy pressure to support it against gravity [15]. The material is compressed and heats rapidly, re-igniting thermonuclear reactions in the previously-inert WD.

SNe Ia are of interest to astronomical studies due to their brightness and standardizability [16, 17, 11, 18, 19]. Except for superluminous SNe, they are the brightest type of SN; this allows them to be seen at further distances than their dimmer relatives. The combination of

these two attributes makes them excellent distance indicators. Utilizing these characteristics in analysis led to the discovery of dark energy and the accelerated expansion of the Universe [20, 21], and SNe Ia remain the most precise distance indicator to date.

Broadly, this dissertation concerns the variability among SNe Ia. This includes observational variability, the physical implications of these variations, and their effects on SN Ia cosmology. This work uses color-magnitude intercept calibration (CMAGIC) methods, introduced in Section 1.3, to quantify some aspects of SN Ia diversity. This CMAGIC-based diversity is discussed in terms of supernova physics, as well as cosmology. Finally, recommendations for future work are detailed.

1.1 Type Ia Supernovae

1.1.1 Progenitors and Explosion Mechanisms

SNe Ia are the result of a thermonuclear explosion of a carbon-oxygen (CO) white dwarf (WD) in a binary system. SN Ia light curves tend to be similar because of the limited composition of their progenitors, as well as the rigid mass value at which electron degeneracy pressure fails (Chandrasekhar mass).

However, there *is* some observed variation among SNe Ia. Its companion may be another WD (degenerate), or any star that isn't a WD (nondegenerate). If the companion star is not degenerate, it is said that the SN has a "single degenerate progenitor" (SD). If the companion star is a WD, it has a "double degenerate progenitor" (DD). The rates of SNe Ia as a result of each of these progenitor scenarios is currently an open question.

1.1.2 Light Curves and Photometric Analysis of Type Ia Supernovae

1.1.2.1 Theory

Bolometric light curves of SNe Ia are primarily driven by radioactive decay of ^{56}Ni [22, 23, 24]. As the initial shock propagates outward, ^{56}Ni is synthesized and decays following

the channels

$$^{56}\text{Ni} + e^- \rightarrow ^{56}\text{Co} + \gamma + \nu_e \tag{1.1}$$

$$^{56}\text{Co} + e^- \rightarrow ^{56}\text{Fe} + \gamma + \nu_e \tag{1.2}$$

$$^{56}\text{Co} \rightarrow ^{56}\text{Fe} + e^+ + \gamma + \nu_e, \tag{1.3}$$

where Equation 1.2 occurs for 81% of ^{56}Co decays and Equation 1.3 represents the remainder of ^{56}Co decay [25]. Energy from these decays heats the expanding material, resulting in thermal radiation and an observable explosion. Further, because the rate of energy released from the decay of ^{56}Ni at peak brightness is equal to the luminosity at that time, the quantity of ^{56}Ni in a given SN Ia can be estimated given a bolometric luminosity at maximum brightness [22, 23, 24, 25].

1.1.2.2 Light curve width and decline rate

Light curve width, which is approximately synonymous with "decline rate", is a crucial parameter for classification of SNe Ia. The decline rate in magnitudes was first defined as β, described the rate of brightness decrease between $B-$band maximum brightness and the change in the slope of the light curve that occurs approximately 30 days after this time [17]. This work paved the way for the parameter Δm_{15} [11]. Δm_{15} describes the change in magnitude between maximum brightness in the $B-$band and 15 days later, rather than a rate of dimming. There is also a relationship between Δm_{15} and the peak luminosity of the supernova—as Δm_{15} increases, the maximum brightness of the supernova decreases [11]. This relationship has been successfully reproduced with models, showing that ^{56}Ni mass is the primary contributor to the width-luminosity correlation [26].

Other parameters have been developed to quantify the light curve width, including the SALT stretch x_1 [27, 28, 3], color-stretch s_{BV} [10], and other statistically-developed quantities [9].

1.1.3 Reddening and Extinction

Reddening and extinction both describe the observable effect of light scattering off dust. Extinction describes the dimming that results, and reddening describes the preferential scattering of bluer light (i.e., shorter wavelengths). In optical wavelengths, the intensity of scattering $I_{scattering} \propto \lambda^{-1}$, reflecting this preferential scattering of shorter wavelengths.

Extinction is described by the equation:

$$A_V = -2.5 \log \frac{F_V}{F_{V,0}}, \tag{1.4}$$

where the subscript V indicates the V-band photometric bandpass, F_V is observed flux in the V-band, and $F_{V,0}$ is the intrinsic flux in the V-band.

Reddening is described by:

$$E(B-V) = (B-V)_{observed} - (B-V)_{intrinsic}, \tag{1.5}$$

where $(B-V)_{observed}$ is the observed $B-V$ photometric color, and $(B-V)_{intrinsic}$ is the intrinsic photometric color. $E(B-V)$ may also be called the "color excess" of an object. Extinction and reddening can be linked via an equation, as well:

$$E(B-V) = A_B - A_V, \tag{1.6}$$

where A_B is photometric extinction in the B-band and A_V is photometric extinction in the V-band. They can also be related to each other as:

$$A_V = R_V E(B-V), \tag{1.7}$$

where R_V is a constant called the "total-to-selective extinction ratio". R_V is correlated with the average size of dust grains—dust grains tend to scatter light with a wavelength

similar to their own size. In terms of photometric observations, R_V roughly quantifies the amount of expected light loss in a particular photometric band.

1.1.3.1 Quantifying Host Galaxy Reddening

Because SN Ia cosmology relies on standardizing a diverse population, it is crucial that the effects of dust on observable quantities are understood. This becomes more crucial as more SNe are discovered and their diversity becomes more apparent. For example, it has been shown that the mass and metallicity of the progenitor WD can affect the intrinsic color in $(B-V)$ by approximately 0.1 magnitudes [8]. Thus, reddening must be quantified robustly in order to access their intrinsic colors. Galactic dust reddening is generally well-measured [29], however, it is more difficult to quantify the effects of dust from other galaxies.

An early method of calculating the color excess used the $(B-V)$ color curves during the time period from $\sim 30-90$ days after maximum brightness [30]. During this time region, the color curves are extremely similar, but have a vertical offset. Because reddening can only make objects redder, it can be assumed that there is a "blue floor" where observed color reflects the intrinsic color of a given supernova. Thus, the vertical offset between the "blue floor" and a color curve is the calculated color excess. This method was expanded upon by including a calibration to the decline rate Δm_{15} [31] (Section 1.1.2.2).

Spectral features (Section 1.1.4) are useful because they can be used to break degeneracies between intrinsic properties and dust effects. For example, it has been shown that the pEW of the Si II λ4131Å feature is highly correlated with light curve width [32, 33], and thus can be used to derive extinction laws [34].

1.1.4 Spectroscopic Analysis of Type Ia Supernovae

SN spectra consist of both emission and absorption lines. The emission lines appear at the rest-frame wavelength of the transition in the SN's frame of reference. The absorption lines are blueshifted because the expanding ejecta material moves toward the observer along the line-of-sight. Due to the plethora of emission and absorption lines coupled with different

blueshifts, in addition to Doppler broadening of all features, it is difficult, if not impossible, to determine the location of the continuum in a SN spectrum.

In general, SNe are classified spectroscopically. SNe that show Hydrogen lines in their spectra at times near maximum brightness are Type I SNe, while SNe that do not have H in their spectra are Type II. All SN types are core collapse SNe, except for SNe Ia, which are thermonuclear explosions of a white dwarf (WD). SNe Ia show strong Si absorption features at 6355 Å and 5972 Å. It is important to note that these features do not appear in the spectra at these rest wavelengths; they appear near 6100 Å and 5750 Å, respectively. This is due to Doppler shifting of the light from the ejecta velocity traveling toward the observer.

As the explosion expands, the photosphere recedes and the observer is able to peer deeper into the ejecta, providing the observer with a view of the elemental content of the different layers of the SN. Fe-group elements are important to understand due to the fact that the luminosity of SNe Ia is primarily driven by radioactive ^{56}Ni decay [22, 23, 24]. Intermediate mass elements (IMEs), such as S and Si, are also of interest because they are in the reaction chain that leads to the synthesis of ^{56}Ni.

1.1.4.1 Absorption line strength and pseudo-equivalent width

The strength of SN absorption lines is usually quantified by measuring their pseudo-equivalent width (pEW). Unlike other objects, which have a clearly-distinguishable continuum in their spectra, there is currently no defined spectral energy distribution (SED) that describes the continuum component of a SN spectrum. Therefore, the equivalent width cannot be measured directly. Instead, a local "pseudo-continuum" is defined—for a small region surrounding an absorption line, a line segment can be taken to be an approximation to the local continuum. The absorption line is normalized to the chosen pseudo-continuum, and the area inside the normalized absorption feature is measured, resulting in a quantification of line strength (pEW) for that spectral line [35]. Sometimes, instead of integrating over the line, the center of the absorption feature (its minimum) is located and the distance between the pseudo-continuum and the minimum serves as a quantification of the spectral line

strength [4, 5]. A ratio of line strengths may also be defined as the ratio of the flux value at a peak or minimum to the flux at another peak or minimum [4, 36].

The strengths of the Si II λ6355 and λ5972 absorption features at maximum brightness have been used to describe the "Branch subtypes", which consist of "core-normal" (CN), "shallow silicon" (SS), "broad line" (BL), and "cool" (CL) classifications [1]. When these line strengths are plotted against each other, SNe tend to group into these four subtypes. These groups tend to have similar spectral features outside of the aforementioned Si II lines.

The strengths of the Si II absorption features are correlated with light curve decline rate [4, 5, 6]. In general, as Si II features weaken, the light curve decline rate $\Delta m_{15,B}$ also decreases. These bright, slowly-declining SNe tend to have weaker lines partially due to the effects of their higher temperature on spectral features. In particular, the pEW of Si II λ5972 and the ratio of the strengths of the two discussed Si II features at maximum brightness, R(Si II)$_{max}$, increase as $\Delta m_{15,B}$ increases [4, 5, 6]. The Si II λ6355 line strength is similarly correlated with $\Delta m_{15,B}$, however, the relationship is not as strong [6]. The blended Si II/Ni II feature at 4000Å has also been found to be associated with $\Delta m_{15,B}$, ^{56}Ni mass, as well as the SALT stretch parameter x_1 [32, 33, 36].

1.1.4.2 Line velocity

The ejecta expansion velocity can be measured using the observed central wavelength of a given absorption feature, the known rest frame wavelength of the feature, and Doppler shift. Typical expansion velocities of Si II lines measured at maximum brightness are around 11000 km s^{-1} for normal SNe Ia [7]. Si II λ6355 line velocity can be used to identify SN Ia subtypes similarly to the Branch subtypes. If the pEW and velocity of this line are plotted against each other for a sample of SNe Ia, they naturally separate into groups, with a notable $\gtrsim$ 12000 km s^{-1} cutoff for fast-declining SNe (91bg-like) [7]. Additionally, these fast-declining SNe with high ejecta velocity measured from the Si II λ6355 absorption feature tend to be redder than normal SNe Ia, and excluding them from cosmology samples reduces the scatter of the Hubble residual [7, 37, 38].

1.2 Cosmology

1.2.1 Overview

Cosmology is the study of the nature of the Universe on large scales. The goal of cosmological studies are to understand the origin of the Universe, how it changes through time, why it has the properties it has, and how it might end. The current popular model describing the Universe is the Lambda-cold dark matter (ΛCDM) model. In addition to normal baryonic matter, this model states that the Universe contains cold dark matter (CDM) and dark energy. The dark energy is described by a "cosmological constant", denoted by Λ.

ΛCDM assumes the Universe is both homogeneous (everywhere is the same) and isotropic (it is the same in every direction). In other words, no matter where an observer is positioned in the Universe, the observer will always deduce the same information about the Universe. Mathematically, the Friedmann-Lemaître-Robertson-Walker (FLRW) metric describes this as

$$ds^2 = c^2dt^2 - a(t)^2\Big(\frac{dr^2}{1-kr^2} + r^2(d\theta^2 + \sin^2\theta d\phi^2)\Big), \tag{1.8}$$

where c is the speed of light, t is time, $a(t)$ is the cosmological scale factor, and (r, θ, ϕ) represent comoving spherical coordinates. k indicates curvature; $k < 0$ means negative curvature, $k = 0$ means zero curvature, and $k > 0$ means positive curvature. Currently, the Universe is believed to be flat (i.e., $k = 0$).

Λ enters the picture because the FLRW metric, expressed as a diagonal matrix, can be used to solve Einstein's field equations with a cosmological constant:

$$G_{\mu\nu} + \Lambda g_{\mu\nu} = \frac{8\pi G}{c^4} T_{\mu\nu}, \tag{1.9}$$

where $G_{\mu\nu}$ is the Einstein tensor, $g_{\mu\nu}$ is the metric tensor (in this case, the FLRW metric expressed as a matrix), $T_{\mu\nu}$ is the stress-energy tensor, and G is the Newtonian gravitational

constant. The solutions are the Friedmann equations,

$$H(t)^2 \equiv \left(\frac{\dot{a}}{a}\right)^2 = \frac{8\pi G\rho}{3} - \frac{kc^2}{a^2} + \frac{\Lambda c^2}{3} \tag{1.10}$$

$$\frac{\ddot{a}}{a} = -\frac{4\pi G}{3}\left(\rho + \frac{3p}{c^2}\right) + \frac{\Lambda c^2}{3}, \tag{1.11}$$

where $H(t)$ is the Hubble parameter, p is pressure, and ρ is mass density of the Universe. ρ and p are related to each other by the equation of state of a perfect fluid,

$$p = w\rho c^2, \tag{1.12}$$

where w is dimensionless. Dots above characters indicate time derivatives.

Assuming a flat Universe ($k = 0$), equations 1.10 and 1.11 can be combined and rewritten as

$$\dot{\rho} + 3H(t)\left(\rho + \frac{p}{c^2}\right) = 0. \tag{1.13}$$

Using Equation 1.12, this can be rewritten as

$$\frac{d\rho}{\rho} = -3\frac{da}{a}(1 + w), \tag{1.14}$$

which, if integrated assuming a constant w, implies that

$$\rho \propto a^{-3(1+w)}. \tag{1.15}$$

The "fluid" in the Universe that these equations describe can be either matter, radiation, or the cosmological constant. To make this expression constant, $w = -1$. Therefore, if dark energy is described by a cosmological constant, experimental evidence must show $w = -1$[1]. For matter, $w = 0$ and $\rho_m \propto a^{-3}$; for radiation, $w = 1/3$ and $\rho_r \propto a^{-4}$. Therefore, a solution

[1]For accelerated expansion, but not necessarily a cosmological constant, $w < -1/3$.

for $\rho(a)$ is

$$\rho(a) = \rho_m a^{-3} + \rho_r a^{-4} + \rho_\Lambda, \tag{1.16}$$

where ρ_i are constants with density units.

We can also derive a critical density ρ_c, which is the current density of the Universe. This value will be used to change the density units of the ρ_i in Equation 1.16 so they are dimensionless. Using Equation 1.10 with $k = 0$ and $\Lambda = 0$,

$$\rho_c = \frac{3H_0^2}{8\pi G}, \tag{1.17}$$

where H_0 is the Hubble constant, or the value of $H(t)$ today. Equation 1.16 is divided by ρ_c such that $\Omega_i = \rho_i/\rho_c$, and the result is

$$H(t) = H_0\sqrt{\Omega_m a^{-3} + \Omega_r a^{-4} + \Omega_\Lambda}. \tag{1.18}$$

However, it is difficult to make practical measurements in terms of the scale factor $a(t)$. Starting with the FLRW metric (Equation 1.8) and setting $\theta = \phi = 0$, in combination with Doppler shift, the cosmological redshift z can be derived:

$$1 + z = \frac{a_0}{a(t)}, \tag{1.19}$$

where $a_0 = 1$ is the scale factor at the current time. Then, Equation 1.18 can be rewritten in terms of z:

$$H(z) = H_0\sqrt{\Omega_m(1+z)^{-3} + \Omega_r(1+z)^{-4} + \Omega_\Lambda}. \tag{1.20}$$

This is still not immediately useful for application to observations without more derivations. Ultimately, what we are able to observe directly is the flux coming from an astronomical object,

$$F = \frac{L}{4\pi d_L^2}, \tag{1.21}$$

where L is luminosity and d_L is luminosity distance. However, in order to calculate the luminosity distance, we need the *comoving distance*, which is the distance between two objects with the expansion of the Universe removed.

Starting with the fact that distance = rate $\times$ time, we can take the "rate" to be the speed of light c, and the time to be the reciprocal of Equation 1.20. Then, we integrate over redshift z:

$$d_C = \frac{c}{H_0} \int_0^z \frac{dz}{\sqrt{\Omega_m(1+z)^{-3} + \Omega_r(1+z)^{-4} + \Omega_\Lambda}}. \tag{1.22}$$

However, luminosity distance d_L is the distance as derived from observation, which includes z. Then, accounting for the expansion of a flat universe,

$$d_L = (1+z)d_C. \tag{1.23}$$

Finally, we define the distance modulus μ and relate these quantities to "observers' units" in magnitudes:

$$\mu \equiv 5 \log \left(\frac{d_L}{10\text{pc}} \right) = m - M - k, \tag{1.24}$$

where m is the apparent magnitude of an object, M is the absolute magnitude, and k is the $k-$correction term. This term accounts for the fact that redshift affects the observer-frame brightness of an object due to its spectral features shifting in or out of a photometric filter.

1.2.2 Type Ia Supernova Cosmology

SNe Ia are the most precise experimental cosmological distance indicator available. Although they are not all identical, and cannot be called "standard" candles, they are highly "standardizable" due to the luminosity-decline rate relationship discussed in Section 1.1.2.2. Very precise Hubble diagrams have been made using only color and decline rate corrections [20, 39, 21, 40, 41, 42]. Typically, these use the Tripp distance modulus relationship [12, 13],

or a modified version of it,

$$\mu_{Tripp} = m_B - (-19.48 + b(\Delta m_{15} - 1.05) + R_B(B - V)). \tag{1.25}$$

Current distance modulus models usually allow the parameter M to vary as a fit parameter rather than fixing it at -19.48, and 1.1 has replaced 1.05 as the accepted average value of Δm_{15}. A commonly-used variation on this model is the SALT distance modulus formalism, which modifies the two-parameter Tripp model to replace Δm_{15} and $(B-V)$ with the SALT parameters x_1 and c, respectively:

$$\mu_{SALT} = m_B - M + \alpha x_1 - \beta c. \tag{1.26}$$

However, these models can be improved if spectral information is considered as well [7, 43, 37, 33, 44]. Spectral features are useful because they can be used to break degeneracies between intrinsic properties and dust effects. For example, it has been shown that the pEW of the Si II λ4131Å feature is highly correlated with light curve width [32, 33], and thus can be used to derive extinction laws [34]. The Hubble residual can also be reduced if peculiar velocity is accounted for [45, 46].

Efforts have been made to use unusual SNe for standardization. For example, if it can be shown that 1991T/1999aa-like objects can be used for standardization as successfully as "normal" SNe Ia, then these objects that will be over-represented in higher-z samples due to their brightness allow extension of the cosmological distance ladder [47, 48]. However, the results do not currently meet the accepted standards established by the use of normal SNe Ia.

1.3 Color-Magnitude Intercept Calibration

The color-magnitude intercept calibration (CMAGIC) method standardizes magnitudes at a constant color rather than at maximum brightness [49]. About one week after maximum

brightness in the $B-$band, the color-magnitude diagram (CMAGIC diagram) for normal-bright SNe Ia (i.e., neither subluminous nor overluminous) displays a remarkably linear relationship in the rest-frame B magnitude versus $B-V$, $B-R$, and $B-I$ colors. This lasts for approximately two weeks. The slope of this region, B_{XY}, is independent from other measurable quantities. Thus, we can use this property to accurately calibrate SNe Ia independently of other methods with sensitivity to different systematic sources of error. It has been shown that CMAGIC curves may be useful in breaking the degeneracies between intrinsic color and reddening. Specifically, the location of its distinguishing features are affected by the central density of the progenitors and explosion mechanism [8].

The slope of the linear region is defined as

$$B = B_{BX} + \beta_{BX}(B - X), \tag{1.27}$$

where β_{BX} is the slope of the linear region, B_{BX} is the intercept of the fit line, and X represents an arbitrary photometric filter (V, R, or I) [49]. Additionally, B_{BX} is the magnitude to be standardized for cosmological application, rather than maximum brightness. Special attention must be paid to B_{BX} because it is not simply the intercept found by a direct linear fit to the CMAGIC diagram. As an error-reducing measure, before fitting the linear region, the CMAGIC diagram is shifted by 0.6 mag to the left (0.6 is approximately the mean $B-V$ color in the linear region) before being shifted back to its "correct" location. This results in a fit value for an intercept at $B-X=0.6$, called $B_{BX0.6}$. Thus, the intercept values are originally defined as:

$$B_{BX} \equiv B_{BX0.6} - \langle \beta_{BX} \rangle \times 0.6 \text{ mag}, \tag{1.28}$$

where the angled brackets represent the average over the entire sample [49].

There is also a second linear region, which occurs between 30-60 days after maximum $B-$band brightness. This is visible in the left panel of Figure 3.1, where the SN can be seen

dimming and becoming bluer after the data point at 34.2 days.

The extinction corrections for the $BVRI$ filter set are

$$A_{BV} = (R_B - \beta_{BV})E(B-V) \tag{1.29a}$$

$$A_{BR} = R_B E(B-V) - \beta_{BR}E(B-R) \tag{1.29b}$$

$$A_{BI} = R_B E(B-V) - \beta_{BI}E(B-I) \tag{1.29c}$$

where R_B is the total-to-selective extinction ratio for the B-band [49].

It is worth noting that if $R_B \approx \beta_{BV}$, then B_{BV} is an extinction-free quantity. Further, we can derive a correction to B_{max} using the quantities defined by the CMAGIC linear fit in order to circumvent the use of $E(B-V)$ or A_{BV} entirely. If an extinction-free magnitude, B_{EF}, is given by

$$B_{EF} = B_{BV} - A_{BV} \tag{1.30}$$

We replace A_{BV} using Equation 1.29a:

$$B_{EF} = B_{BV} - (R_B - \beta_{BV})E(B-V) \tag{1.31}$$

Then, we assume that

$$\beta_{BV} = \frac{\Delta B}{\Delta(B-V)} \approx \frac{B_{max} - B_{BV}}{\beta_{BV}}, \tag{1.32}$$

and can then express the extinction-free magnitude B_{EF} in terms of measurable quantities as

$$B_{EF} = B_{BV} - \frac{(R_B - \beta_{BV})(B_{max} - B_{BV})}{\beta_{BV}}. \tag{1.33}$$

1.3.1 CMAGIC diagram variability

The CMAGIC diagram reveals features and relationships that are not visible on light curves or color curves. For example, some SNe show a "bump" feature near the time of maximum brightness, i.e., they show a small luminosity excess with respect to the line fit

to the linear region. Others do not have this feature, and all data and corresponding curve fits to the CMAGIC diagram appear underneath the fit line [49]. Early CMAGIC literature suggested that the bump feature, along with a possible observed bifurcation in the slope distribution, may be indicative of two progenitor channels. It had been found that the probability of a bump occurring increases as the $B-$band stretch increases, and that the difference value $B_{max} - B_{BV}$ is directly tied to the presence of a bump feature [50, 51]. For instance, SNe with $\Delta m_{15} \gtrsim 1.1$ tend to have $|B_{max} - B_{BV}| \approx 0$, and SNe with $\Delta m_{15} \lesssim 1.1$ have $|B_{max} - B_{BV}| \lesssim 0$ [51]. It has also been suggested that variations in slope may be indicative of underlying supernova physics [8].

1.3.2 Cosmological results from CMAGIC

Cosmological results from CMAGIC are consistent with the current picture of cosmology, i.e., an accelerating flat Universe with a cosmological constant [50]. The Hubble residual from CMAGIC standardization has root mean square (RMS) dispersion of approximately 0.14 mag, which is comparable to other methods that use the magnitude at maximum brightness for standardization [51]. However, it is not currently known if the bump feature affects these results. For low-redshift SNe, it is straightforward to circumvent this potential issue: a bump is easily detectable with data that are sufficiently high-quality. It would be more difficult to detect a bump for a high-z sample [50].

Previous work has used the extinction-free magnitude B_{EF} (Equation 1.33) as a quantity in the distance modulus model [9]:

$$\begin{aligned}\mu =& B_{BV} - M - \delta(\Delta m_{15} - \langle \Delta m_{15} \rangle) \\ & - (R_B - \beta_{BV})\Big(\frac{B_{max} - B_{BV}}{\beta_{BV}} + 0.6 + 1.2\Big(\frac{1}{\beta_{BV}} - \Big\langle \frac{1}{\beta_{BV}} \Big\rangle\Big)\Big)\end{aligned} \tag{1.34}$$

In this model, the free fit parameters are M, δ, and R_B. Angled brackets represent the average of the quantity inside the brackets over the entire sample. This model makes some assumptions and simplifications; the $0.6 + 1.2\Big(\frac{1}{\beta_{BV}} - \Big\langle \frac{1}{\beta_{BV}} \Big\rangle\Big)$ term represents the average of $\frac{B_{max} - B_{BV}}{\beta_{BV}}$. The factor of 1.2 comes from 2×0.6; i.e., an assumed average slope of 2

has been adopted in order to calculate *only* the average $B_{max} - B_{BV}$. In the work that fit this model, the weighted root mean square (WRMS) of the Hubble residual ranged from $0.119 < \mathrm{WRMS} < 0.137$, depending on the strictness of a color cut applied to the sample.

2. DATA

2.1 Spectrophotometry

Integral field spectrographs (IFS) combine imaging techniques with spectroscopic techniques [52, 53]. An image passes through the telescope, and is then split into many spatial samples with a microlens array. Each of these samples is fed into a spectrograph, and the result is many spectra for a single telescope pointing. The product is a "data cube" with coordinates $(\alpha, \delta, \lambda)$, representing 2D sky coordinates and wavelength, respectively. These instruments are advantageous for SN searches because they allow simultaneous observation of both the supernova (point source), its host galaxy (extended source), and the sky. This allows spectral characterization of the object, its host, and contaminants at the same time, enabling pristine background subtraction.

Spectrophotometric data are spectra such that the flux scale of the spectrum is calibrated to the flux of a standard star. Standard stars are stars that have well-characterized spectra. These "actual" flux values can be obtained from databases such as `CALSPEC` [54], or models. Spectral observations of the chosen standard stars that are taken at the same time as the data for the science object are calibrated to the "true" reference spectrum. This is necessary in order to account for effects like airmass and seeing—the reference and science object spectra should have as similar conditions as possible. Finally, the science spectrum is calibrated to the adjusted observed reference spectrum, yielding a science spectrum in physical units (e.g., ergs s^{-1} $Å^{-1}$ cm^2).

A further advantage of using an IFS is that analyses are not restricted to a particular set of photometric filters. Given a flux-calibrated (i.e., spectrophotometric) data cube, the full original image can be reconstructed by generating synthetic photometry in any chosen filters, as long as the filters are within the wavelength range of the spectra.

2.2 The Nearby Supernova Factory

The Nearby Supernova Factory (SNfactory) is a spectrophotometric dataset consisting of 275 low-z ($0.03 < z < 0.08$) SNe Ia [55]. Because each object has observations at several epochs, there are a total of 3731 flux-calibrated spectra. All SNe are in the smooth Hubble flow (i.e., their radial velocities are relatively uncontaminated by host galaxy peculiar velocities), thus, they are ideal for probing the nature of dark energy in the nearby Universe ($z \lesssim 0.1$). It is especially important to obtain precise knowledge of nearby supernovae for cosmological purposes because the rest of the cosmic distance ladder relies on the calibration of these objects. If the low-z rung of the cosmic distance ladder forms a more stable base for higher-z measurements, a more precise calculation of H_0 can be made. In addition to providing a zero-point for the Hubble diagram, they allow us to better understand SN Ia physics, including the relationship between brightness and light curve width and intrinsic color. Accurate $k-$corrections also pose a challenge for SN cosmology. At higher z, spectral features redshift out of the observer-frame photometric bandpasses. Because SNfactory SNe are spectrophotometric, and thus do not require $k-$corrections, they are an excellent source for constructing a basis for more accurate $k-$ corrections at higher z. Thus, the error contribution from systematics can be reduced with such a dataset.

These SNe were discovered using CCD images from JPL's Near Earth Asteroid Team (NEAT) and the Palomar-Quest (PQ) survey, and were followed up using the SuperNova Integral Field Spectrograph (SNIFS) [56] on the University of Hawaii 2.2-m telescope on Mauna Kea [55]. SNIFS provides wavelength coverage from $3200\text{Å} - 10,000\text{Å}$, which translates roughly to the coverage of $UBVRI$ Johnson filters [14]. The spectrograph has two "arms"—a blue arm ($3200\text{Å} - 5600\text{Å}$, $R \sim 1000$) and a red arm ($5200\text{Å} - 10000\text{Å}$, $R \sim 1300$). This split design is necessary to accommodate the wide target wavelength range. Once the spectra from the blue and red arms are merged, there are 225 spectra per pointing from SNIFS.

The SNfactory data are not flux-calibrated exactly as described in Section 2.1. The

SNIFS CALibration Apparatus (SCALA) [57] uses a Xenon lamp for the blue arm and a halogen lamp for the red arm as proxies for astronomical standards. Atmospheric conditions are monitored for SCALA with observations of `CALSPEC` [54] standard stars [58].

2.2.1 Spectral models from the Nearby Supernova Factory

Several spectral models have been developed from the SNfactory data. The SuperNova Empirical MOdels (SNEMO) is a PCA-based time series spectral energy distribution (SED) model, which aimed to improve upon the SALT2 PCA-like model by identifying additional components that describe significant SN Ia variation [59, 60]. Three models are developed: one with two free parameters for the purposes of comparing with SALT2, one with seven, and one with 15 free parameters. The SUpernova Genreator And Reconstructor (SUGAR) model is a similar time series SED model developed using SNfactory data with PCA-like methods [61, 60].

The "Twins embedding" model intends to model spectral variability at maximum light rather than over the full time series. It expands a previous method [62] to include a spectral parameterization of SNe Ia [63]. The nonlinear model includes three PCA-like components that describe $\sim 80\%$ of the variance between SNe Ia. The three components of the model, represented by ξ_i, roughly correspond to pEW of Ca II features, pEW of Si II features, and ejecta velocity [63].

There is also a probabilistic autoencoder (PAE) model [64]. This is a nonlinear method that uses the probability distribution of the data to generate simulated samples; this is advantageous because it allows construction of a realistic simulated SN Ia dataset.

2.2.2 Previous SN Ia calibration results from the Nearby Supernova Factory

An early SNfactory cosmological study found that the flux ratio of the spectral features at 6420Å and 4430Å is highly correlated with SN Ia luminosity [43]. Using a sample size of 58 SNe, and without removing highly extincted or 91T/99aa-like SNe, they fit the single-

parameter distance modulus model

$$\mu = m_B - M - \gamma\mathcal{R}, \tag{2.1}$$

where m_B is the $B-$band magnitude at the time of the observation, $\mathcal{R}$ is the flux ratio of the spectral features at 6420Å and 4430Å, and M and γ are free fit parameters. They find that the standard deviation from this fit (i.e., Hubble residual) is $\Delta\mu(\mathcal{R}) \approx 0.13$. For comparison, the result from the SALT2 model (i.e., photometry only) for the same data was $\Delta\mu(x_1, c) \approx 0.16$. These results are a compelling argument for including spectral information in SN Ia cosmological analyses, and by design, for using SNfactory to do so.

The SNfactory data also yielded the "twin" method for standardizing SNe Ia. In this method, SNe with matching spectra in their full time series are assumed to originate from the same progenitor and explosion mechanism [62]. Because spectroscopic twins' intrinsic brightness and colors are the same, any difference in these values can be attributed to dust effects. "Twinness" is quantified by minimizing a χ^2-like quantity, represented by ξ. This method resulted in a dispersion of $\sim$ 0.08 [62]. Twinness was revisited later with the nonlinear "Twins embedding" model [63]. Because its components are nonlinear, the usual linear methods of standardization cannot be used with these parameters. However, standardizing using this model as well as twins yields residuals down to ~ 0.07 [65].

In addition to SN Ia calibration, SNfactory data have been used to examine SN physics for individual SNe Ia. This is necessary in order to better understand standardization. SN 2011fe has been the subject of several publications; it has become the archetypical "normal" SN Ia due to the fact that it is extremely nearby and minimally affected by dust [66, 67, 68]. Unusual SNe have received the same treatment, providing a necessary window into the possible variations of SN Ia physics [69, 70, 71].

3. METHODS

All analysis in this work is carried out using the Nearby Supernova Factory (SNfactory) spectrophotometric dataset, described in Section 2.1.

3.1 Synthetic Photometry

Because spectra from SNIFS are spectrophotometric, synthetic photometry can be generated without concern for color calibration or $k-$corrections. First, all spectra are corrected for the effects of Milky Way dust [29]. Then, all spectra are converted to the observer frame at redshift $z = 0.05$. Correcting the observed wavelength for the relativistic Doppler effect is done by:

$$\lambda_{rest\ frame} = \frac{\lambda_{observed}}{1 + z_{helio}}. \tag{3.1}$$

The full spectrum wavelength correction is

$$\lambda_{z=0.05} = \frac{\lambda_{observed}}{1 + z_{helio}}(1 + 0.05). \tag{3.2}$$

Bessell filters [14], which are given in the rest frame, were also set to $z = 0.05$ using $\lambda_{observed} = \lambda_{rest\ frame}(1+z)$. The transmission curves do not need to be adjusted because they are given in fractional quantities (Appendix A).

Fluxes were normalized to $z = 0.05$ using

$$F_{ref} = F_{actual}\Big(\frac{1 + z_{helio}}{1 + z_{ref}}\Big)\Big(\frac{D_{L,actual}}{D_{L,ref}}\Big)^2 = F_{actual}\Big(\frac{a(t_{ref})}{a(t_{actual})}\Big), \tag{3.3}$$

where F_{actual} is the original spectrum flux, z_{helio} is heliocentric redshift, z_{ref} is the new redshift (i.e., $z = 0.05$), $D_{L,actual}$ and $D_{L,ref}$ are luminosity distances for the object's original z and at $z = 0.05$ assuming a flat ΛCDM cosmology with $H_0 = 70$ km s^{-1} Mpc^{-1} and $\Omega_{m,0} = 0.3$, and both $a(t)$ are the cosmological scale factors associated with the original z

and $z = 0.05$ for the assumed cosmology. Then, the error of the normalized flux is

$$\sigma_{F_{ref}} = \sigma_{F_{actual}} \frac{\partial F_{ref}}{\partial F_{actual}} = \sigma_{F_{actual}} \Big(\frac{1 + z_{helio}}{1 + z_{ref}} \Big) \Big(\frac{D_{L,actual}}{D_{L,ref}} \Big)^2. \tag{3.4}$$

See Appendix B.1 for a summary of error propagation procedures. After these corrections are made, synthetic photometry can be generated. The area under the spectrum, F, in a given filter X for a photon-counting detector, is calculated by

$$F_X = \int_{\lambda_1}^{\lambda_2} \lambda f(\lambda) R_X(\lambda) d\lambda, \tag{3.5}$$

where $f(\lambda)$ is the rest-frame spectrum, and $R_X(\lambda)$ is the photometric filter. The standard $BVRI$ filters used in this analysis are summarized in Appendix A [14].

However, the continuous version of this function cannot be directly applied to an analysis carried out via Python. The discrete version is:

$$F_X = \sum_{i=\lambda_1}^{\lambda_2} \lambda_i f(\lambda_i) R_X(\lambda_i) (\lambda_i - \lambda_{i-1}), \tag{3.6}$$

where $f(\lambda_i)$ is the energy flux at a particular wavelength λ_i, and $R_X(\lambda_i)$ is the response function for the filter at wavelength λ_i. $(\lambda_i - \lambda_{i-1})$ corresponds to $d\lambda$.

Then, using Equation B.1, the variance of F is:

$$\sigma_F^2 = \Big(\sum_{i=\lambda_1}^{\lambda_2} \sigma_{f(\lambda_i)} R_X(\lambda_i) (\lambda_i - \lambda_{i-1}) \Big)^2 \tag{3.7}$$

Individual magnitudes are calculated by

$$m = -2.5 \log_{10} \Big(\frac{F}{F_{ref}} \Big) = -2.5 \log_{10}(F) + 2.5 \log_{10}(F_{ref}) = -2.5 \log_{10}(F) - m_{ref}, \tag{3.8}$$

where F_{ref} and m_{ref} are flux and magnitude, respectively, from a reference object. For this work, we use the Vega magnitude system, and the reference object is a spectrum from the

reference star Vega (Alpha Lyrae). Specifically, we use `alpha_lyr_stis_010.fits` from the CALSPEC database [54].

Equation 3.6 is also used on the Vega spectrum to calculate F_{ref}, with the same response function as is used on the supernova spectrum. For the Vega magnitude system, $m_{ref} = 0$.

For arbitrary photometric color $X - Y$,

$$m_X - m_Y = -2.5 \log\left(\frac{F_X}{F_{ref,X}}\right) + 2.5 \log\left(\frac{F_Y}{F_{ref,Y}}\right) \tag{3.9}$$

.

To propagate error for color $X - Y$, we will treat m_{X-Y} as a function of $f(\lambda_i)$. Then, for arbitrary color $X - Y$, the Jacobian is:

$$\mathbf{J}_{X-Y} = \begin{bmatrix} \frac{\partial m_{X-Y}}{\partial f(\lambda_0)} & \frac{\partial m_{X-Y}}{\partial f(\lambda_1)} & \cdots & \frac{\partial m_{X-Y}}{\partial f(\lambda_N)} \end{bmatrix} \tag{3.10}$$

where N is the last measured wavelength in the spectrum. The ith entry is:

$$\frac{\partial m_{X-Y}}{\partial f(\lambda_i)} = -\frac{1.09}{F_X} R_X(\lambda_i)(\lambda_i - \lambda_{i-1}) + \frac{1.09}{F_Y} R_Y(\lambda_i)(\lambda_i - \lambda_{i-1}) \tag{3.11}$$

The covariance matrix is diagonal, and each entry is the spectrum error provided in the data:

$$\mathbf{C_{X-Y}} = \begin{bmatrix} \sigma^2_{f(\lambda_0)} & & & \\ & \sigma^2_{f(\lambda_1)} & & \\ & & \ddots & \\ & & & \sigma^2_{f(\lambda_N)} \end{bmatrix}. \tag{3.12}$$

Finally, we use $\sigma^2_{m_{X-Y}} = \mathbf{J_{X-Y}} \mathbf{C_{X-Y}} \mathbf{J^T_{X-Y}}$ to calculate the variance of m_{X-Y}.

3.2 Light curve fitting

3.2.1 fPCA

The synthetic light curves (Section 3.1) are fit using functional principal component analysis (fPCA) [72, 73] templates [9]. These templates, which are functional paramaterizations of light curves, are statistically generated from data. Although they are functions, they are analogous to vectors, where all principal components (PCs) are orthogonal. Each template represents a different aspect of SN Ia light curve shape, for example, there is one that represents the mean SN Ia light curve, and another that is closely related to the width of the light curve. The data are fit to a model that is a linear combination of the PCs. The model is described by

$$g_{s\lambda}(q) = m_{s\lambda} + \phi_{0\lambda}(q) + \sum_{k=1}^{K} \beta_{s\lambda}^{(k)} \phi_{k\lambda}(q), \tag{3.13}$$

where q is phase, $m_{s\lambda}$ is peak magnitude, s is the corresponding supernova, λ is the corresponding filter, $\phi_{k\lambda}$ are the fPCA vectors, and $\beta_{s\lambda}^{(k)}$ are the outputs of the fPCA analysis code [9]. Although four PCs are available, only two are used in this analysis. Including the third and fourth vectors resulted in unphysical fits for some SNe because the data were insufficient to realistically constrain the fit using this method.

The error for the entire light curve can be calculated with $\sigma^2 = \mathbf{JCJ^T}$. The covariance matrix is output from the fPCA analysis code.

The Jacobian is

$$\mathbf{J}_{g_{s\lambda}} = \left[\frac{\partial g_{s\lambda}}{\partial q_0} \quad \frac{\partial g_{s\lambda}}{\partial m_{s\lambda}} \quad \frac{\partial g_{s\lambda}}{\partial \beta_{s\lambda}^{(1)}} \quad \frac{\partial g_{s\lambda}}{\partial \beta_{s\lambda}^{(2)}} \quad \frac{\partial g_{s\lambda}}{\partial \beta_{s\lambda}^{(3)}} \quad \frac{\partial g_{s\lambda}}{\partial \beta_{s\lambda}^{(4)}} \right], \tag{3.14}$$

or, equivalently,

$$\mathbf{J}_{g_{s\lambda}} = \left[0 \quad 1 \quad \phi_{1\lambda}(q) \quad \phi_{2\lambda}(q) \quad \phi_{3\lambda}(q) \quad \phi_{4\lambda}(q) \right]. \tag{3.15}$$

The error in Δm_{15} is calculated similarly. If

$$\Delta m_{15} = g_{s\lambda}(q_0 + 15) - g_{s\lambda}(q_0) = \phi_{0\lambda}(q_0 + 15) - \phi_{0\lambda}(q_0) + \sum_{k=1}^{K} \beta_{s\lambda}^{(k)} \Big(\phi_{k\lambda}(q_0 + 15) - \phi_{k\lambda}(q_0) \Big), \tag{3.16}$$

then $\mathbf{J}_{\Delta m_{15}}$ is given by

$$\mathbf{J}_{\Delta m_{15}} = \left[\frac{\partial \Delta m_{15}}{\partial q_0} \quad \frac{\partial \Delta m_{15}}{\partial m_{s\lambda}} \quad \frac{\partial \Delta m_{15}}{\partial \beta_{s\lambda}^{(1)}} \quad \frac{\partial \Delta m_{15}}{\partial \beta_{s\lambda}^{(2)}} \quad \frac{\partial \Delta m_{15}}{\partial \beta_{s\lambda}^{(3)}} \quad \frac{\partial \Delta m_{15}}{\partial \beta_{s\lambda}^{(4)}} \right], \tag{3.17}$$

The first entry is

$$\frac{\partial \Delta m_{15}}{\partial q_0} = \frac{\partial \phi_0(q_0 + 15)}{\partial q_0} - \frac{\partial \phi_0(q_0)}{\partial q_0} + \sum_{k=1}^{K} \beta_{s\lambda}^{(k)} \Big(\frac{\partial \phi_{k\lambda}(q_0 + 15)}{\partial q_0} - \frac{\partial \phi_{k\lambda}(q_0)}{\partial q_0} \Big) \tag{3.18}$$

These values can be calculated directly when this formula is discretized because each vector exists in the form of a discrete grid. The second entry is always 0. The derivatives with respect to $\beta_{s\lambda}^{(k)}$ are:

$$\frac{\partial \Delta m_{15}}{\partial \beta_{s\lambda}^{(k)}} = \Big(\phi_{k\lambda}(q_0 + 15) - \phi_{k\lambda}(q_0) \Big) \tag{3.19}$$

The covariance matrix used is the same one that is output from the fPCA analysis code. The fPCA templates and a fitting routine can be used by installing `snlcpy`, a Python package located at https://github.com/laldoroty/snlcpy [74].

3.2.2 SALT3

The Spectral Adaptive Light-curve Template (SALT) models [27, 28, 3] have been key to many SN Ia studies, ranging from analyses that focus on SN Ia physics to those that are cosmological [32, 33, 75, 41, 63, 65]. Following suit, the synthetic light curves in this analysis are also fit using the SALT3 templates [3], implemented in `sncosmo` [76]. These models are spectral energy distribution (SED) templates, which have both wavelength and time axes. Thus, photometric time series data (light curves) can be fit with any arbitrary photometric

filter, as long as those filters fall within the wavelength range of the templates. The template is represented as a linear combination of flux surfaces, multiplied by a color law:

$$F(p,\lambda) = x_0[M_0(p,\lambda;\mathbf{m_0}) + x_1 M_1(p,\lambda;\mathbf{m_1})] \cdot \exp(-0.4c \cdot CL(\lambda;\mathbf{cl})), \tag{3.20}$$

where M_i are components of the flux templates, CL is a polynomial color law, and (x_0, x_1, c) are free fit parameters [27, 28, 3].

3.3 CMAGIC analysis

Data and fit light curves were used to construct color-magnitude diagrams (CMAGIC diagrams) for all SNe in the sample. The linear regions of each SN were determined by eye in the $B-V$, $B-R$, and $B-I$ CMAGIC diagram color combinations. All linear regions were fit using Levenberg-Marquardt least squares minimization (Appendix B.2) via `mpfit` in Python [77, 78, 79]. Errors were scaled such that χ^2 was fixed equal to the number of degrees of freedom for each fit in order to account for unknown sources of error.

3.3.1 Bump feature

The size of the bump feature is defined as

$$\omega_{XY} = (\beta_{XY}(X-Y)_{max} + X_{XY0}) - m_{Xmax} \tag{3.21}$$

where m_{Xmax} is the magnitude at maximum brightness in the arbitrary $X-$band, β_{XY} is the slope of the linear region from the fit (purple line in Figure 3.1), $(X-Y)_{max}$ is the color at the time of $X-$band maximum, and X_{XY0} is the value of the fit line when $(X-Y)=0$. If there is a bump, ω_{XY} will be positive; if there is no bump, the value will be negative.

We use $\sigma^2 = \mathbf{JCJ^T}$ to calculate the error in bump size. We construct a covariance matrix

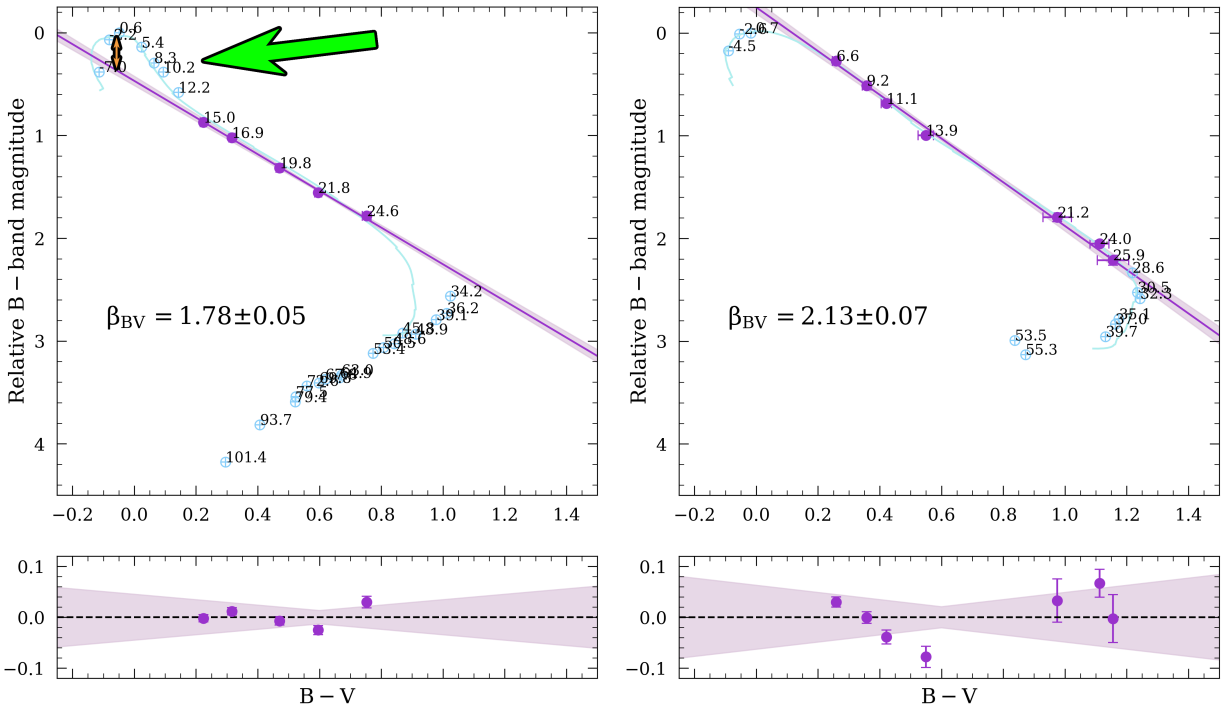

Figure 3.1: *Left*: A sample CMAGIC diagram that shows a bump feature, indicated by the green arrow. The vertical orange arrow shows where the bump size ω_{BV} is measured. *Right*: A sample CMAGIC diagram that does not show a bump. In both panels, the filled purple points are included in the linear fit (purple line), and the empty blue points are excluded. The light purple filled region is fit error. The lower panels are the residuals between the linear fits and the data. Figure from [2]. © AAS. Reproduced with permission.

with rows and columns for m_X, $X-Y$, β_{XY}, and X_{XY0}:

$$\mathbf{C_{bump}} = \begin{bmatrix} \sigma^2_{m_{X,max}} & \sigma^2_{m_{X,max}(X-Y)_{max}} & 0 & 0 \\ \sigma^2_{m_{X,max}(X-Y)_{max}} & \sigma^2_{(X-Y)_{max}} & 0 & 0 \\ 0 & 0 & \sigma^2_{\beta_{XY}} & \sigma^2_{\beta_{XY}X_{XY0}} \\ 0 & 0 & \sigma^2_{\beta_{XY}X_{XY0}} & \sigma^2_{X_{XY0}} \end{bmatrix}. \tag{3.22}$$

If it is assumed that the X and Y bands are independent, then $\sigma^2_{m_{X,max}(X-Y)_{max}} = 0$. Although the bandpasses are *not* independent in reality, we assume independence in this work for ease of calculation, as the final results would not be significantly affected by this complication. The Jacobian is:

$$\mathbf{J}_\omega = \begin{bmatrix} \frac{\partial\omega}{\partial m_{X,max}} & \frac{\partial\omega}{\partial(X-Y)_{max}} & \frac{\partial\omega}{\partial\beta_{XY}} & \frac{\partial\omega}{\partial X_{XY0}} \end{bmatrix} \tag{3.23}$$

$$= \begin{bmatrix} -1 & \beta_{XY} & (X-Y)_{max} & 1 \end{bmatrix} \tag{3.24}$$

3.3.2 Color-width

We also define a new color-width parameter, Δ_{X-Y}, such that

$$\Delta_{X-Y} = (X-Y)_{intersection} - (X-Y)_{Xmax}, \tag{3.25}$$

where X and Y are arbitrary photometric bands, $(X-Y)_{intersection}$ is the color at the intersection of the lines fit to the two linear regions, and $(X-Y)_{Xmax}$ is the color at the time of maximum brightness in the X-band. Because color is an axis on the CMAGIC diagram, any reddening will not change the shape of the curve; it will shift it along the x-axis. Therefore, it is unlikely that Δ_{X-Y} is affected by dust.

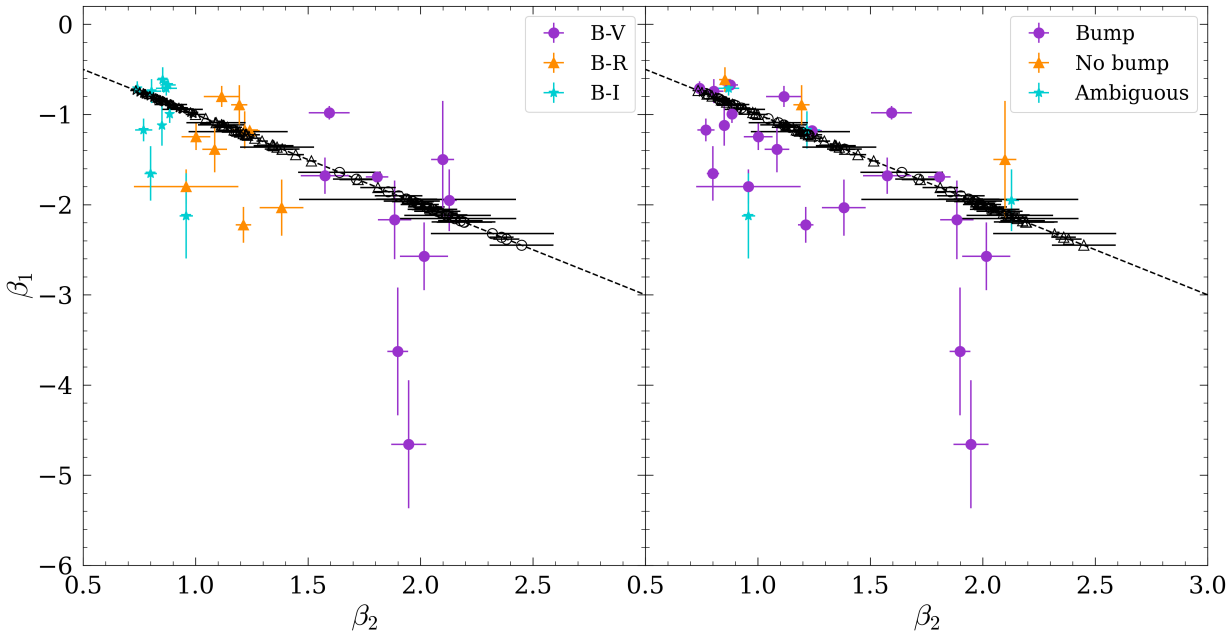

Figure 3.2: *Left*: The slope of the first linear region, β_1, compared to the slope of the second linear region, β_2, color-coded by which CMAGIC diagram the measurement belongs to. Purple, orange, and blue points indicate SNe where the slope of the second linear region could be measured without fixing $\beta_1 = \beta_2$. Empty black outlined points indicate SNe fit with a fixed slope for the second linear region such that $\beta_1 = \beta_2$. For all points, circles belong to $B-V$, triangles belong to $B-R$, and stars belong to $B-I$. *Right*: The same as *left* except color-coded by bump or no bump. Circles belong to the bump sample, triangles belong to the no bump sample, and stars belong to the ambiguous group.

3.3.3 Data cuts

Data cuts were applied to the SNFactory sample for this analysis. First, only SNe in the "training" and "validation" samples were considered, reducing the total number of objects from 275 to 223. All SNe in these samples that did not have observations prior to maximum brightness in the $B-$ band were excluded. Additionally, SNe with less than three observations in the first linear region of any of the three CMAGIC diagrams ($B-V$, $B-R$, or $B-I$) were excluded from this analysis.

In many cases, there were not enough data after 30 days, and it was not possible to fit the second linear region. In order to proceed, it was necessary to find an appropriate approximation for β_2. In many cases, β_1 and β_2 approximately mirror each other (Figure 3.2). Thus, if a supernova had insufficient data in the second linear region to fit the line with β_2 as a free parameter, a fixed slope was used such that the magnitude of the fixed slope "mirrored" the magnitude of the first slope. Because spectra were not available for all SNe 30 days after maximum brightness, Δ_{X-Y} could not be calculated for the entire sample because β_2 could not be measured. β_2 could be measured for 42 SNe, with the slope allowed to vary as a free parameter for 9, 9, and 10 SNe in the $B-V$, $B-R$, and $B-I$ CMAGIC diagrams, respectively. Therefore, Δ_{X-Y} was calculated for the SNe where β_2 could be measured. These quantities include SNe where a fixed β_2 was used, which may affect results.

Peculiar SNe are only removed for the cosmological portion of this analysis. These include PTF11mkx, which is 91T-like [**?**]; LSQ12fhe, which is also 91T-like [**?**]; SNF20070606-006, a known 99aa-like SN [80]; SNF20070803-005, a super-Chandrasekhar mass SN [81]; and LSQ12gxj, which is subluminous, may show evidence for absorption along the line-of-sight, and has previously been excluded from distance modulus parameter calculations [82].

3.4 Spectral analysis

3.4.1 Pseudo-equivalent widths

Pseudo-equivalent widths (pEW) were calculated by first smoothing the spectrum nearest to maximum brightness using a moving average filter. This ensures that the pseudo-continuum is less likely to be affected by anomalous spikes or dips due to noise. Next, Gaussian profiles were fit to the smoothed λ6355 and λ5972 Si II features using a bootstrapping method. 20Å regions were specified on either side of each absorption feature, and endpoints were drawn from this region a total of 225 times [35]. For each draw, the area under the Gaussian curve was recorded. The final pEW is the mean of all 225 area measurements, and its error is their standard deviation.

3.4.2 Line velocity

Line velocities were calculated by using a single set of endpoints for each absorption line used in the pseudo-equivalent width calculations. A Gaussian profile was fit, and the "center" parameter of the fit was taken to be the center wavelength of the line. Then, the velocity was calculated using the relativistic Doppler formula,

$$v_{\text{Si II}} = c\frac{\left(\frac{\Delta\lambda}{\lambda_0}+1\right)^2 - 1}{\left(\frac{\Delta\lambda}{\lambda_0}+1\right)^2 + 1}, \tag{3.26}$$

where λ_0 is the rest frame wavelength of the absorption line, $\Delta\lambda$ is the difference between λ_0 and the measured center wavelength, and c is the speed of light [35].

3.4.3 F R(Ni II)

F R(Ni II) is defined as the ratio of the flux of the maximum near 3950Å to the flux at the minimum near 4000Å, and has previously been found to be a good indicator of ^{56}Ni mass [36].

We used a previously-developed Long Short-Term Memory (LSTM) neural network called `SNAIL` [83] to predict spectra for each SN at maximum brightness. Then, the relevant local

minima and maxima were measured from these predicted spectra, which are all normalized to their mean flux, and the flux ratio F R(Ni II) is recorded.

3.5 Cosmological fitting

Before any cosmological analysis could begin, all SNe had to be "moved back" to their original redshift because they were normalized to $z = 0.05$ to ensure appropriate treatment of flux (Section 3.1). Given the definition of the distance modulus, $\mu = m - M$, and an assumed flat ΛCDM cosmology with $H_0 = 70$ km s^{-1} Mpc^{-1} and $\Omega_{m,0} = 0.3$, this can be done using the equation

$$m_{original} = \mu_{original} - M = \mu_{original} - (m_{z=0.05} - \mu_{z=0.05}). \tag{3.27}$$

Additionally, to take advantage of the information that spectra provide, an absorption line velocity cut was applied so all SNe have $v_{\text{Si II } \lambda 6355} < 12000$ km s^{-1} [7, 84]. It has been shown that SNe Ia with high velocity Si II features tend to be redder [37, 85] and have more negative Hubble residuals than normal SNe Ia [86]. Thus, it may result in a more "standard" sample if these SNe are excluded [84].

We fit four distance modulus models to an assumed ΛCDM cosmology with $H_0 = 70$ km s^{-1} Mpc^{-1} and $\Omega_{m,0} = 0.3$ using maximum likelihood estimation (Appendix B.3) and Markov chain Monte Carlo methods (Appendix B.4, [87]). Fits are applied to two groups of SNe: one without a color cut, and one such that $(B - V)_{max} < 0.05$, as it is assumed that these SNe are minimally affected by dust.

These models include the standard "Tripp model" [12],

$$\mu_{Tripp} = m_{Bmax} - M - \alpha(C - \langle C \rangle) - \delta(\Delta m_{15} - \langle \Delta m_{15} \rangle), \tag{3.28}$$

where m_{Bmax} is the apparent B-band maximum brightness, M is the absolute magnitude, α is a fitting parameter describing the color correction, C is the $B - V$ color at maximum

brightness, Δm_{15} is the change in magnitude between B-band maximum brightness and 15 days later, and angle brackets indicate the average of our sample. Additionally, $\sigma^2 = \sigma^2_{vpec,i} + \sigma^2_{Bmax,i} + (\alpha\sigma_{C,i})^2 + (\delta\sigma_{\Delta m_{15},i})^2$. σ_{vpec} is error in peculiar velocity [46]. For SALT3 [3], we use the standard SALT distance modulus model,

$$\mu_{SALT} = m_{Bmax} - M + \alpha x_1 - \beta c. \tag{3.29}$$

where M, α, and β are parameters to be fit. Here, $\sigma^2 = \sigma^2_{vpec,i} + \sigma^2_{m_{Bmax,i}} + (\alpha\sigma_{x_{1,i}})^2 + (\beta\sigma_{c_i})^2$.

Finally, we introduce a new spectrum-based distance modulus model:

$$\mu_{F\ R(Ni\ II)} = m_{Bmax} - M + \alpha[\text{F R(Ni II)}] - \beta c, \tag{3.30}$$

where F R(Ni II) is the ratio of the fluxes described in Section 3.4.3, and c is the SALT color term. This model is identical to the standard SALT model, except with stretch x_1 replaced with the flux ratio of the Si II/Ni II blended absorption feature [36].

We also fit a previously-introduced CMAGIC model [9]:

$$\mu_{H18} = B_{BV} - M - \delta(\Delta m_{15} - \langle\Delta m_{15}\rangle) - (b_2 - \beta_{BV})\Big(\frac{m_{Bmax} - B_{BV}}{\beta_{BV}} + 1.2\Big(\frac{1}{\beta_{BV}} - \Big\langle\frac{1}{\beta_{BV}}\Big\rangle\Big)\Big) \tag{3.31}$$

We introduce a new distance modulus model based on CMAGIC,

$$\mu = B_{BV} - M - \delta(\Delta m_{15} - \langle\Delta m_{15}\rangle) - (b - \beta_{BV})\Big(\frac{m_{Bmax} - B_{BV}}{\beta_{BV}} - \Big\langle\frac{m_{Bmax} - B_{BV}}{\beta_{BV}}\Big\rangle\Big). \tag{3.32}$$

where M, δ, and b are parameters to be fit. The CMAGIC models are based on the extinction-free parameter B_{EF} (Equation 1.33). The difference between the two CMAGIC models is that Equation 3.31 assumes an average slope of 2 in order to calculate *only* the average $B_{max} - B_{BV}$, i.e., $\langle m_{Bmax} - B_{BV}\rangle = 1.2$. The model introduced in this thesis (Equation 3.32)

does not make this assumption.

Finally, we examine a CMAGIC-based model where SNe are not corrected for decline rate. We do this because the CMAGIC magnitude B_{BV} is less correlated with light curve width than m_{Bmax} (Figure 4.18, [49]). If this model performs as well as the other CMAGIC models that include decline rate, then SNe without pre-maximum observations would be able to be included in cosmological analyses, vastly increasing the amount of available data. This model is identical to Equation 3.32, but with the decline rate correction term left out:

$$\mu = B_{BV} - M - (b - \beta_{BV})\Big(\frac{m_{Bmax} - B_{BV}}{\beta_{BV}} - \Big\langle \frac{m_{Bmax} - B_{BV}}{\beta_{BV}} \Big\rangle\Big). \tag{3.33}$$

4.1 Bump morphology

The most striking result of this analysis is the correlation between the slope of the first linear region, β_{XY}, and the bump size, ω_{XY} (Figure 4.1, Table 4.1). Two-sample Kolmogorov-Smirnov (KS) tests and $t-$tests strongly suggest that the "bump" and "no bump" samples are likely to be drawn from different parent populations (Table 4.1). Further, the fact that the "ambiguous" category tends to sit in the center of these two groups indicates that the bump feature exists on a continuous basis, rather than being discrete. There are some outliers; the isolated "no bump" point in the top panel of Figure 4.1 is PTF10ygu (SN 2010jn), a known bright SN Ia with a slow decline rate [88]. Although it has more extreme values for β_{BV} and ω_{BV} than the rest of the sample, it is still consistent with the trend that SNe with larger ω_{BV} have smaller β_{BV}. PTF10ops and SNF20070714-007 are the two "no bump" outliers in the second and third panels. PTF10ops has been shown to be subluminous and does not match expected explosion models [89]. The "ambiguous" outlier in the second and third panels is SN 2004ef.

Further bolstering the conclusion that these observational features exist on a continuous basis is that there is a separation between the "bump" and "no bump" categories, with "ambiguous" in the middle, when comparing them within other parameters (Figure 4.3, Table 4.1). These comparisons show that a bump feature is associated with a slower decline rate, reflecting behavior noted previously [51]. SNe with a bump tend to have a smaller Δm_{15}, as well as weaker Si II λ6355 and λ5972 absorption features. It has also been noted that there is a piecewise relation between $B_{max} - B_{BV}$ and $\Delta m_{15,B}$ where $|B_{max} - B_{BV}|$ decreases until it hits 0 when $\Delta m_{15,B} \approx 1.1$, where it then stays consistent with 0 [51]. In the right column and third row of Figure 4.3, there is a steep decrease in the number of SNe with a bump where $\Delta m_{15} \approx 1.1$, reflecting this relationship.

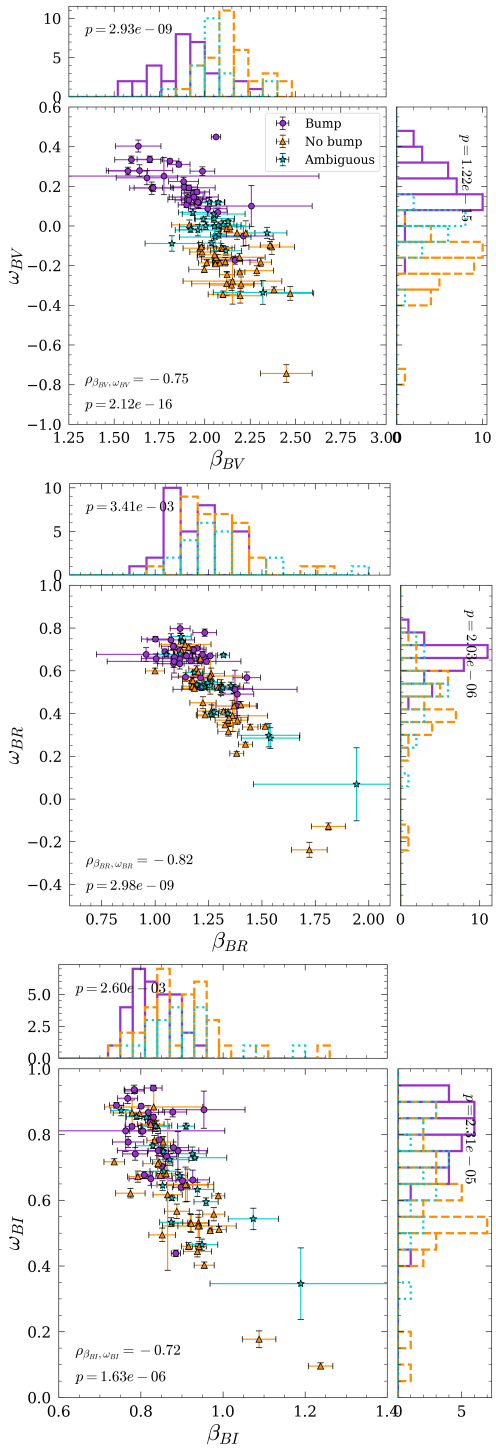

Figure 4.1: Correlations between the bump size, ω_{XY}, and slope, β_{XY}. Histograms to the top and right of the scatter plots correspond to distributions of slope and bump size, respectively. $p-$values in histogram panels are the result of two-sample Kolmogorov-Smirnov (KS) tests on the "bump" and "no bump" groups. ρ in the scatter plot panel is the Pearson correlation coefficient, with its corresponding $p-$value found below it. See Table 4.1 for a full summary of statistical test results. Figure from [2]. © AAS. Reproduced with permission.

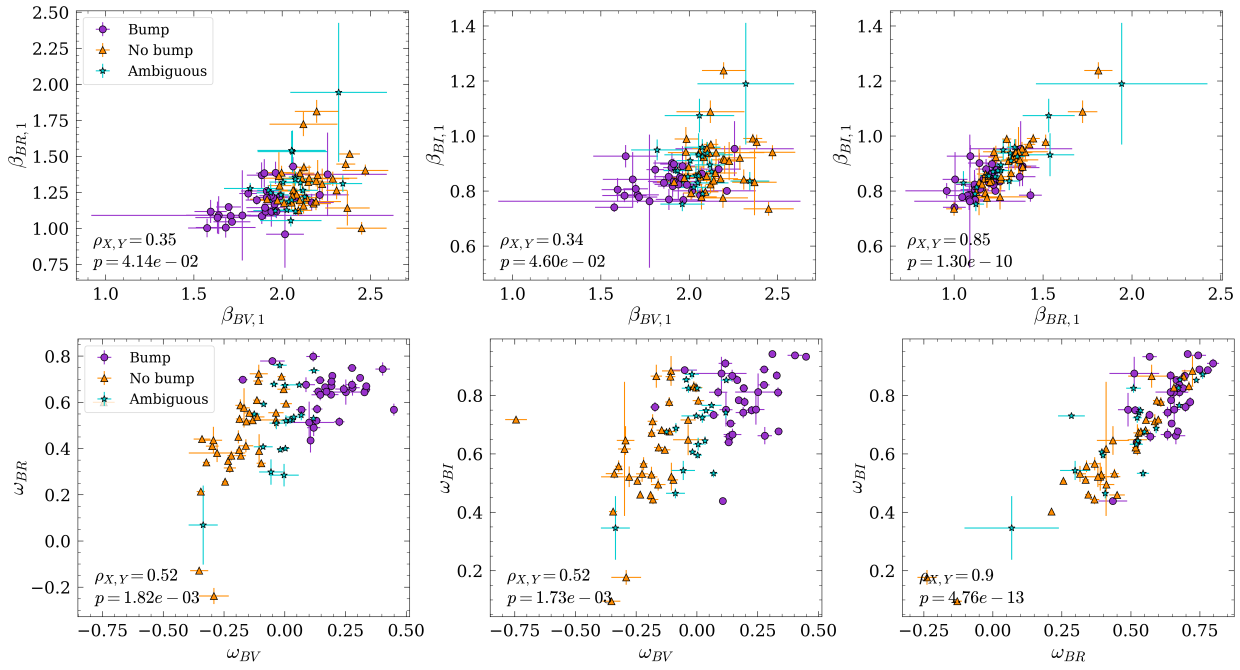

Figure 4.2: *Top row*: Correlations between $\beta_{XY,1}$ and $\beta_{XZ,1}$ for all possible combinations. *Bottom row*: Correlations between ω_{XY} and ω_{XZ} for all possible combinations. For all figures, $\rho_{X,Y}$ is the Pearson correlation coefficient, and p is the corresponding p-value.

Figure 4.3 also shows a strong sepration between the bump and no bump categories in the ratio of $\Delta m_{15,V}/\Delta m_{15,B}$. Like the slope, a KS test indicates these are likely to be drawn from different samples (Figure 4.3). Once again, the fact that the "ambiguous" category lies in the center of these indicates a continuum of bump size rather than discrete types.

For a given SN, the slopes and bump sizes in different color-magnitude combinations tend to be correlated with each other (Figure 4.2). The strongest correlations are between the $B-R$ and $B-I$ CMAGIC diagrams (Figure 4.2, *right*). The correlation between the $B-R$ and $B-I$ features being tighter than the comparison plots with $B-V$ may be interpreted as either effects due to dust, or more variation in spectral features that lie in the V band than in the R or I bands. Although the Si IIλ5972 and λ6355 lines are the focus of the spectral analysis portion of this work, they cannot be the origin of this scatter because they fall in the V and R bands only. If they were the cause of the scatter, we would expect the $B-V$ and $B-R$ features to be more tightly correlated with a larger scatter for comparisons involving

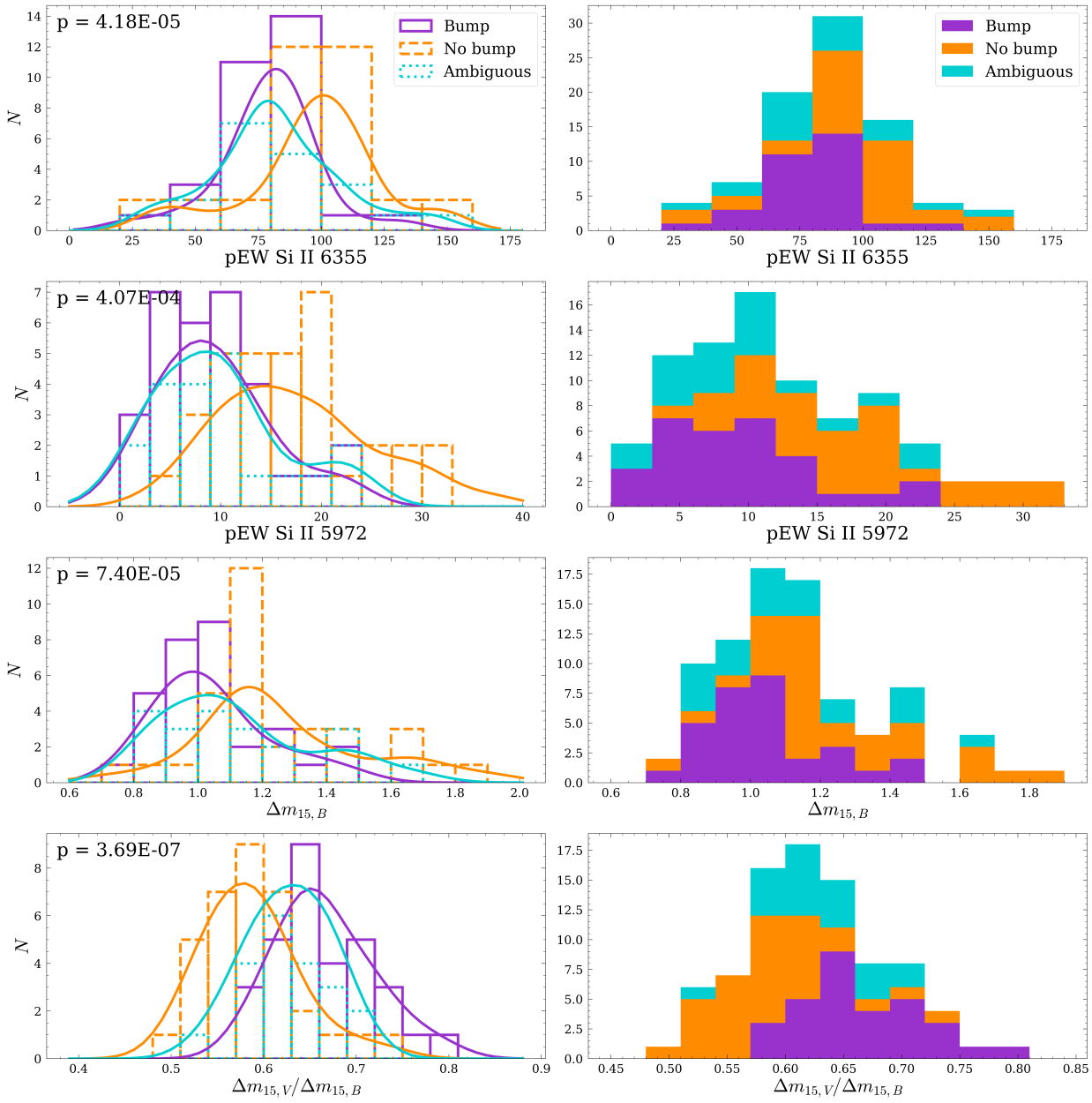

Figure 4.3: Histograms showing the distinction between measurements on "bump" and "no bump" samples. The *left* column shows overlaid histograms, and the *right* column shows stacked histograms. $p-$values are the result of two-sample Kolmogorov-Smirnov (KS) tests on the "bump" and "no bump" groups for the histogram it overlays. A smaller p-value means it is more likely that the samples are drawn from different distributions. Figure from [2]. © AAS. Reproduced with permission.

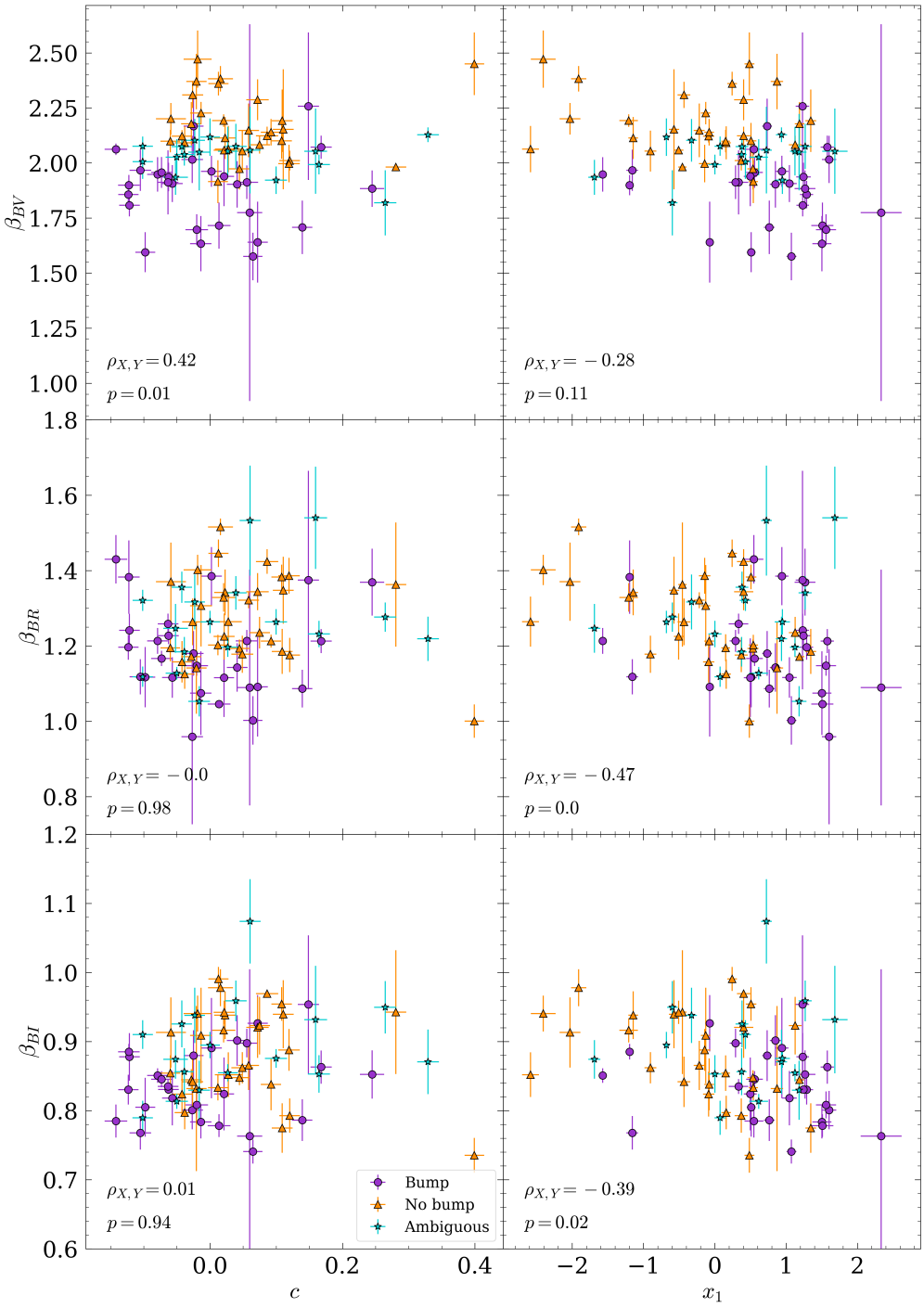

Figure 4.4: Correlations between SALT3 parameters [3] and β_{XY}. $\rho_{X,Y}$ is the Pearson correlation coefficient for all data in each panel, and p is the corresponding p-value. Figure from [2]. © AAS. Reproduced with permission.

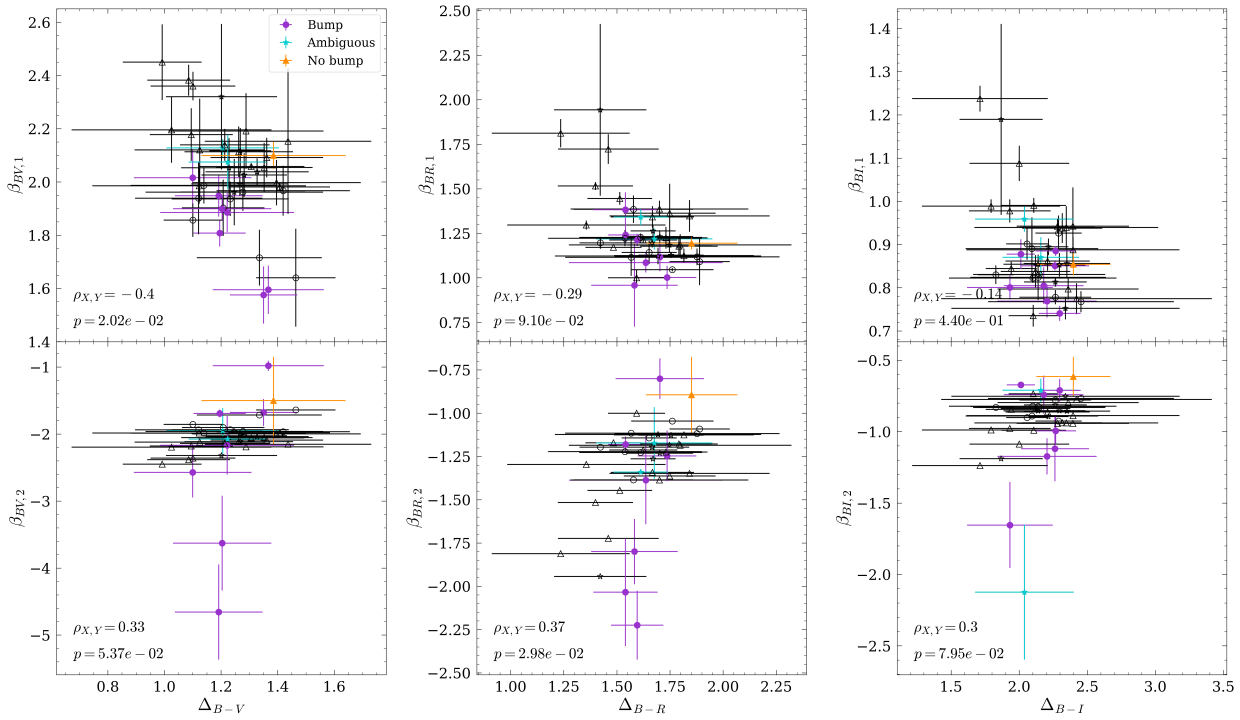

Figure 4.5: Comparison between the slopes of the first and second linear regions ($\beta_{XY,1}$ and $\beta_{XY,2}$, respectively) to the color-width parameter Δ_{X-Y}. $\rho_{X,Y}$ is the Pearson correlation coefficient for all data in each panel, and p is the corresponding p-value.

$B - I$. Because dust affects scattering in longer wavelengths less than shorter wavelengths, i.e., the V-band extinguished by dust more than the R- and I-bands, it is possible that the observed scatter in the left and center columns of Figure 4.2 is due to different amounts of host galaxy extinction.

The slopes of the first linear regions derived in this work are also compared to the SALT3 x_1 and c parameters (Figure 4.4). Although there appears to be a weak negative correlation between β_{XY} and x_1, which is reflective of the relationships previously discussed, these correlations are not conclusive and will require further verification.

Parameter	$D_{n,m}$	$p_{D_{n,m}}$	t	p_t
x_1	0.47	2.53×10^{-3}	2.93	4.84×10^{-3}
$\Delta m_{15,B}$	0.54	7.40×10^{-5}	-3.74	3.89×10^{-4}
$\Delta m_{15,V}/\Delta m_{15,B}$	0.64	9.56×10^{-7}	6.30	3.25×10^{-8}
pEW Si II λ6355	0.55	4.18×10^{-5}	-3.01	3.70×10^{-3}
pEW Si II λ5972	0.49	4.07×10^{-4}	-4.77	1.12×10^{-5}
F R(Ni II)	0.46	1.13×10^{-3}	-3.00	3.72×10^{-3}
β_{BV}	0.75	2.40×10^{-9}	-6.63	8.94×10^{-9}
β_{BR}	0.43	2.96×10^{-3}	-3.62	5.89×10^{-4}
β_{BI}	0.44	2.60×10^{-3}	-3.45	2.60×10^{-3}
ω_{BV}	0.94	1.22×10^{-15}	11.61	2.69×10^{-17}
ω_{BR}	0.62	2.03×10^{-6}	5.13	3.01×10^{-6}
ω_{BI}	0.57	2.31×10^{-5}	4.98	5.20×10^{-5}

Table 4.1: Results for a two-sample Kolmogorov-Smirnov (KS) test ($D_{n,m}$) and independent two-sample t-test for the parameters presented in this work, based on the "bump" vs. "no bump" samples. We correct for the "look-elsewhere effect" by dividing our significance level $\alpha = 0.05$ by the number of parameters in this table. Thus, our significance level is $\alpha_C = 0.004$. The first section shows results for parameters independent of the bump. The second section shows results for slope β_{XY} of the linear region of the CMAGIC diagram, which we have shown to be strongly correlated with bump size (Figure 4.1). The third section shows results for bump size ω_{XY}. The functions `ks_2samp()` and `ttest_ind()` from `scipy.stats` were used. The first column lists the tested parameter; the second and fourth columns show the test statistics; the third and fifth columns show the p-values for the test statistics in the columns to their left. For the KS test, the null hypothesis is that the "bump" and "no bump" samples are drawn from the same distribution. No assumption is made about the distributions of the data. The two-sample t-test checks the null hypothesis that the mean value of the two groups is identical. This test assumes the data are normally distributed. We do not assume equal variance. We are able to reject the null hypothesis for all parameters, except the t-test for x_1.

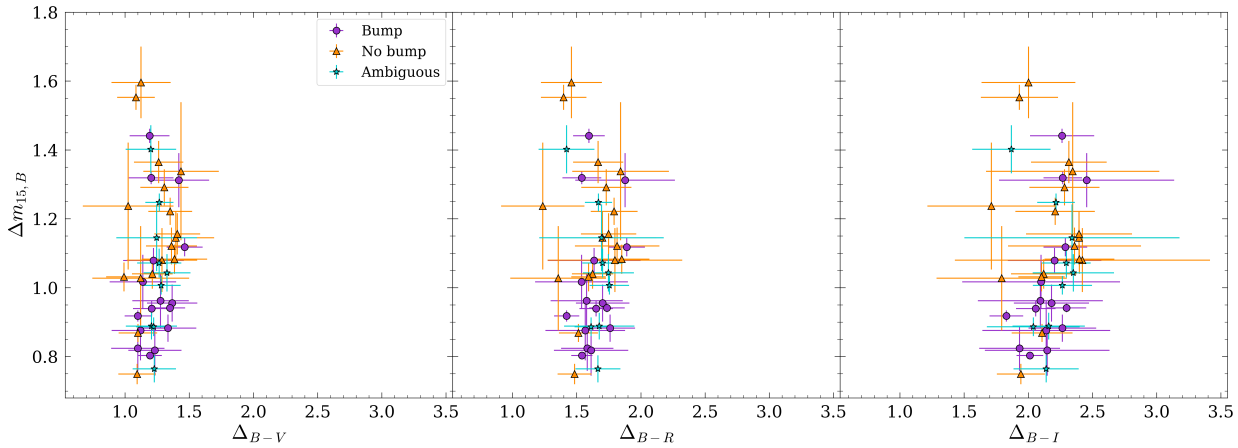

Figure 4.6: Comparison between the decline rate $\Delta m_{15,B}$ and the color-width parameters Δ_{B-V}, Δ_{B-I}, and Δ_{B-I}.

4.2 Second linear region

It is difficult to draw conclusions about the color-width parameter Δ_{X-Y} from this analysis because so many SNe did not have sufficient data in the second linear region to measure its slope (Figure 3.2). It is reasonable to expect that Δ_{X-Y} is correlated with the slope; if $\beta_{XY,1} \approx -\beta_{XY,2}$, then the CMAGIC curve should get wider with a flatter slope (i.e., $\Delta_{X-Y} \propto 1/\beta_{XY,1}$). The data may reflect this expectation (Figure 4.5), but more data are necessary to verify or disprove this. There is no discernible relationship between $\Delta m_{15,B}$ and Δ_{X-Y} (Figure 4.6). It does appear that Δ_{X-Y} has a narrow distribution (Figure 4.6). At this time, it is unclear if this is a result of the method used to make up for the lack of data in the second linear region (3.3.3) or if this is an inherent property of Δ_{X-Y}. A dataset constructed specifically to investigate this is needed due to the general lack of observations in the 30–60 day range (Section 5.2).

4.3 Spectral features

SNe with a bump tend to have a smaller $\Delta m_{15,B}$ than SNe without a bump. In addition to the previously discussed photometrically-derived quantities, the results of this analysis show that SNe with a bump *also* have spectral features that reflect a slower decline rate.

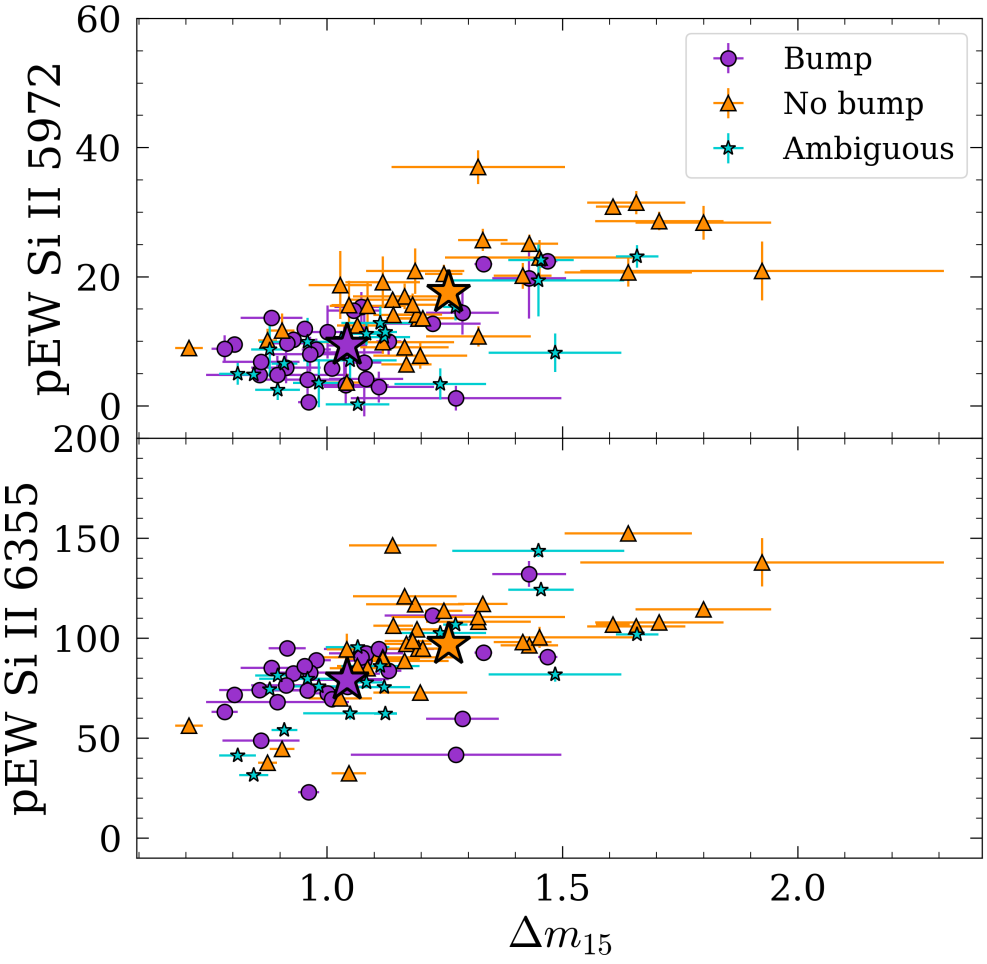

Figure 4.7: The decline rate Δm_{15} compared to the pEW of the Si II λ6355 and λ5972. The purple and orange stars indicate the centroids of the bump and no bump samples, respectively.

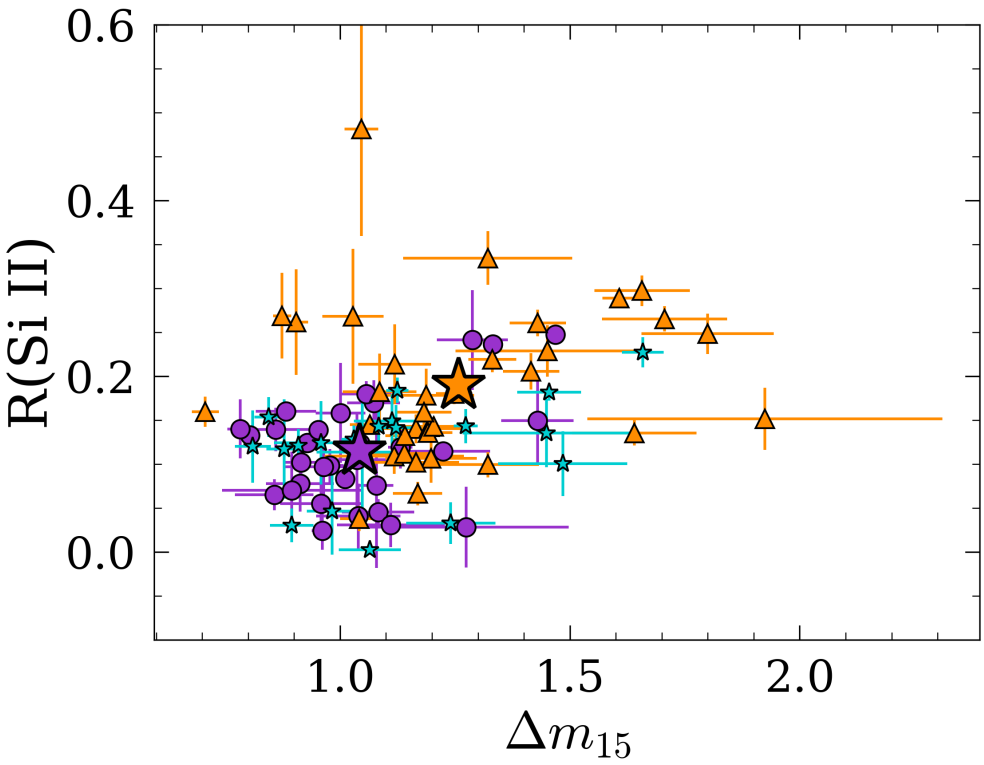

Figure 4.8: The ratio of the strengths of the Si II λ5972 absorption feature to that of the λ6355 feature [4, 5, 6]. The purple and orange stars indicate the centroids of the bump and no bump samples, respectively.

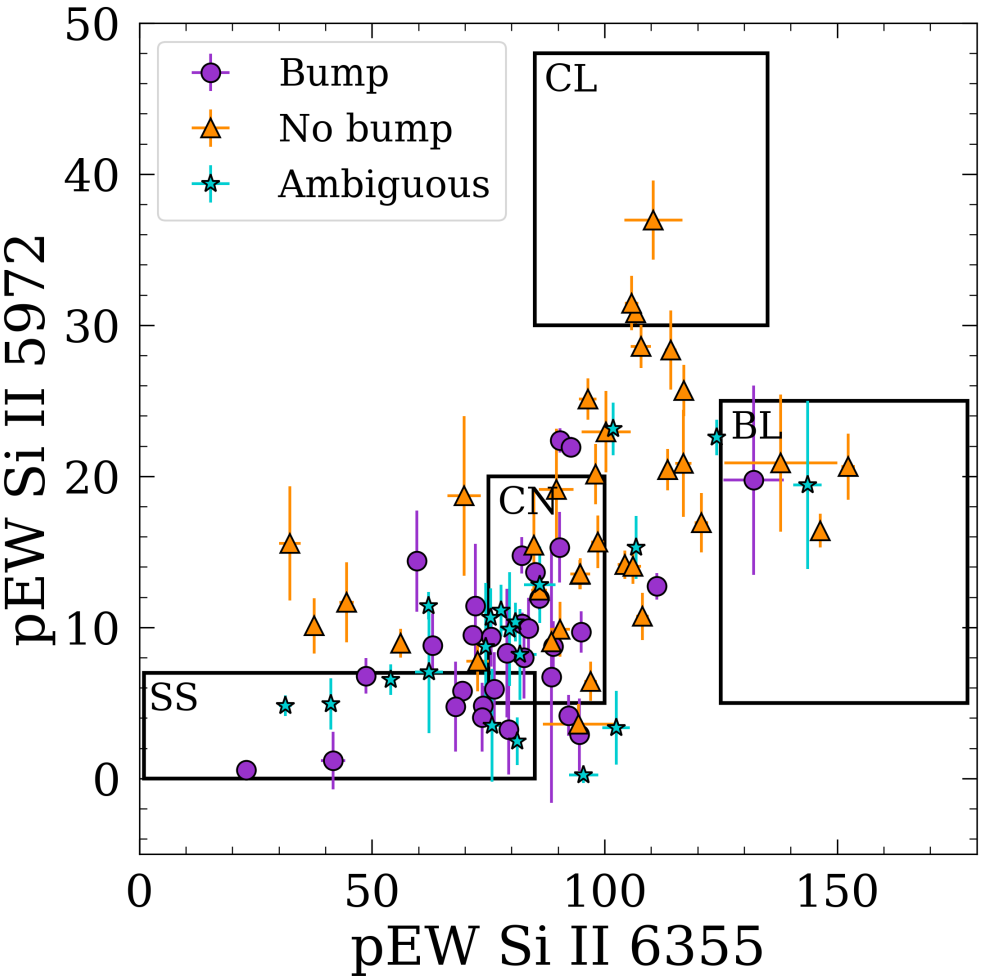

Figure 4.9: A "Branch diagram" [1] for the SNfactory SNe in this sample. Approximate outlines of each Branch subtype are drawn, based on the original publication. No conclusions are drawn based off this plot.

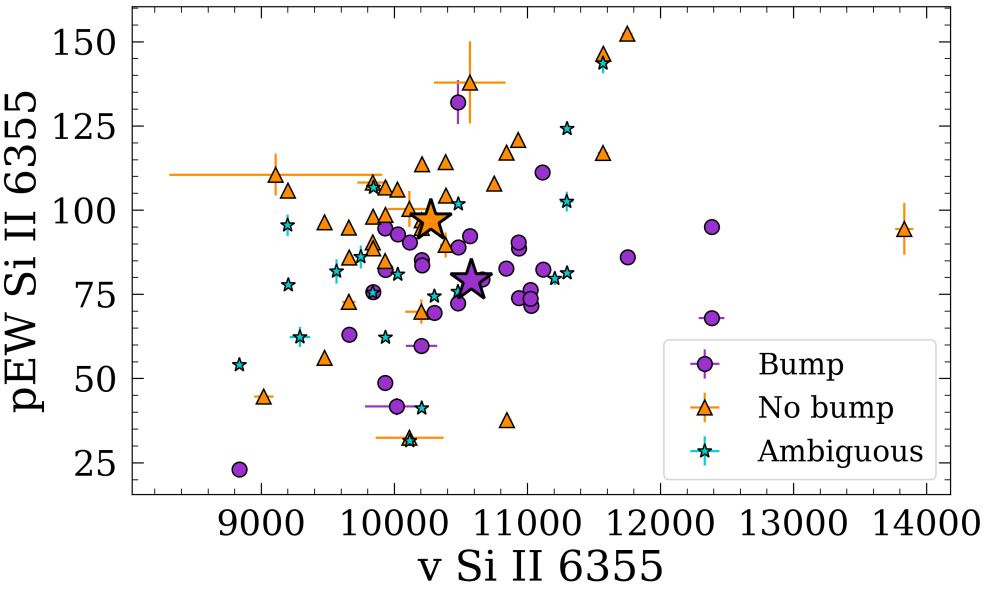

Figure 4.10: Pseudo-equivalent width of the Si II λ6355 absorption line compared to the ejecta velocity measured from the same line. Purple and orange stars represent the centroids of the "bump" and "no bump" groups, respectively. Almost all SNe are within the range of normal SNe in this plot [7]. Note that the "bump" and "no bump" samples separate along a diagonal line.

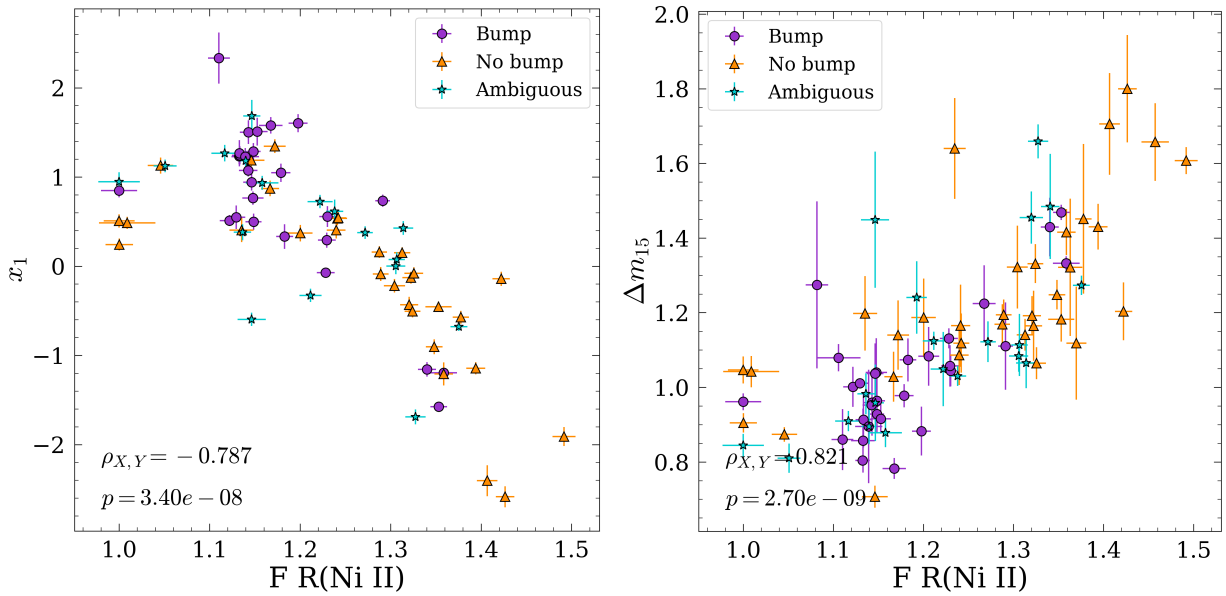

Figure 4.11: *Left*: The SALT3 stretch x_1 [3] compared to the flux ratio F R(Ni II). *Right*: The decline rate Δm_{15} compared to the flux ratio F R(Ni II). For both panels, $\rho_{X,Y}$ is the Pearson correlation coefficient and p is the associated $p-$value.

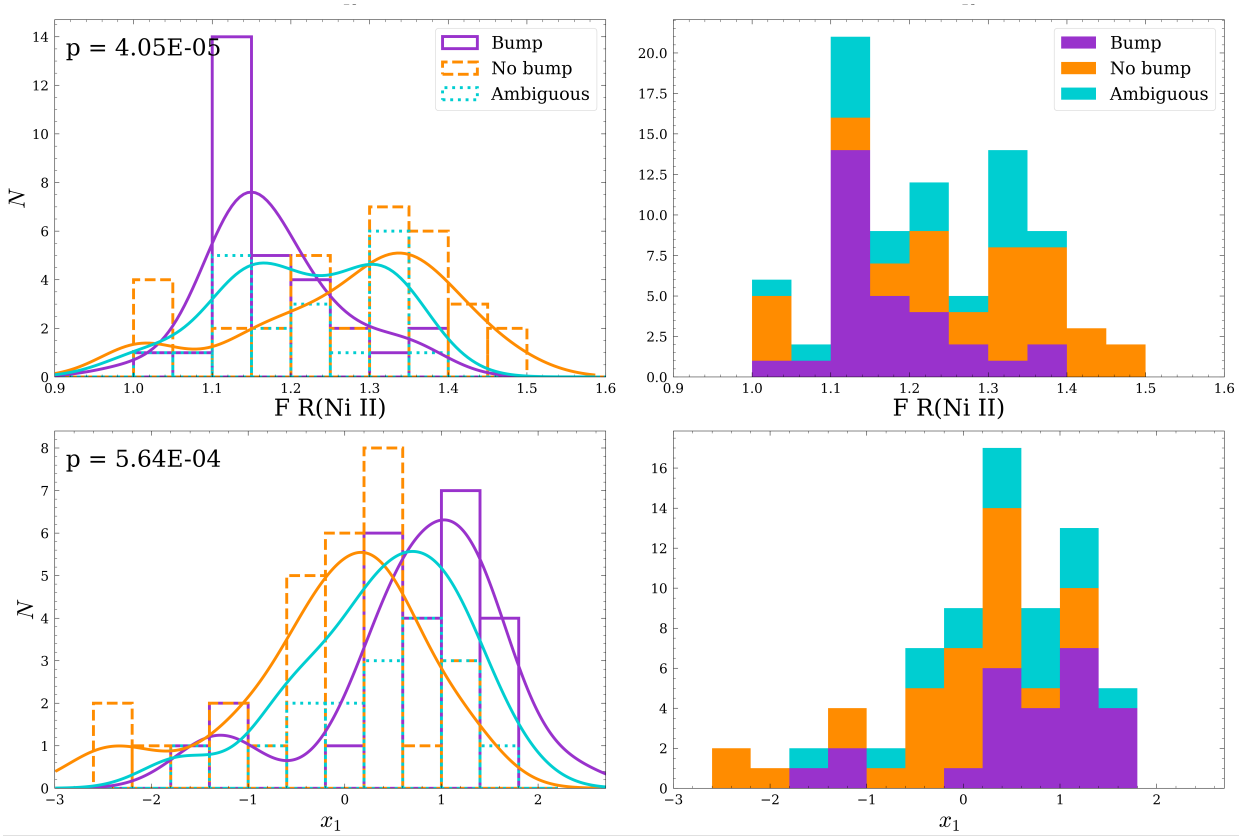

Figure 4.12: The same as Figure 4.3, but for the flux ratio F R(Ni II) and SALT3 stretch x_1.

Si II line strength is known to be associated with decline rate. Specifically, SNe Ia that dim at a slower rate than others tend to have weaker Si II lines [4, 5, 6]. Figure 4.7 shows that the SNe in this analysis follow the expected trend that SNe with small $\Delta m_{15,B}$ tend to have weaker Si II absorption features. Additionally, Figure 4.8 shows that the ratio of the strength of the Si II λ5972 to the strength of the absorption feature at λ6355 at maximum brightness follows the expected trend that larger $\Delta m_{15,B}$ has a larger ratio, R(Si II) [4, 5, 6].

We find that the flux ratio F R(Ni II), which is known to be associated with ^{56}Ni mass [36], is highly correlated with both Δm_{15} and the SALT3 stretch x_1 [3] (Figure 4.11). This result is expected, but confirms that this flux ratio can be used as a handle on SN Ia physics, and has potential to be used in standardization for cosmological studies (Section 4.6). We also find that larger F R(Ni II) is associated with bump presence (Figure 4.12). This is in line with previous results; it has been shown that a larger F R(Ni II) is associated with a lower ^{56}Ni mass [36]. Thus, we can expect that if SNe Ia with a larger F R(Ni II) value have less ^{56}Ni mass, they should also have a faster decline rate.

Figure 4.9 shows a "Branch diagram" [1] for the SNfactory sample presented in this work. There are no notable separations between the "bump" and "no bump" groups with respect to the Branch subtypes. All SNe appear to overlap with the expected range of core-normal (CN) SNe, with a few passing as shallow silicon (SS).

Figure 4.10 can be used to distinguish "high velocity" (HV) SNe Ia from normal SNe Ia [7]. Although nearly all SNe in this sample fall in the expected region for normal SNe, and the bump/no bump distinction is not reflected in terms of HV vs. normal, there is a sepration in the two groups diagonally across the plot. SNe without a bump tend to be in the upper-left region of the scatter, and SNe without a bump tend to be in the lower-right region of the scatter (with some exceptions). In other words, SNe with a bump tend to have stronger Si II λ6355 absorption feature that shows a slower ejecta velocity, while SNe without a bump have a weaker absorption feature and faster-moving ejecta. However, this result does not intuitively make sense, given that a larger Δm_{15} is associated with stronger

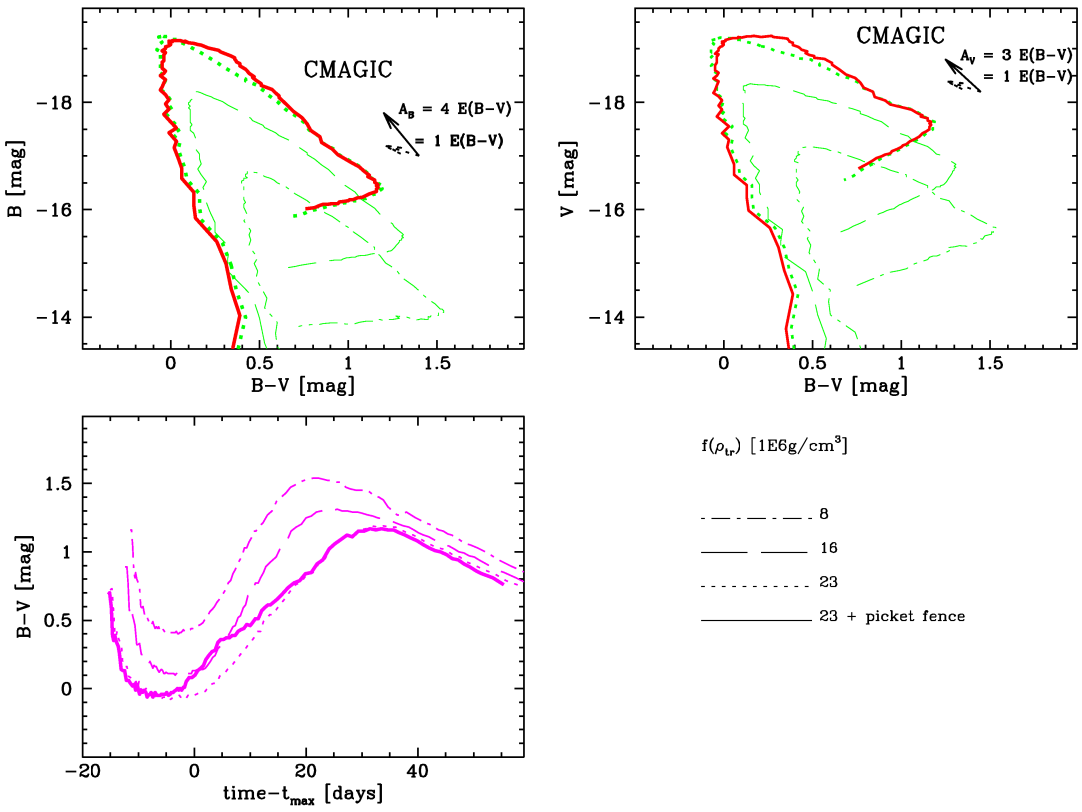

Figure 4.13: Model 23 from Hoeflich et al. 2017 [8], modified to include inhomogeneous mixing. The solid red line is the model with inhomogeneous mixing; the dotted green line immediately behind the red line is without mixing. The other lines are models without mixing at assorted transition densities, ρ_{tr}, representing a series from bright to transitional to underluminous SNe Ia with transition densities of 8, 16, and 23×10^6 g/cm^3. CMAGIC templates with different brightness shift along a line defined by the peak brightnesses. Figure from [2]. © AAS. Reproduced with permission.

absorption features [4, 5, 6] and a faster ejecta velocity [7, 37, 38]. One would expect that Figure 4.10 shows a linear relationship with the "bump" SNe at the lower end of the relation, rather than a scatter plot with a rough separation through the center. More work is needed to understand this result.

4.4 Theory

The defining features of CMAGIC diagrams of SNe Ia (the slope of the linear region and the two "turnaround" locations near $(B-V) \approx 0$ and $1 \leq (B-V) \leq 1.5$) depend on the

type of explosion and its associated physics [8, 49]. Using a 1D delayed-detonation (DDT) model [90] from Hoeflich et al. 2017 [8] (hereafter H17) for a normal-bright SN Ia, it can be shown that mixing reproduces the observed "bump" effect. In particular, inhomogeneous mixing of Si and Ni at their interface produces this result in 1D models.

The H17 model is run via the radiation-hydrodynamical code `HYDRA` [91]. Three scenarios are investigated: (a) the original, unmixed model, (b) mixing at the Si/Ni interface with large-scale inhomogeneous Rayleigh-Taylor instabilities with 50% of the material sinking and 50% of the material rising, and (c) homogeneous mixing of the Si/Ni interface. Scenarios (a) and (b) are shown in Figure 4.13, where the solid lines represent scenario (b), and the dotted/dashed lines represent scenario (a). The solid lines show a distinct bump feature near the time of maximum brightness in the same location as observed in the data. The dotted/dashed lines confirm that the DDT transition density, ρ_{tr}, does not affect the presence of a bump in this model. However, this was included because it was previously shown that the brightness shift between CMAGIC diagrams is influenced by ρ_{tr} [8].

Scenario (c) is not plotted because homogeneous mixing results in a net opacity increase. This results in redder colors throughout the CMAGIC curve, and is reflected in the CMAGIC diagram as a shift of the entire curve to the right rather than a change in the shape of the curve itself. No bump is produced in this case.

After a SN Ia explodes, large-scale plumes of burned material form in its interior and burst through the photosphere, while denser, unburned material sinks to the center [92]. These plumes decay to smaller sizes as the deflagration proceeds [93]. At maximum brightness, the photosphere has receded to the interface of Si/Ni [94]. At this time, we may study the observational consequences of these plumes. Because the plumes without mixing are transparent and the plumes with mixing are opaque, a patchy effect is created at the photosphere with respect to transparency. Radiation escapes through the transparent unmixed regions, causing a small luminosity excess, which corresponds to the "bump" feature observed in the data. Later, once the photosphere has receded past the mixed region, some energy

has already escaped through the plumes, causing a slower rate of energy loss corresponding to the observed shallower slope in the "bump" population.

It is important to note that the large-scale Rayleigh-Taylor instabilities result in an explosion with asymmetric geometry. Thus, they may lead to observable polarization of the SN.

It is worth emphasizing again that this model is 1D, and thus, results may not reflect reality. 3D models are needed to verify these results. It is possible that a 3D model may reveal asymmetry; for example, it is unknown if a given SN Ia can show a bump at one viewing angle, but will not show one at another. If the bump is related to asymmetry, it may also suggest that the light curve decline rate is connected with geometry [95, 96, 97, 98]. Because asymmetry introduces intrinsic color and magnitude dispersion among SNe Ia [96], it is important to determine the effects, if any, of the bump feature on cosmological analyses.

It is also currently impossible to rule out interaction of the ejecta with circumstellar material as the physical cause of the bump feature. However, this is unlikely due to the previously-discussed tendency for SNe with a bump to have a slower decline rate, as well as their tendency to stay bluer for a longer amount of time after maximum brightness. These suggest that the bump feature is an intrinsic property of the SN itself, and is not due to environmental effects.

4.5 Template analysis

It is important to determine if currently-used empirical templates reproduce the features seen in the data. The fPCA [9], SNooPy [10], and SALT3 [3] templates were manually manipulated to explore the results of investigating these parameter spaces.

In order to reproduce the bump feature using light curve templates, it is important to remember that the CMAGIC diagram is time-independent if the time axis is stretched identically for all light curves. Therefore, the shapes of the light curves must be adjusted relative to one another. In this case, the width of one band was varied while leaving the width of the other band fixed (Figure 4.3, bottom row) for the fPCA and SNooPy templates.

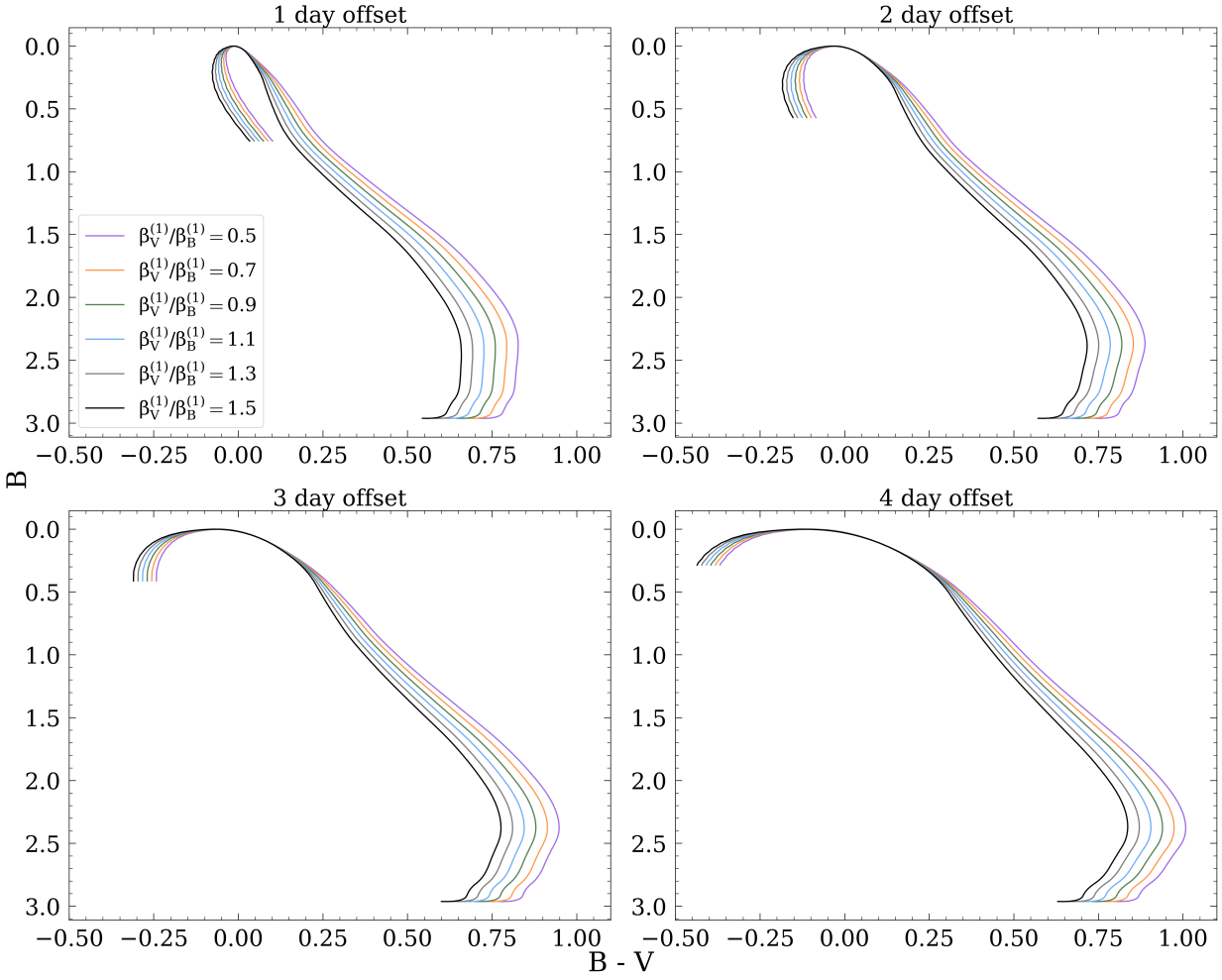

Figure 4.14: CMAGIC diagrams constructed by manually manipulating the fPCA templates used for light curve fitting in this work [9]. Each panel corresponds to a different amount of time between B_{max} and V_{max}, such that a 0 day offset is when B_{max} and V_{max} occur at the same time. Consistent with observations, the V-band is shifted to later times relative to the B-band. The different colors represent the variations of the ratio of the first PC vector in the $V-$band, $\beta_V^{(1)}$, to the first PC vector in the $B-$band. $\beta_B^{(1)}$ is held fixed at $\beta_B^{(1)} = 1$ and $\beta_V^{(1)}$ is allowed to vary. The $\beta^{(1)}$ parameter in this plot *only* does not represent the slope of the linear region in the CMAGIC diagram; this notation was chosen to be consistent with previously-used notation in literature [9]. Figure from [2]. © AAS. Reproduced with permission.

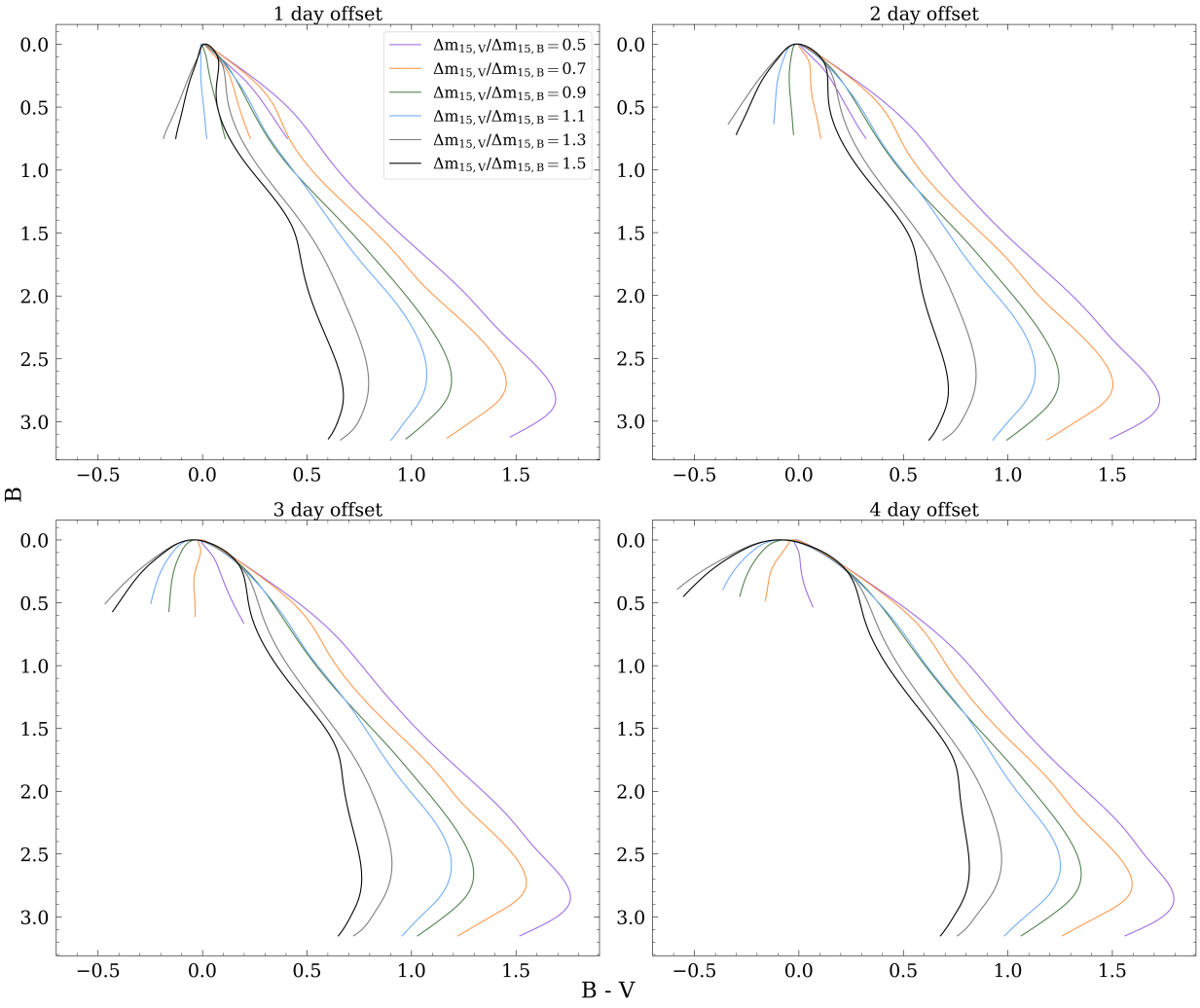

Figure 4.15: CMAGIC diagrams constructed by manually manipulating SNooPy templates [10]. Each panel corresponds to a different amount of time between B_{max} and V_{max}, such that a 0 day offset is when B_{max} and V_{max} occur at the same time. Consistent with observations, the V-band is shifted to later times relative to the B-band. The different colors represent the variations of the ratio of the decline rate in the $V-$band, $\Delta m_{15,V}$, to the decline rate in the $B-$band. $\Delta m_{15,B}$ is held fixed at $\Delta m_{15,B} = 1$ and $\Delta m_{15,V}$ is allowed to vary. Figure from [2]. © AAS. Reproduced with permission.

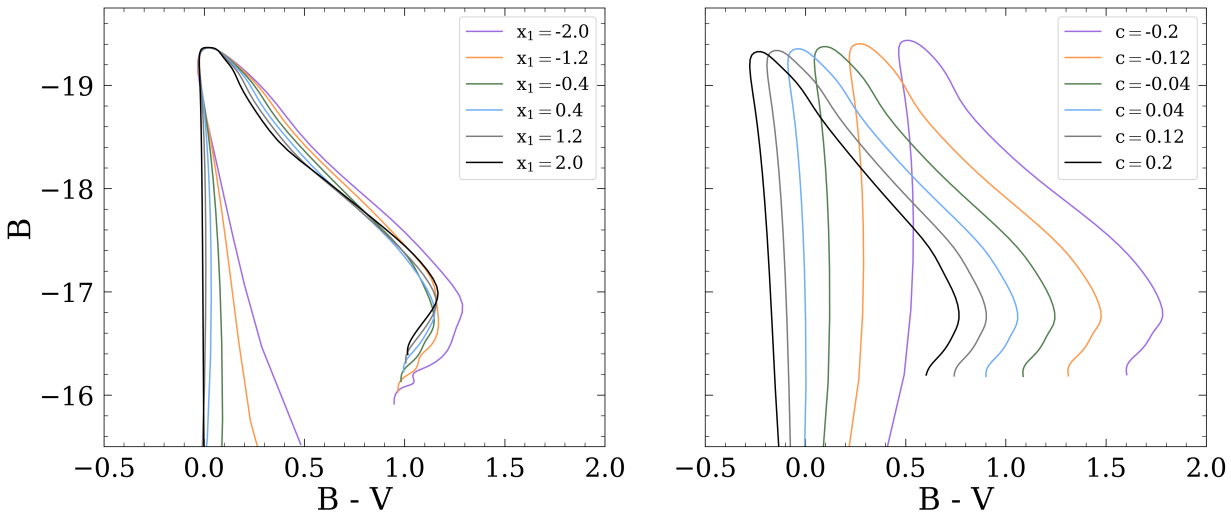

Figure 4.16: CMAGIC diagrams constructed by manually manipulating SALT3 templates [3]. *Left*: Stretch, x_1, is varied. The color term is held constant with $c = 0$. *Right*: The color term, c, is varied. Stretch is held constant at $x_1 = 1$. Figure from [2]. © AAS. Reproduced with permission.

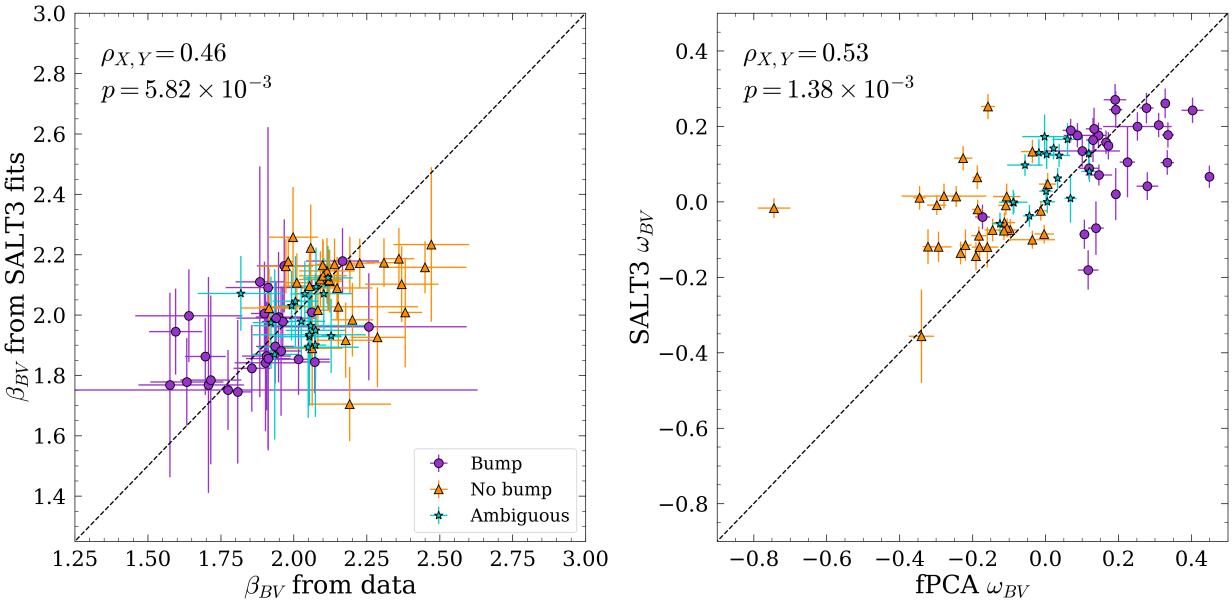

Figure 4.17: *Left*: *Left*: Slope β_{BV} measured from linear fits directly to the data compared to β_{BV} measured from a linear fit to a synthetic SALT3 CMAGIC diagram in the same phase window. *Right*: Bump size ω_{BV} measured from SALT3 fits and fPCA fits. fPCA ω_{BV} is calculated using β_{BV} from the data rather than a linear fit to the synthetic CMAGIC diagram from the fPCA templates. $\rho_{X,Y}$ is the Pearson correlation coefficient for each plot, and p is the corresponding p-value. Figure from [2]. © AAS. Reproduced with permission.

The other relative adjustment that can be made is the time offset between $B-$ and $V-$band peaks. The curves in Figure 4.14 only include the mean PC component and the first PC component; by definition, the expectation value of every component is 0. Therefore, for these purposes, the last three PC components can be excluded.

The SALT3 template is a spectral template from which synthetic photometry is produced, and thus must be treated differently. For any given parameter, that parameter applies to all photometric bands. In this case, the stretch, x_1, and color, c, parameters can be varied independently from one another. Additionally, SALT3 templates can be fit to the data, and these synthetic SALT3-derived CMAGIC diagrams can be compared to the fPCA- and data-derived quantities.

In the fPCA and SNooPy templates (Figures 4.14, 4.15), a larger time offset results in a wider bump feature, and a larger ratio results in a "sharper" bump feature. Although they do reproduce a bump feature and slope that vary in size, they tend to reproduce larger bump features with steeper slopes. This is the opposite of what is seen in the data, where a larger bump feature corresponds with a shallower slope.

The manual manipulation of the SALT3 template (Figure 4.16 shows that an increasing stretch corresponds with the presence of a bump, as well as a shallower slope. In addition to reflecting the trend seen in the data, this implies that as x_1 varies, the width of the resulting light curves do not scale together. Additionally, β_{BV} and ω_{BV} measured from synthetic SALT3 CMAGIC diagrams show the same patterns as the data- and fPCA-derived quantities (Figure 4.17). SALT3 may overpredict bump size for the "no bump" sample and underpredict bump size for the "bump" sample (Figure 4.17, right), however, these results are not conclusive and require further investigation.

It is important that future template construction considers the shape of the CMAGIC diagram while under development. Otherwise, important indicators of SN physics may be unintentionally excluded.

4.6 Hubble residuals

The results of the Hubble residual minimization in this analysis match standards set by previous literature (Table 4.3; Sections 1.2.2, 2.2.2, and references therein). We particularly note that the overall WRMS for our SALT3 minimization where $(B-V)_{max} < \infty$ is 0.14; this result is the same as the scatter reported in other work using an almost identical sample [65]. Further, we show that our fits have successfully removed correlations between the Hubble residual, $\Delta\mu$, and other quantities that are associated with SN Ia standardizable properties (Figures 4.19, 4.20, 4.21).

In terms of the "bump" and "no bump" CMAGIC categories, we see that when standardized separately, the "bump" category has a smaller WRMS than the "no bump" category (Table 4.2, $(B-V)_{max} < \infty$). When all 75 SNe are standardized together, the "bump" group still generally has a smaller or equivalent WRMS than the "no bump" group (Table 4.3). This result is unexpected; if the bump is caused by inhomogeneity in the supernova (Section 4.4), it should be a less uniform sample. However, we do note that the distribution of $\Delta m_{15,B}$ is narrower for the "bump" group than the "no bump" group (Figure 4.3, which could result in the "bump" sample being more uniform with respect to standardizability. At this time, we cannot say if this is generally true or is a property of the particular sample used in this work. We do not draw any conclusions for the $(B-V)_{max} < 0.05$ subsample when standardized separately due to the small sample sizes. These results show that SN Ia physics, even among "normal" SNe Ia, matter with respect to sample uniformity.

F R(Ni II) is an appropriate substitute for the SALT3 stretch x_1 (Table 4.3). In all cases, the results are nearly identical. Although this work shows that F R(Ni II) is correlated with both x_1 and Δm_{15}, it a more suitable replacement for x_1 because x_1 is an SED-derived quantity [27, 28, 3], whereas Δm_{15} is inherently photometric [11]. If an appropriate spectral feature can be found that correlates with c, then template-free, single-spectrum standardization can be achieved, which eliminates a source of unquantifiable uncertainty and reduces the amount of data needed to accurately calculate cosmological parameters. We do note that

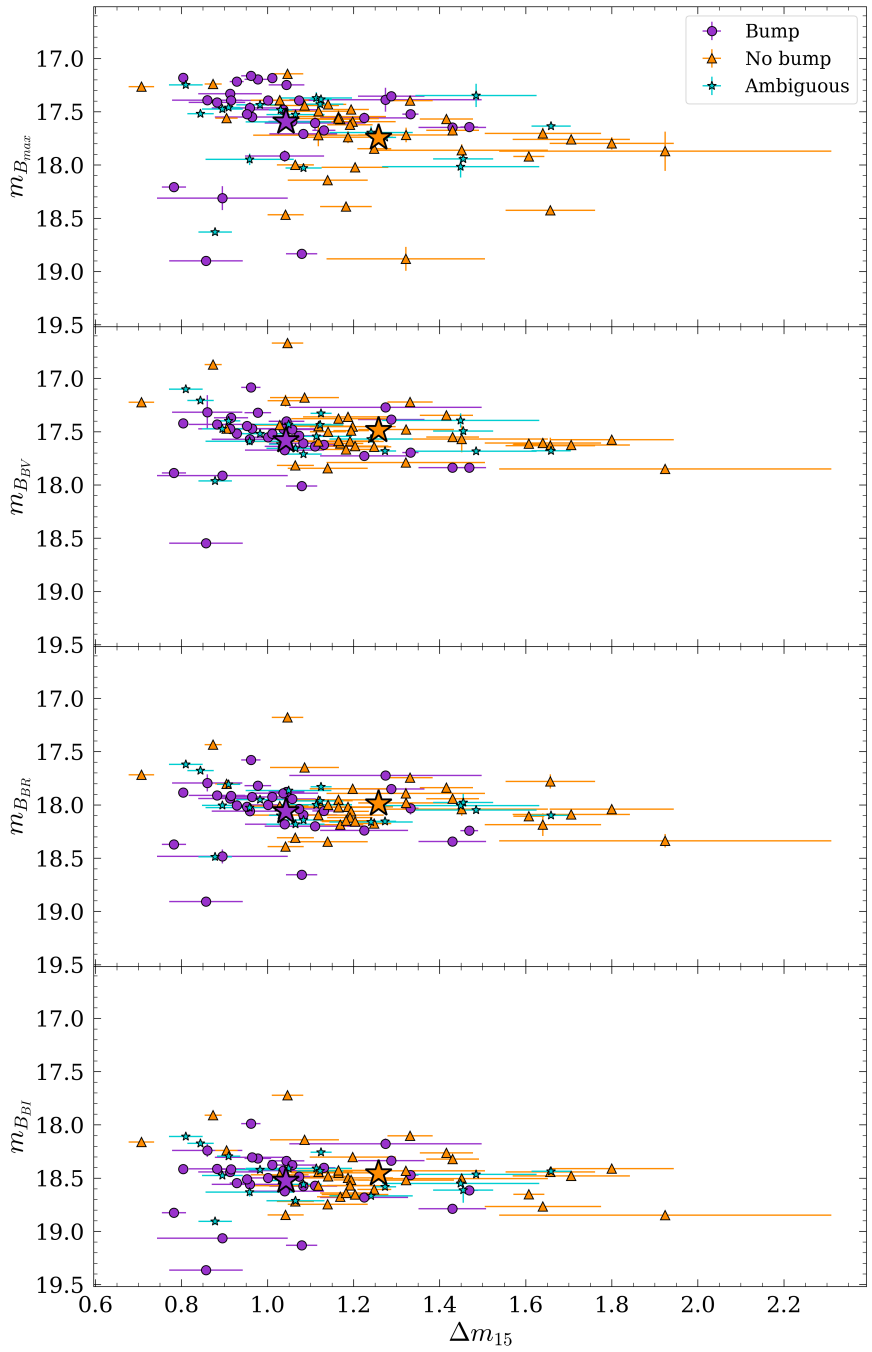

Figure 4.18: The luminosity-decline rate relationship [11] for apparent magnitudes for all SNe in the sample in this work at $z = 0.05$, using an assumed Flat ΛCDM cosmology such that $H_0 = 70$ Mpc km^{-1} s^{-1} and $\Omega_{m,0} = 0.3$. Purple, orange, and teal points are the bump, no bump, and ambiguous samples, respectively. The purple and orange stars are the centroids of the bump and no bump groups. It is clear from this plot that the CMAGIC magnitudes, $M_{B_{BV}}$, $M_{B_{BR}}$, and $M_{B_{BI}}$ are less correlated with luminosity than $M_{B_{max}}$.

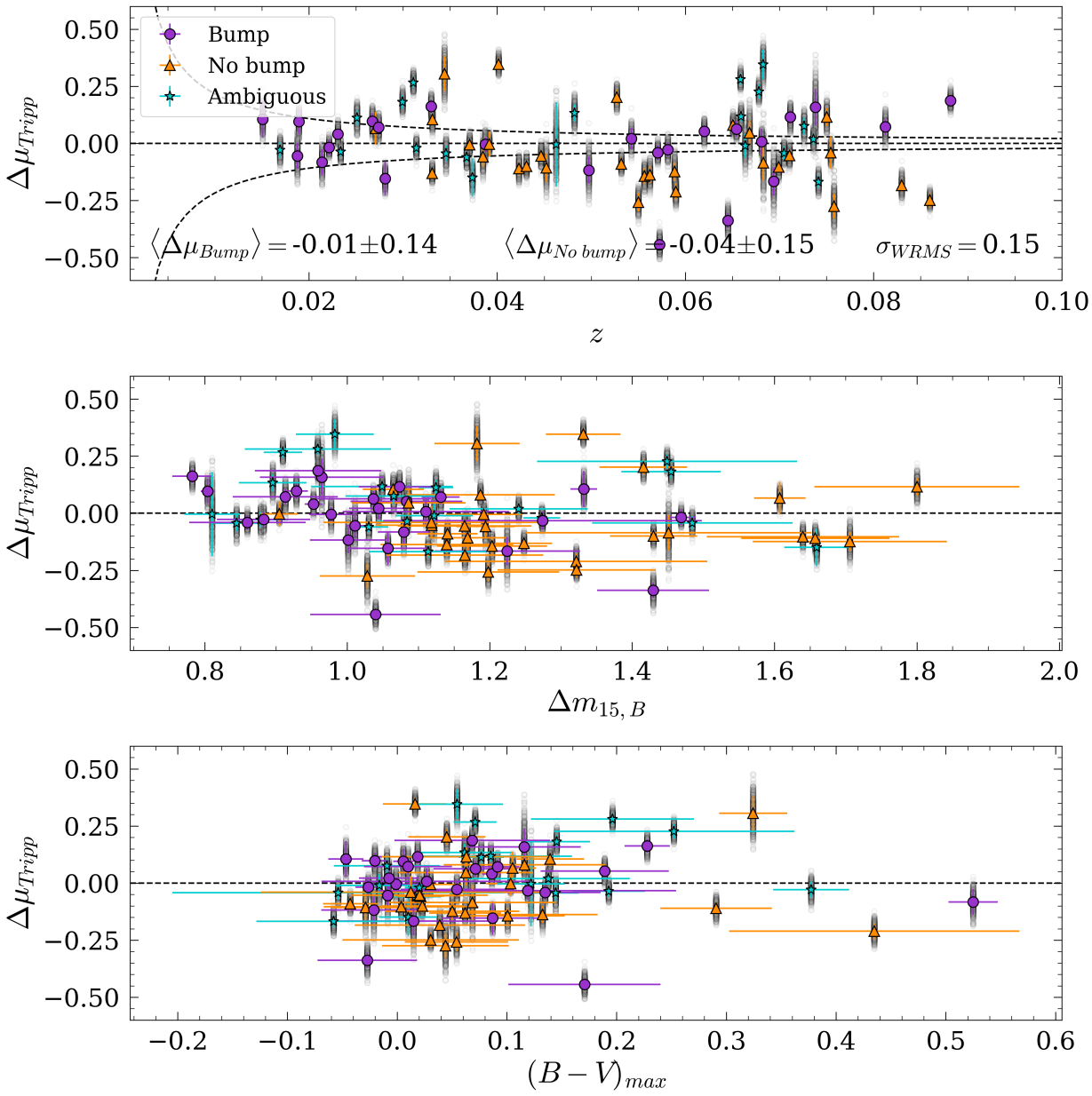

Figure 4.19: Results from the Tripp distance modulus model (Equation 3.28 [12, 13]. Purple circles represent the "bump" sample, orange triangles represent the "no bump" sample, and teal stars represent the "ambiguous" sample for $(B-V)_{max} < \infty$. All SNe have been standardized together (Table 4.3). The vertical grey smudges behind the points are all results from the MCMC procedure (Appendix B.4).

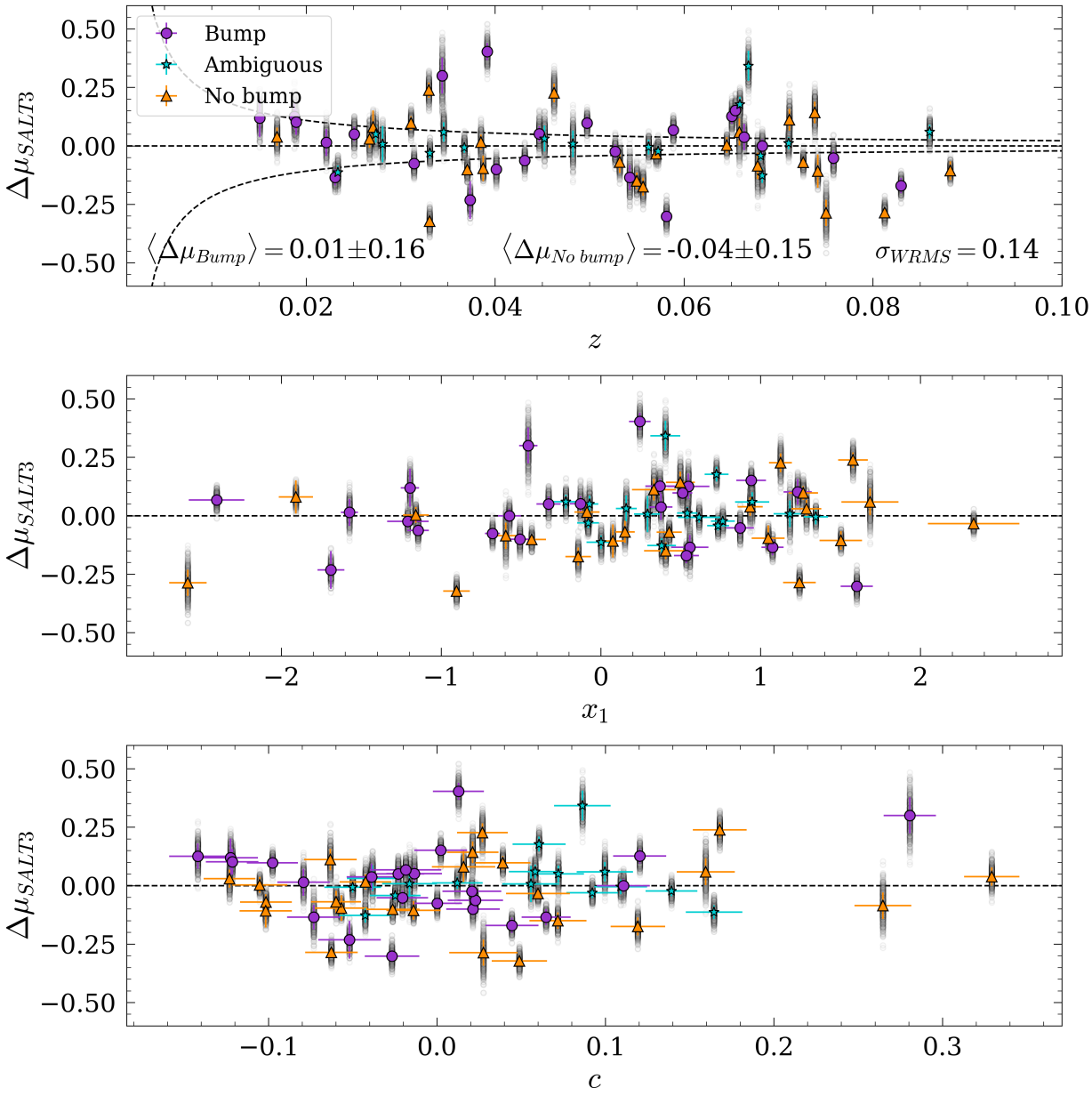

Figure 4.20: The same as Figure 4.19, but for the SALT3 distance modulus model (Equation 3.29).

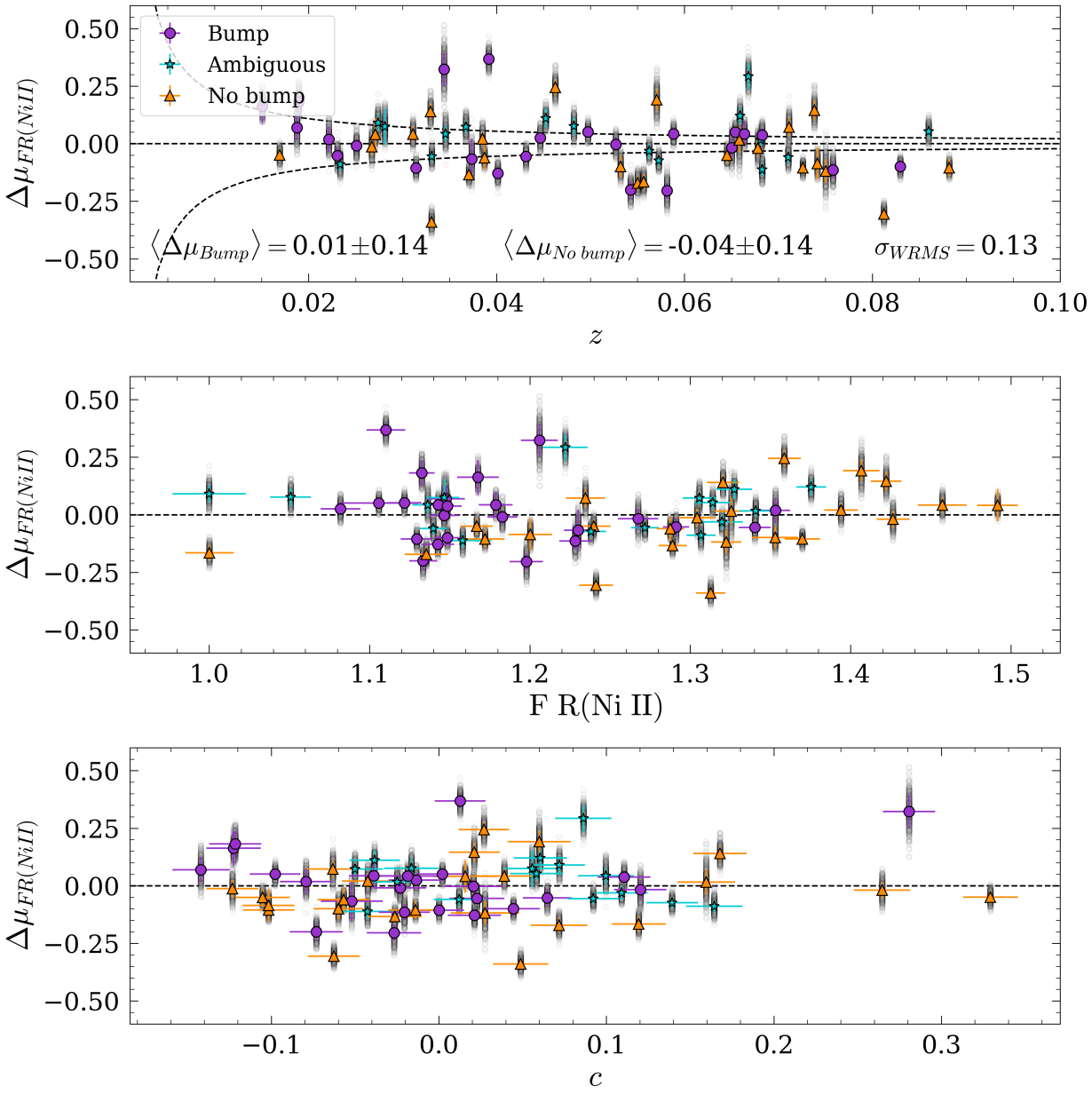

Figure 4.21: The same as Figure 4.19, but for the R (Ni II) distance modulus model (Equation 3.30).

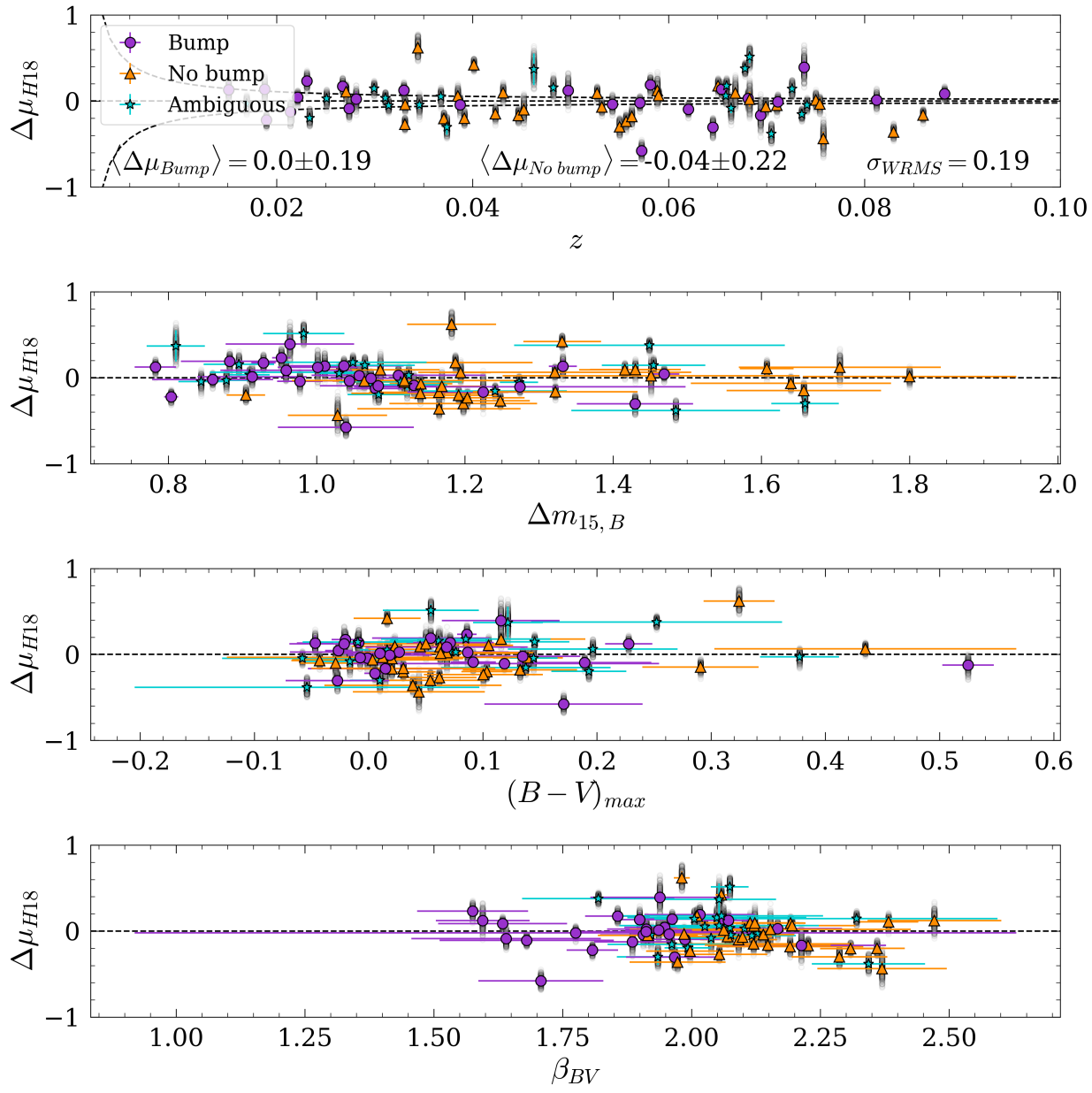

Figure 4.22: The same as Figure 4.19, but for the H18 distance modulus model (Equation 3.31).

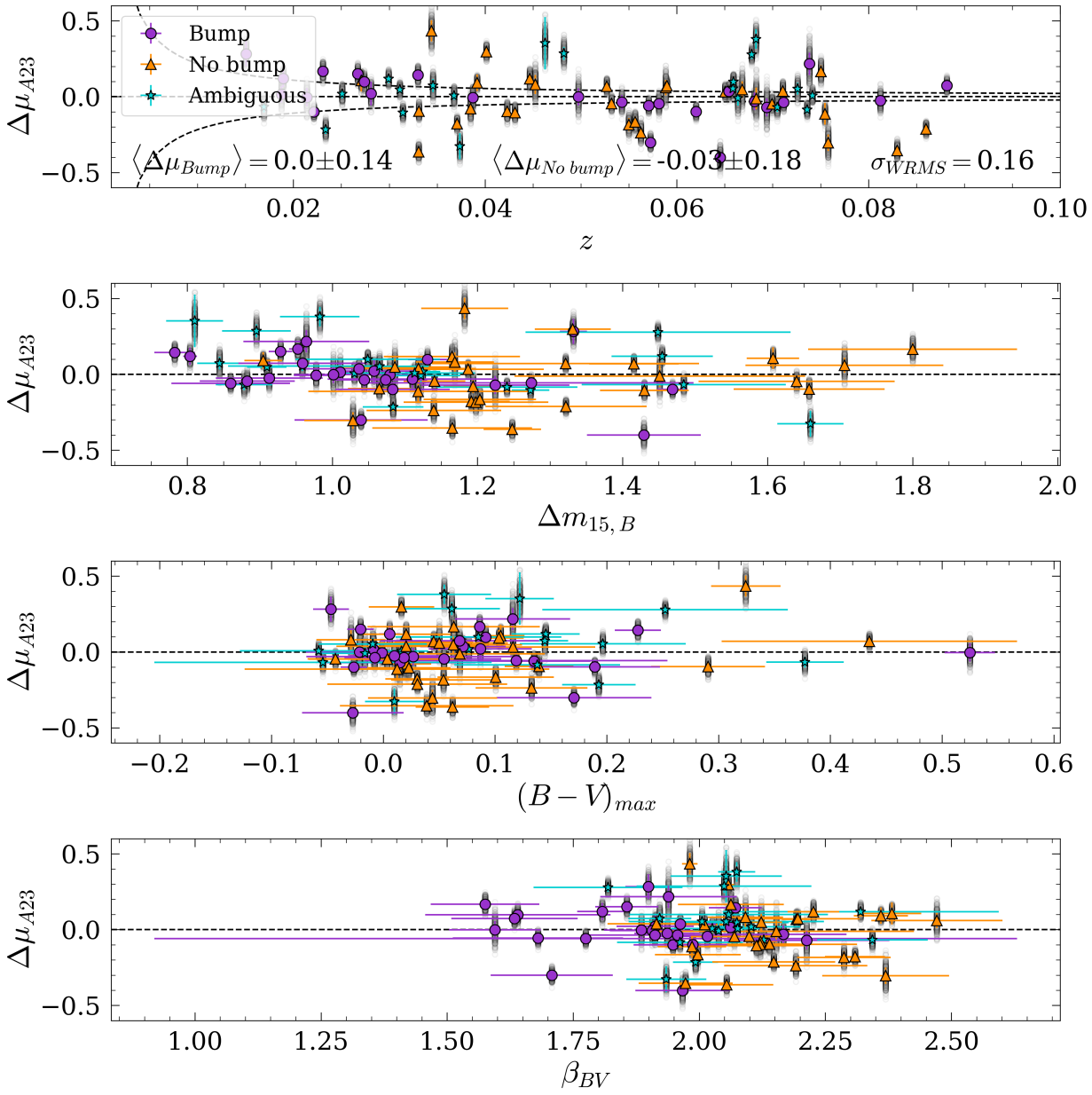

Figure 4.23: The same as Figure 4.19, but for the distance model introduced in this work (A23, Equation 3.32).

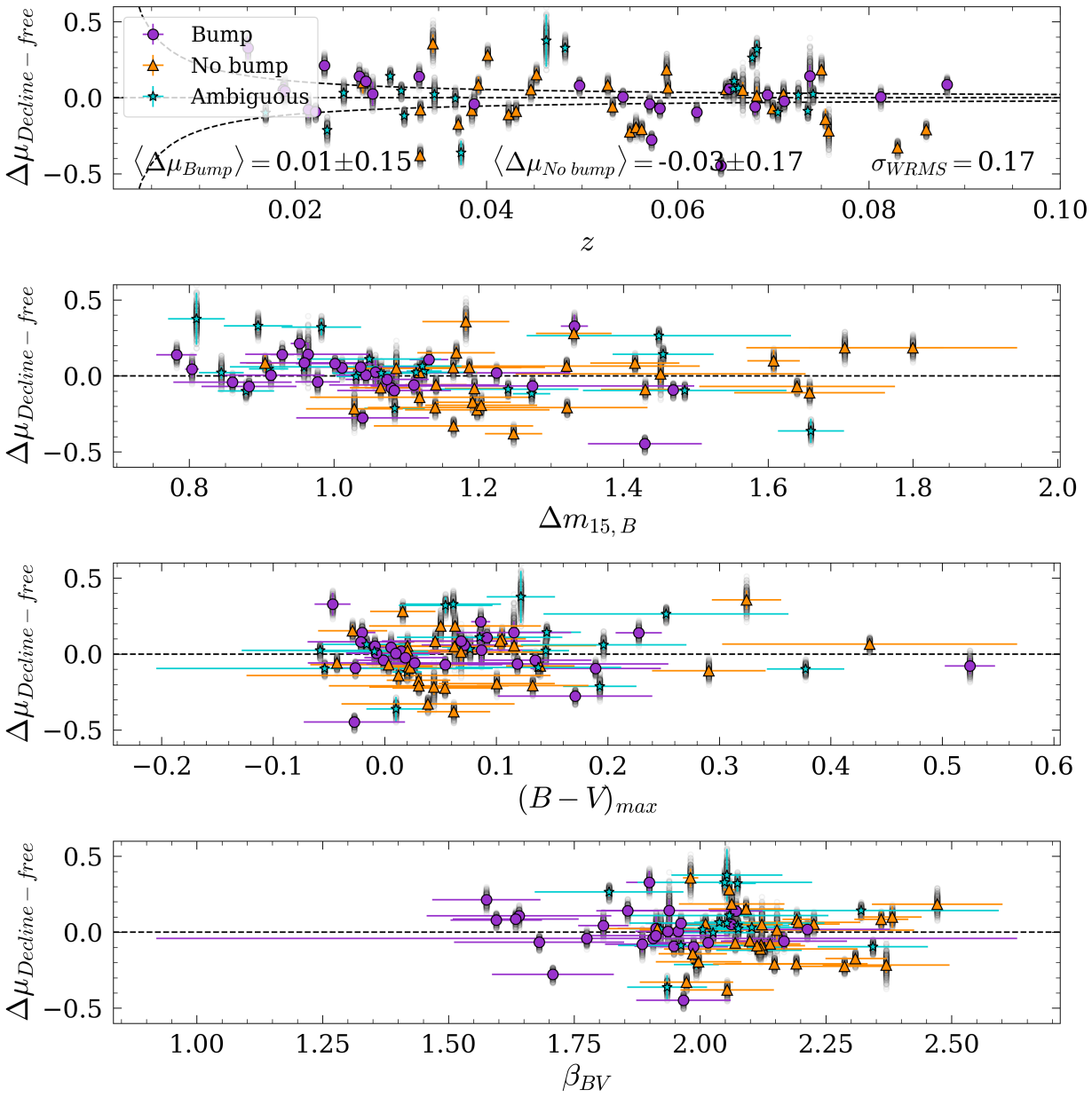

Figure 4.24: The same as Figure 4.19, but for the distance model introduced in this work (A23, Equation 3.33).

Model	Bump WRMS	No bump WRMS	Overall WRMS
$(B-V)_{max} < 0.05$, $N = 34$			
Tripp [12]	0.06	0.12	0.12
SALT3 [3]	0.07	0.12	0.10
F R(Ni II) [36]	0.10	0.10	0.09
H18 [9]	0.08	0.12	0.11
A23 (This work)	0.07	0.11	0.10
A23, Δm_{15}-free	0.10	0.13	0.12
$(B-V)_{max} < \infty$, $N = 75$			
Tripp [12]	0.17	0.15	0.15
SALT3 [3]	0.15	0.17	0.14
F R(Ni II) [36]	0.12	0.17	0.13
H18 [9]	0.18	0.21	0.19
A23 (This work)	0.15	0.18	0.16
A23, Δm_{15}-free	0.18	0.18	0.17

Table 4.2: WRMS of the Hubble residual for the three models examined in this work. N represents the total number of SNe used for each cut. Likelihoods were minimized for the entire data set, not for the "bump" and "no bump" categories separately. WRMS for these were calculated *after* minimization. The samples represent the MCMC likelihood minimization procedure applied directly to the data described in Section 3.5. Note that for SALT3 and F R(Ni II), $N = 64$ for $(B-V) < \infty$ and $N = 30$ for $(B-V) < 0.05$ because not all SNe had valid SALT3 fits.

there is a correlation between α and M (Figure C.5), where there is not a correlation between α and M for the SALT3 model (Figure C.3). This may suggest that F R(Ni II) encodes information associated with the fit absolute magnitude M. However, it is more likely that this correlation is associated with the MCMC algorithm itself; the assumed posterior distribution may be appropriate for x_1, but not for F R(Ni II). Then, because each starting value in the Markov chain depends on the value of the previous one, an inappropriate distribution assumption may lead to the value of one parameter "following" another.

Model	Bump WRMS	No bump WRMS
$(B-V)_{max} < 0.05$, $N_{bump} = 13$, $N_{No\ bump} = 14$		
Tripp [12]	0.08	0.11
SALT3 [3]	0.09	0.09
F R(Ni II) [36]	0.11	0.09
H18 [9]	0.12	0.10
A23 (This work)	0.08	0.09
A23, Δm_{15}-free	0.17	0.10
$(B-V)_{max} < \infty$, $N_{bump} = 26$, $N_{No\ bump} = 29$		
Tripp [12]	0.12	0.14
SALT3 [3]	0.10	0.15
F R(Ni II) [36]	0.12	0.15
H18 [9]	0.16	0.19
A23 (This work)	0.13	0.15
A23, Δm_{15}-free	0.16	0.16

Table 4.3: WRMS of the Hubble residual for the three models examined in this work. N represents the total number of SNe used for each cut. Likelihoods were minimized for the "bump" and "no bump" categories separately. WRMS for these were calculated *after* minimization. The samples represent the MCMC likelihood minimization procedure applied directly to the data described in Section 3.5. Note that for SALT3 and F R(Ni II), $N_{Bump} = 22$ and $N_{No\ bump} = 25$ for $(B-V) < \infty$. $N_{Bump} = 12$ and $N_{No\ bump} = 12$ for $(B-V) < 0.05$ because not all SNe had valid SALT3 fits.

5. CONCLUSIONS

5.1 Summary

The primary conclusions of this work are:

1. The SNFactory data—which do not require k-corrections—confirm previously-discussed CMAGIC behavior [49].

2. There is a correlation between the slope of the first linear region, β_{XY}, and the bump size, ω_{XY}, in the CMAGIC diagram (Figure 4.1).

3. Bump presence tends to be associated with a slower decline rate, as well as other observational parameters that are associated with slower decline rates (Figure 4.3, Table 4.1).

4. The bump feature may be caused by Si/Ni mixing from large Rayleigh-Taylor instabilities (Figure 4.13).

5. Current empirical templates are able to reproduce the bump feature in the CMAGIC diagram, as well as the varying slope (Figures 4.14, 4.15, 4.16, 4.17). Of the templates examined in this work, the SALT3 template is most reflective of observations because as the stretch parameter x_1 is varied, the slope of the linear region decreases while the bump size increases (Figure 4.16, 4.17).

6. The flux ratio F R(Ni II) [36] is correlated with $\Delta m_{15,B}$ [11] and the SALT3 stretch x_1 [3], and is an appropriate substitute for the purposes of cosmological analyses.

7. Conclusions cannot be drawn about the color-width parameter Δ_{X-Y}. However, it does appear that the distribution of these values is fairly narrow (Figure 4.6), which may warrant further investigation.

8. The "bump" sample, in general, produces a smaller scatter in the Hubble residual regardless of whether or not the two groups are standardized separately (Tables 4.3 and 4.2).

5.2 Future work

Although this work has been presented in terms of separate "bump" and "no bump" groups as an illustrative aid, it is important to emphasize that the bump feature does not bifurcate the sample into two discrete categories. It exists on a continuum (Figures 4.1, 4.3, 4.14, 4.15, 4.16, 4.17), as is apparent from the "ambiguous" category in this work, which includes SNe that were difficult to categorize by eye, and consistently lies between the "bump" and "no bump" samples in all tests. From a theoretical perspective, there is no physical reason that there should not be a continuum of Rayleigh-Taylor instability sizes (Section 4.4). The physical cause of the bump size should also be viewed through the lens of different SN types—for example, do 91T- [99] or 91bg-like [100] objects tend to have/not have bumps, and do these objects exist on a continuum with the normal SNe Ia? Determining this observationally would be straightforward; given a sample with sufficient normal, 91bg-, and 91T-like SNe Ia, the analysis in this work could be repeated (Figures 4.1, 4.3, 4.12) and checked for (1) a continuous distribution in the bump-slope relationship, as in Figure 4.1, and (2) association of these features with photometric and spectral decline rate parameters such as $\Delta m_{15,B}$, Si II lines, and x_1.

Future work should include investigating the physical cause of the bump feature and its correlation with the slope using more complete 3D models. Parameters that could be adjusted include diffusion timescale, amount of mixing (in this work, the amount of upward material mixing was equal to the amount of downward material mixing), and magnetic field strength. It is particularly crucial to determine if the bump feature is associated with asymmetry or viewing angle. If so, SNe with a bump are more likely to be polarized. For example, there is a strong correlation between polarization and the velocity gradient for the Si II λ6355 absorption line; future studies can investigate this parameter without the need

for new observations.

In order to more rigorously check if the "bump" and "no bump" populations produce different Hubble residual results, a leave-one-out cross-validation (LOOCV) algorithm could be used. The fitting procedure is repeated N times, where N is the number of SNe in the sample. In each repetition, one unique SN is excluded from the training sample, and used as a single-item test set. The resulting test μ and residual $\Delta\mu$ are recorded. These test μ and $\Delta\mu$ values would then be used to construct a new Hubble diagram in order to verify that large variance has not affected the initial results.

This work has shown that the flux ratio F R(Ni II) [36] is a good substitute for x_1 and Δm_{15}. However, there is another spectral quantity that has been shown to correlate well with x_1; the pseudo-equivalent width (pEW) of the absorption line at 4131Å, which is in the same blended feature, is also highly correlated with the stretch [32, 33]. It would be interesting to do a comparative study and determine which of these very similar quantities, if either, provides more accurate standardization.

It would be useful to develop a standardization technique using the second linear region of the CMAGIC diagram. As a supernova explodes, observations are able to peer deeper into the ejecta as the photosphere recedes, unveiling spectral features that are emblematic of different subtypes [100, 99, 1, 101, 102]. Given that supernova diversity is revealed rather than obscured as time passes, if data at later times are used rather than data near maximum brightness for these standardizable candles, it may be possible to make more stringent cuts on the requirements for a "normal" SN Ia, reducing the uncertainty associated with SN Ia diversity. Standardization at later times would have strategic observational advantages, as well; once data from LSST and the Vera C. Rubin Observatory and *Roman* survey become available, in general, applying CMAGIC as a standardization technique is ideal because the light curves do not need to be sampled with high cadence. If SNe Ia can be standardized in not one, but two regions of the CMAGIC diagram, then many sparsely-sampled SNe Ia become available for use in cosmological analyses. The disadvantage of standardizing at much

later times is that SNe are around 3 mag dimmer than they are at maximum brightness. This is not a problem for nearby SNe Ia, but may prevent use of this technique at higher z.

If CMAGIC standardization methods continue to be utilized in the literature, it will be important to determine if the effect of the choice of the "linear region" contributes significant error to cosmological analyses. The choice of the linear region affects the measured slope, β_{XY}, which is used directly in CMAGIC distance modulus models (Equations 3.31, 3.32, and 3.33). A standard procedure for choosing this region does not currently exist. Development of these methods would be useful for both error reduction and applying CMAGIC to larger datasets that cannot be manually inspected due to volume.

These results would be improved by using a dataset with more well-sampled SNe Ia in the window 0–60 days after maximum brightness. It is difficult to find a sample with appropriate observational cadence after 30 days in particular, hence the need to develop the proxy Δ_{X-Y} for the slope of the second linear region (Section 3.3.1). Due to the difficulty measuring the slope in this region, results in this work based on Δ_{X-Y} must be considered inconclusive. A cosmological study involving the second linear region would certainly require new observations. This dataset would not only need to have a well-sampled 30–60 day region, but it would also need a well-sampled -5–30 day region to ensure consistency of results with previous methods.

Upcoming surveys like *Roman* and LSST are expected to discover 10^4 and 10^5 SNe Ia, respectively. With data sets of this size, systematic uncertainties in cosmological analyses will vastly outweigh statistical uncertainty. Thus, it is imperative that SN Ia variations, such as those described in this work, are understood. Observable indicators of underlying SN physics can be leveraged to construct a homogeneous sample that is tailored for cosmological precision. Going forward, the CMAGIC "bump" feature should be included in these considerations; as shown in this work, it has the potential to be a powerful asset in studying SN Ia physics, and therefore, deserves attention in preparation for future surveys.

REFERENCES

[1] D. Branch, L. Dang, N. Hall, W. Ketchum, M. Melakayil, J. Parrent, M. Troxel, D. Casebeer, D. Jeffery, and E. Baron, "Comparative Direct Analysis of Type Ia Supernova Spectra. II. Maximum Light," *Publications of the Astronomical Society of the Pacific*, vol. 118, pp. 560–571, apr 2006.

[2] L. Aldoroty, L. Wang, P. Hoeflich, J. Yang, N. Suntzeff, G. Aldering, P. Antilogus, C. Aragon, S. Bailey, C. Baltay, S. Bongard, K. Boone, C. Buton, Y. Copin, S. Dixon, D. Fouchez, E. Gangler, R. Gupta, B. Hayden, M. Karmen, A. G. Kim, M. Kowalski, D. Küsters, P. F. Léget, F. Mondon, J. Nordin, R. Pain, E. Pecontal, R. Pereira, S. Perlmutter, K. A. Ponder, D. Rabinowitz, M. Rigault, D. Rubin, K. Runge, C. Saunders, G. Smadja, N. Suzuki, C. Tao, R. C. Thomas, and M. Vincenzi, "Bump Morphology of the CMAGIC Diagram," *ApJ*, vol. 948, p. 10, May 2023.

[3] W. D. Kenworthy, D. O. Jones, M. Dai, R. Kessler, D. Scolnic, D. Brout, M. R. Siebert, J. D. R. Pierel, K. G. Dettman, G. Dimitriadis, R. J. Foley, S. W. Jha, Y. C. Pan, A. Riess, S. Rodney, and C. Rojas-Bravo, "SALT3: An Improved Type Ia Supernova Model for Measuring Cosmic Distances," *arXiv e-prints*, p. arXiv:2104.07795, Apr. 2021.

[4] P. Nugent, M. Phillips, E. Baron, D. Branch, and P. Hauschildt, "Evidence for a Spectroscopic Sequence among Type 1a Supernovae," *ApJ*, vol. 455, p. L147, Dec. 1995.

[5] S. Benetti, "The Diversity of Type Ia Supernovae," in *1604-2004: Supernovae as Cosmological Lighthouses* (M. Turatto, S. Benetti, L. Zampieri, and W. Shea, eds.), vol. 342 of *Astronomical Society of the Pacific Conference Series*, p. 235, Dec. 2005.

[6] S. Hachinger, P. A. Mazzali, and S. Benetti, "Exploring the spectroscopic diversity of type ia supernovae," *MNRAS*, vol. 370, pp. 299–318, July 2006.

[7] X. Wang, A. V. Filippenko, M. Ganeshalingam, W. Li, J. M. Silverman, L. Wang, R. Chornock, R. J. Foley, E. L. Gates, B. Macomber, F. J. D. Serduke, T. N. Steele, and D. S. Wong, "Improved Distances to Type Ia Supernovae with Two Spectroscopic Subclasses," *ApJ*, vol. 699, pp. L139–L143, July 2009.

[8] P. Hoeflich, E. Y. Hsiao, C. Ashall, C. R. Burns, T. R. Diamond, M. M. Phillips, D. Sand, M. D. Stritzinger, N. Suntzeff, C. Contreras, K. Krisciunas, N. Morrell, L. Wang, P. Hoeflich, E. Y. Hsiao, C. Ashall, C. R. Burns, T. R. Diamond, M. M. Phillips, D. Sand, M. D. Stritzinger, N. Suntzeff, C. Contreras, K. Krisciunas, N. Morrell, and L. Wang, "Light and Color Curve Properties of Type Ia Supernovae: Theory Versus Observations," *ApJ*, vol. 846, p. 58, aug 2017.

[9] S. He, L. Wang, and J. Z. Huang, "Characterization of Type Ia Supernova Light Curves Using Principal Component Analysis of Sparse Functional Data," *The Astrophysical Journal*, vol. 857, p. 110, apr 2018.

[10] C. R. Burns, M. Stritzinger, M. M. Phillips, E. Y. Hsiao, C. Contreras, S. E. Persson, G. Folatelli, L. Boldt, A. Campillay, S. Castellón, W. L. Freedman, B. F. Madore, N. Morrell, F. Salgado, and N. B. Suntzeff, "The Carnegie Supernova Project: Intrinsic Colors of Type Ia Supernovae," *ApJ*, vol. 789, p. 32, July 2014.

[11] M. M. Phillips, "The Absolute Magnitudes of Type IA Supernovae," *ApJ*, vol. 413, p. L105, Aug. 1993.

[12] R. Tripp, "Using distant type ia supernovae to measure the cosmological expansion parameters.," *A&A*, vol. 325, pp. 871–876, Sept. 1997.

[13] R. Tripp, "A two-parameter luminosity correction for Type IA supernovae," *A&A*, vol. 331, pp. 815–820, Mar. 1998.

[14] M. Bessell and S. Murphy, " Spectrophotometric Libraries, Revised Photonic Passbands, and Zero Points for UBVRI , Hipparcos , and Tycho Photometry ," *Publications of the Astronomical Society of the Pacific*, vol. 124, pp. 140–157, feb 2012.

[15] S. Chandrasekhar, "The Maximum Mass of Ideal White Dwarfs," *ApJ*, vol. 74, p. 81, July 1931.

[16] F. Zwicky, "Supernovae," in *Stellar Structure - Stars and Stellar Systems* (L. H. Aller and D. B. McLaughlin, eds.), p. 367, Jan. 1965.

[17] Y. P. Pskovskii, "The Photometric Properties of Supernovae.," *Soviet Astronomy*, vol. 11, pp. 63–+, Aug. 1967.

[18] A. G. Riess, W. H. Press, and R. P. Kirshner, "A Precise Distance Indicator: Type Ia Supernova Multicolor Light-Curve Shapes," *The Astrophysical Journal*, vol. 473, pp. 88–109, dec 1996.

[19] G. Goldhaber, D. E. Groom, A. Kim, G. Aldering, P. Astier, A. Conley, S. E. Deustua, R. Ellis, S. Fabbro, A. S. Fruchter, A. Goobar, I. Hook, M. Irwin, M. Kim, R. A. Knop, C. Lidman, R. McMahon, P. E. Nugent, R. Pain, N. Panagia, C. R. Pennypacker, S. Perlmutter, P. Ruiz-Lapuente, B. Schaefer, N. A. Walton, and T. York, "Timescale Stretch Parameterization of Type Ia Supernova B-Band Light Curves," *ApJ*, vol. 558, pp. 359–368, Sept. 2001.

[20] A. G. Riess, A. V. Filippenko, P. Challis, A. Clocchiatti, A. Diercks, P. M. Garnavich, R. L. Gilliland, C. J. Hogan, S. Jha, R. P. Kirshner, B. Leibundgut, M. M. Phillips, D. Reiss, B. P. Schmidt, R. A. Schommer, R. C. Smith, J. Spyromilio, C. Stubbs, N. B. Suntzeff, and J. Tonry, "Observational Evidence from Supernovae for an Accelerating Universe and a Cosmological Constant," *The Astronomical Journal*, vol. 116, pp. 1009–1038, sep 1998.

[21] S. Perlmutter, G. Aldering, G. Goldhaber, R. A. Knop, P. Nugent, P. G. Castro, S. Deustua, S. Fabbro, A. Goobar, D. E. Groom, I. M. Hook, A. G. Kim, M. Y. Kim, J. C. Lee, N. J. Nunes, R. Pain, C. R. Pennypacker, R. Quimby, C. Lidman, R. S. Ellis, M. Irwin, R. G. McMahon, P. Ruiz-Lapuente, N. Walton, B. Schaefer, B. J. Boyle, A. V. Filippenko, T. Matheson, A. S. Fruchter, N. Panagia, H. J. M. Newberg,

W. J. Couch, and T. S. C. Project, "Measurements of Ω and Λ from 42 High-Redshift Supernovae," *ApJ*, vol. 517, pp. 565–586, June 1999.

[22] S. A. Colgate and C. McKee, "Early Supernova Luminosity," *ApJ*, vol. 157, p. 623, Aug. 1969.

[23] W. D. Arnett, "On the theory of type I supernovae.," *ApJ*, vol. 230, pp. L37–L40, May 1979.

[24] W. D. Arnett, "Type I supernovae. I - Analytic solutions for the early part of the light curve," *ApJ*, vol. 253, pp. 785–797, Feb. 1982.

[25] D. Branch and J. C. Wheeler, *Supernova Explosions*. 2017.

[26] D. Kasen, F. K. Röpke, and S. E. Woosley, "The diversity of type Ia supernovae from broken symmetries," *Nature*, vol. 460, pp. 869–872, Aug. 2009.

[27] J. Guy, P. Astier, S. Nobili, N. Regnault, and R. Pain, "SALT: a spectral adaptive light curve template for type Ia supernovae," *Astronomy & Astrophysics*, vol. 443, pp. 781–791, dec 2005.

[28] J. Guy, P. Astier, S. Baumont, D. Hardin, R. Pain, N. Regnault, S. Basa, R. G. Carlberg, A. Conley, S. Fabbro, D. Fouchez, I. M. Hook, D. A. Howell, K. Perrett, C. J. Pritchet, J. Rich, M. Sullivan, P. Antilogus, E. Aubourg, G. Bazin, J. Bronder, M. Filiol, N. Palanque-Delabrouille, P. Ripoche, and V. Ruhlmann-Kleider, "SALT2: Using distant supernovae to improve the use of type la supernovae as distance indicators," *Astronomy and Astrophysics*, vol. 466, pp. 11–21, apr 2007.

[29] E. F. Schlafly and D. P. Finkbeiner, "Measuring reddening with Sloan Digital Sky Survey stellar spectra and recalibrating SFD," *Astrophysical Journal*, vol. 737, p. 103, aug 2011.

[30] P. Lira *MS Thesis, Universidad de Chile*, 1995.

[31] M. M. Phillips, P. Lira, N. B. Suntzeff, R. A. Schommer, M. Hamuy, and J. Maza, "The Reddening-Free Decline Rate Versus Luminosity Relationship for Type [CLC]Ia[/CLC] Supernovae," *The Astronomical Journal*, vol. 118, pp. 1766–1776, oct 1999.

[32] V. Arsenijevic, S. Fabbro, A. M. Mourão, and A. J. Rica da Silva, "Diversity of supernovae Ia determined using equivalent widths of Si II 4000," *A&A*, vol. 492, pp. 535–544, Dec. 2008.

[33] J. M. Silverman, M. Ganeshalingam, W. Li, and A. V. Filippenko, "Berkeley Supernova Ia Program - III. Spectra near maximum brightness improve the accuracy of derived distances to Type Ia supernovae," *MNRAS*, vol. 425, pp. 1889–1916, Sept. 2012.

[34] N. Chotard, E. Gangler, G. Aldering, P. Antilogus, C. Aragon, S. Bailey, C. Baltay, S. Bongard, C. Buton, A. Canto, M. Childress, Y. Copin, H. K. Fakhouri, E. Y. Hsiao, M. Kerschhaggl, M. Kowalski, S. Loken, P. Nugent, K. Paech, R. Pain, E. Pecontal, R. Pereira, S. Perlmutter, D. Rabinowitz, K. Runge, R. Scalzo, G. Smadja, C. Tao, R. C. Thomas, B. A. Weaver, C. Wu, and Nearby Supernova Factory, "The reddening law of type Ia supernovae: separating intrinsic variability from dust using equivalent widths," *A&A*, vol. 529, p. L4, May 2011.

[35] L. Galbany, M. E. Moreno-Raya, P. Ruiz-Lapuente, J. I. G. Hernández, J. Méndez, P. Vallely, E. Baron, I. Domínguez, M. Hamuy, A. R. López-Sánchez, M. Mollá, S. Catalán, E. A. Cooke, C. Fariña, R. Génova-Santos, R. Karjalainen, H. Lietzen, J. McCormac, F. C. Riddick, J. A. Rubiño-Martín, I. Skillen, V. Tudor, and O. Vaduvescu, "SN 2014J at M82: I. A middle-class type Ia supernova by all spectroscopic metrics," *Monthly Notices of the Royal Astronomical Society*, vol. 457, pp. 525–537, oct 2015.

[36] X. Chen, L. Wang, L. Hu, and P. J. Brown, "Artificial Intelligence Assisted Inversion (AIAI): Quantifying the Spectral Features of ^{56}Ni of Type Ia Supernovae," *arXiv e-prints*, p. arXiv:2210.15892, Oct. 2022.

[37] R. J. Foley and D. Kasen, "MEASURING EJECTA VELOCITY IMPROVES TYPE Ia SUPERNOVA DISTANCES," *The Astrophysical Journal*, vol. 729, p. 55, feb 2011.

[38] S. Blondin, T. Matheson, R. P. Kirshner, K. S. Mandel, P. Berlind, M. Calkins, P. Challis, P. M. Garnavich, S. W. Jha, M. Modjaz, A. G. Riess, and B. P. Schmidt, "The Spectroscopic Diversity of Type Ia Supernovae," *AJ*, vol. 143, p. 126, May 2012.

[39] S. Perlmutter, S. Gabi, G. Goldhaber, A. Goobar, D. E. Groom, I. M. Hook, A. G. Kim, M. Y. Kim, J. C. Lee, R. Pain, C. R. Pennypacker, I. A. Small, R. S. Ellis, R. G. McMahon, B. J. Boyle, P. S. Bunclark, D. Carter, M. J. Irwin, K. Glazebrook, H. J. M. Newberg, A. V. Filippenko, T. Matheson, M. Dopita, and W. J. Couch, "Measurements of the Cosmological Parameters Ω and Λ from the First Seven Supernovae at z >= 0.35," *ApJ*, vol. 483, pp. 565–581, July 1997.

[40] M. Betoule, R. Kessler, J. Guy, J. Mosher, D. Hardin, R. Biswas, P. Astier, P. El-Hage, M. Konig, S. Kuhlmann, J. Marriner, R. Pain, N. Regnault, C. Balland, B. A. Bassett, P. J. Brown, H. Campbell, R. G. Carlberg, F. Cellier-Holzem, D. Cinabro, A. Conley, C. B. D'Andrea, D. L. DePoy, M. Doi, R. S. Ellis, S. Fabbro, A. V. Filippenko, R. J. Foley, J. A. Frieman, D. Fouchez, L. Galbany, A. Goobar, R. R. Gupta, G. J. Hill, R. Hlozek, C. J. Hogan, I. M. Hook, D. A. Howell, S. W. Jha, L. Le Guillou, G. Leloudas, C. Lidman, J. L. Marshall, A. Möller, A. M. Mourão, J. Neveu, R. Nichol, M. D. Olmstead, N. Palanque-Delabrouille, S. Perlmutter, J. L. Prieto, C. J. Pritchet, M. Richmond, A. G. Riess, V. Ruhlmann-Kleider, M. Sako, K. Schahmaneche, D. P. Schneider, M. Smith, J. Sollerman, M. Sullivan, N. A. Walton, and C. J. Wheeler, "Improved cosmological constraints from a joint analysis of the SDSS-II and SNLS supernova samples," *A&A*, vol. 568, p. A22, Aug. 2014.

[41] D. M. Scolnic, D. O. Jones, A. Rest, Y. C. Pan, R. Chornock, R. J. Foley, M. E. Huber, R. Kessler, G. Narayan, A. G. Riess, S. Rodney, E. Berger, D. J. Brout, P. J. Challis, M. Drout, D. Finkbeiner, R. Lunnan, R. P. Kirshner, N. E. Sanders, E. Schlafly,

S. Smartt, C. W. Stubbs, J. Tonry, W. M. Wood-Vasey, M. Foley, J. Hand, E. Johnson, W. S. Burgett, K. C. Chambers, P. W. Draper, K. W. Hodapp, N. Kaiser, R. P. Kudritzki, E. A. Magnier, N. Metcalfe, F. Bresolin, E. Gall, R. Kotak, M. McCrum, and K. W. Smith, "The Complete Light-curve Sample of Spectroscopically Confirmed SNe Ia from Pan-STARRS1 and Cosmological Constraints from the Combined Pantheon Sample," *ApJ*, vol. 859, p. 101, June 2018.

[42] D. Brout, D. Scolnic, B. Popovic, A. G. Riess, A. Carr, J. Zuntz, R. Kessler, T. M. Davis, S. Hinton, D. Jones, W. D. Kenworthy, E. R. Peterson, K. Said, G. Taylor, N. Ali, P. Armstrong, P. Charvu, A. Dwomoh, C. Meldorf, A. Palmese, H. Qu, B. M. Rose, B. Sanchez, C. W. Stubbs, M. Vincenzi, C. M. Wood, P. J. Brown, R. Chen, K. Chambers, D. A. Coulter, M. Dai, G. Dimitriadis, A. V. Filippenko, R. J. Foley, S. W. Jha, L. Kelsey, R. P. Kirshner, A. Möller, J. Muir, S. Nadathur, Y.-C. Pan, A. Rest, C. Rojas-Bravo, M. Sako, M. R. Siebert, M. Smith, B. E. Stahl, and P. Wiseman, "The Pantheon+ Analysis: Cosmological Constraints," *ApJ*, vol. 938, p. 110, Oct. 2022.

[43] S. Bailey, G. Aldering, P. Antilogus, C. Aragon, C. Baltay, S. Bongard, C. Buton, M. Childress, N. Chotard, Y. Copin, E. Gangler, S. Loken, P. Nugent, R. Pain, E. Pecontal, R. Pereira, S. Perlmutter, D. Rabinowitz, G. Rigaudier, K. Runge, R. Scalzo, G. Smadja, H. Swift, C. Tao, R. C. Thomas, C. Wu, and Nearby Supernova Factory, "Using spectral flux ratios to standardize SN Ia luminosities," *A&A*, vol. 500, pp. L17–L20, June 2009.

[44] B. M. Rose, D. Rubin, L. Strolger, and P. M. Garnavich, "Host Galaxy Mass Combined with Local Stellar Age Improve Type Ia Supernovae Distances," dec 2020.

[45] P. F. Léget, M. V. Pruzhinskaya, A. Ciulli, E. Gangler, G. Aldering, P. Antilogus, C. Aragon, S. Bailey, C. Baltay, K. Barbary, S. Bongard, K. Boone, C. Buton, M. Childress, N. Chotard, Y. Copin, S. Dixon, P. Fagrelius, U. Feindt, D. Fouchez, P. Gris,

B. Hayden, W. Hillebrandt, D. A. Howell, A. Kim, M. Kowalski, D. Kuesters, S. Lombardo, Q. Lin, J. Nordin, R. Pain, E. Pecontal, R. Pereira, S. Perlmutter, D. Rabinowitz, M. Rigault, K. Runge, D. Rubin, C. Saunders, L. P. Says, G. Smadja, C. Sofiatti, N. Suzuki, S. Taubenberger, C. Tao, R. C. Thomas, and Nearby Supernova Factory, "Correcting for peculiar velocities of Type Ia supernovae in clusters of galaxies," *A&A*, vol. 615, p. A162, July 2018.

[46] E. R. Peterson, W. D. Kenworthy, D. Scolnic, A. G. Riess, D. Brout, A. Carr, H. Courtois, T. Davis, A. Dwomoh, D. O. Jones, B. Popovic, B. M. Rose, and K. Said, "The Pantheon+ Analysis: Evaluating Peculiar Velocity Corrections in Cosmological Analyses with Nearby Type Ia Supernovae," *ApJ*, vol. 938, p. 112, Oct. 2022.

[47] J. Yang, L. Wang, N. Suntzeff, L. Hu, L. Aldoroty, P. J. Brown, K. Krisciunas, I. Arcavi, J. Burke, L. Galbany, D. Hiramatsu, G. Hosseinzadeh, D. A. Howell, C. McCully, C. Pellegrino, and S. Valenti, "Using 1991t/1999aa-like type ia supernovae as standardizable candles," *The Astrophysical Journal*, vol. 938, p. 83, oct 2022.

[48] M. M. Phillips, C. Ashall, C. R. Burns, C. Contreras, L. Galbany, P. Hoeflich, E. Y. Hsiao, N. Morrell, P. Nugent, S. A. Uddin, E. Baron, W. L. Freedman, C. E. Harris, K. Krisciunas, S. Kumar, J. Lu, S. E. Persson, A. L. Piro, A. Polin, M. Shahbandeh, M. Stritzinger, and N. B. Suntzeff, "The Absolute Magnitudes of 1991T-like Supernovae," *ApJ*, vol. 938, p. 47, Oct. 2022.

[49] L. Wang, G. Goldhaber, G. Aldering, and S. Perlmutter, "Multicolor Light Curves of Type Ia Supernovae on the Color-Magnitude Diagram: A Novel Step toward More Precise Distance and Extinction Estimates," *The Astrophysical Journal*, vol. 590, pp. 944–970, jun 2003.

[50] A. Conley, G. Goldhaber, L. Wang, G. Aldering, R. Amanullah, E. D. Commins, V. Fadeyev, G. Folatelli, G. Garavini, R. Gibbons, A. Goobar, D. E. Groom, I. Hook, D. A. Howell, A. G. Kim, R. A. Knop, M. Kowalski, N. Kuznetsova, C. Lidman, S. No-

bili, P. E. Nugent, R. Pain, S. Perlmutter, E. Smith, A. L. Spadafora, V. Stanishev, M. Strovink, R. C. Thomas, W. M. Wood-Vasey, and T. S. C. Project), "Measurement of Ω _m , Ω _Λ from a Blind Analysis of Type Ia Supernovae with CMAGIC: Using Color Information to Verify the Acceleration of the Universe," *The Astrophysical Journal*, vol. 644, pp. 1–20, jun 2006.

[51] L. Wang, M. Strovink, A. Conley, G. Goldhaber, M. Kowalski, S. Perlmutter, and J. Siegrist, "Nonlinear Decline-Rate Dependence and Intrinsic Variation of Type Ia Supernova Luminosities," *The Astrophysical Journal*, vol. 641, pp. 50–69, apr 2006.

[52] R. Bacon, G. Adam, A. Baranne, G. Courtes, D. Dubet, J. P. Dubois, E. Emsellem, P. Ferruit, Y. Georgelin, G. Monnet, E. Pecontal, A. Rousset, and F. Say, "3D spectrography at high spatial resolution. I. Concept and realization of the integral field spectrograph TIGER.," *A&AS*, vol. 113, p. 347, Oct. 1995.

[53] R. Bacon, Y. Copin, G. Monnet, B. W. Miller, J. R. Allington-Smith, M. Bureau, C. M. Carollo, R. L. Davies, E. Emsellem, H. Kuntschner, R. F. Peletier, E. K. Verolme, and P. T. de Zeeuw, "The SAURON project - I. The panoramic integral-field spectrograph," *MNRAS*, vol. 326, pp. 23–35, Sept. 2001.

[54] R. C. Bohlin, K. D. Gordon, and P. E. Tremblay, "Techniques and Review of Absolute Flux Calibration from the Ultraviolet to the Mid-Infrared," *PASP*, vol. 126, p. 711, Aug. 2014.

[55] G. Aldering, G. Adam, P. Antilogus, P. Astier, R. Bacon, S. Bongard, C. Bonnaud, Y. Copin, D. Hardin, F. Henault, D. A. Howell, J.-P. Lemonnier, J.-M. Levy, S. C. Loken, P. E. Nugent, R. Pain, A. Pecontal, E. Pecontal, S. Perlmutter, R. M. Quimby, K. Schahmaneche, G. Smadja, and W. M. Wood-Vasey, "Overview of the Nearby Supernova Factory," in *Survey and Other Telescope Technologies and Discoveries* (J. A. Tyson and S. Wolff, eds.), vol. 4836 of *Society of Photo-Optical Instrumentation Engineers (SPIE) Conference Series*, pp. 61–72, Dec. 2002.

[56] B. Lantz, G. Aldering, P. Antilogus, C. Bonnaud, L. Capoani, A. Castera, Y. Copin, D. Dubet, E. Gangler, F. Henault, J.-P. Lemonnier, R. Pain, A. Pecontal, E. Pecontal, and G. Smadja, "SNIFS: a wideband integral field spectrograph with microlens arrays," in *Optical Design and Engineering* (L. Mazuray, P. J. Rogers, and R. Wartmann, eds.), vol. 5249, pp. 146–155, International Society for Optics and Photonics, SPIE, 2004.

[57] D. Küsters, S. Lombardo, M. Kowalski, G. Aldering, J. Nordin, and M. Rigault, "Calibrating the SNfactory Integral Field Spectrograph (SNIFS) with SCALA," in *Ground-based and Airborne Instrumentation for Astronomy VI* (C. J. Evans, L. Simard, and H. Takami, eds.), vol. 9908 of *Society of Photo-Optical Instrumentation Engineers (SPIE) Conference Series*, p. 99084V, Aug. 2016.

[58] C. Buton, Y. Copin, G. Aldering, P. Antilogus, C. Aragon, S. Bailey, C. Baltay, S. Bongard, A. Canto, F. Cellier-Holzem, M. Childress, N. Chotard, H. K. Fakhouri, E. Gangler, J. Guy, E. Y. Hsiao, M. Kerschhaggl, M. Kowalski, S. Loken, P. Nugent, K. Paech, R. Pain, E. Pécontal, R. Pereira, S. Perlmutter, D. Rabinowitz, M. Rigault, K. Runge, R. Scalzo, G. Smadja, C. Tao, R. C. Thomas, B. A. Weaver, C. Wu, and Nearby SuperNova Factory, "Atmospheric extinction properties above Mauna Kea from the Nearby SuperNova Factory spectro-photometric data set," *A&A*, vol. 549, p. A8, Jan. 2013.

[59] C. Saunders, G. Aldering, P. Antilogus, S. Bailey, C. Baltay, K. Barbary, D. Baugh, K. Boone, S. Bongard, C. Buton, J. Chen, N. Chotard, Y. Copin, S. Dixon, P. Fagrelius, H. K. Fakhouri, U. Feindt, D. Fouchez, E. Gangler, B. Hayden, W. Hillebrandt, A. G. Kim, M. Kowalski, D. Küsters, P. F. Leget, S. Lombardo, J. Nordin, R. Pain, E. Pecontal, R. Pereira, S. Perlmutter, D. Rabinowitz, M. Rigault, D. Rubin, K. Runge, G. Smadja, C. Sofiatti, N. Suzuki, C. Tao, S. Taubenberger, R. C. Thomas, M. Vincenzi, and T. Nearby Supernova Factory, "SNEMO: Improved Empirical Models for Type Ia Supernovae," *ApJ*, vol. 869, p. 167, Dec. 2018.

[60] G. Aldering, P. Antilogus, C. Aragon, S. Bailey, C. Baltay, S. Bongard, K. Boone, C. Buton, N. Chotard, Y. Copin, S. Dixon, H. K. Fakhouri, U. Feindt, D. Fouchez, E. Gangler, B. Hayden, W. Hillebrandt, A. G. Kim, M. Kowalski, D. Küsters, P. F. Léget, Q. Lin, S. Lombardo, F. Mondon, J. Nordin, R. Pain, E. Pecontal, R. Pereira, S. Perlmutter, K. Ponder, M. Pruzhinskaya, D. Rabinowitz, M. Rigault, D. Rubin, K. Runge, C. Saunders, L. P. Says, G. Smadja, N. Suzuki, C. Tao, S. Taubenberger, R. C. Thomas, M. Vincenzi, B. Weaver, and Nearby Supernova Factory Collaboration, "The SNEMO and SUGAR Companion Data Sets," *Research Notes of the American Astronomical Society*, vol. 4, p. 63, May 2020.

[61] P. F. Léget, E. Gangler, F. Mondon, G. Aldering, P. Antilogus, C. Aragon, S. Bailey, C. Baltay, K. Barbary, S. Bongard, K. Boone, C. Buton, N. Chotard, Y. Copin, S. Dixon, P. Fagrelius, U. Feindt, D. Fouchez, B. Hayden, W. Hillebrandt, A. Kim, M. Kowalski, D. Kuesters, S. Lombardo, Q. Lin, J. Nordin, R. Pain, E. Pecontal, R. Pereira, S. Perlmutter, K. A. Ponder, M. V. Pruzhinskaya, D. Rabinowitz, M. Rigault, K. Runge, D. Rubin, C. Saunders, L. P. Says, G. Smadja, C. Sofiatti, N. Suzuki, S. Taubenberger, C. Tao, and R. C. Thomas, "SUGAR: An improved empirical model of Type Ia supernovae based on spectral features," *A&A*, vol. 636, p. A46, Apr. 2020.

[62] H. K. Fakhouri, K. Boone, G. Aldering, P. Antilogus, C. Aragon, S. Bailey, C. Baltay, K. Barbary, D. Baugh, S. Bongard, C. Buton, J. Chen, M. Childress, N. Chotard, Y. Copin, P. Fagrelius, U. Feindt, M. Fleury, D. Fouchez, E. Gangler, B. Hayden, A. G. Kim, M. Kowalski, P. F. Leget, S. Lombardo, J. Nordin, R. Pain, E. Pecontal, R. Pereira, S. Perlmutter, D. Rabinowitz, J. Ren, M. Rigault, D. Rubin, K. Runge, C. Saunders, R. Scalzo, G. Smadja, C. Sofiatti, M. Strovink, N. Suzuki, C. Tao, R. C. Thomas, B. A. Weaver, and T. Nearby Supernova Factory, "Improving Cosmological Distance Measurements Using Twin Type Ia Supernovae," *ApJ*, vol. 815, p. 58, Dec. 2015.

[63] K. Boone, G. Aldering, P. Antilogus, C. Aragon, S. Bailey, C. Baltay, S. Bongard, C. Buton, Y. Copin, S. Dixon, D. Fouchez, E. Gangler, R. Gupta, B. Hayden, W. Hillebrandt, A. G. Kim, M. Kowalski, D. Küsters, P. F. Léget, F. Mondon, J. Nordin, R. Pain, E. Pecontal, R. Pereira, S. Perlmutter, K. A. Ponder, D. Rabinowitz, M. Rigault, D. Rubin, K. Runge, C. Saunders, G. Smadja, N. Suzuki, C. Tao, S. Taubenberger, R. C. Thomas, and M. Vincenzi, "The Twins Embedding of Type Ia Supernovae. I. The Diversity of Spectra at Maximum Light," *ApJ*, vol. 912, p. 70, May 2021.

[64] G. Stein, U. Seljak, V. Böhm, G. Aldering, P. Antilogus, C. Aragon, S. Bailey, C. Baltay, S. Bongard, K. Boone, C. Buton, Y. Copin, S. Dixon, D. Fouchez, E. Gangler, R. Gupta, B. Hayden, W. Hillebrandt, M. Karmen, A. G. Kim, M. Kowalski, D. Küsters, P. F. Léget, F. Mondon, J. Nordin, R. Pain, E. Pecontal, R. Pereira, S. Perlmutter, K. A. Ponder, D. Rabinowitz, M. Rigault, D. Rubin, K. Runge, C. Saunders, G. Smadja, N. Suzuki, C. Tao, S. Taubenberger, R. C. Thomas, M. Vincenzi, and Nearby Supernova Factory, "A Probabilistic Autoencoder for Type Ia Supernova Spectral Time Series," *ApJ*, vol. 935, p. 5, Aug. 2022.

[65] K. Boone, G. Aldering, P. Antilogus, C. Aragon, S. Bailey, C. Baltay, S. Bongard, C. Buton, Y. Copin, S. Dixon, D. Fouchez, E. Gangler, R. Gupta, B. Hayden, W. Hillebrandt, A. G. Kim, M. Kowalski, D. Küsters, P. F. Léget, F. Mondon, J. Nordin, R. Pain, E. Pecontal, R. Pereira, S. Perlmutter, K. A. Ponder, D. Rabinowitz, M. Rigault, D. Rubin, K. Runge, C. Saunders, G. Smadja, N. Suzuki, C. Tao, S. Taubenberger, R. C. Thomas, and M. Vincenzi, "The Twins Embedding of Type Ia Supernovae. II. Improving Cosmological Distance Estimates," *ApJ*, vol. 912, p. 71, May 2021.

[66] P. E. Nugent, M. Sullivan, S. B. Cenko, R. C. Thomas, D. Kasen, D. A. Howell, D. Bersier, J. S. Bloom, S. R. Kulkarni, M. T. Kandrashoff, A. V. Filippenko, J. M. Silverman, G. W. Marcy, A. W. Howard, H. T. Isaacson, K. Maguire, N. Suzuki, J. E.

Tarlton, Y.-C. Pan, L. Bildsten, B. J. Fulton, J. T. Parrent, D. Sand, P. Podsiadlowski, F. B. Bianco, B. Dilday, M. L. Graham, J. Lyman, P. James, M. M. Kasliwal, N. M. Law, R. M. Quimby, I. M. Hook, E. S. Walker, P. Mazzali, E. Pian, E. O. Ofek, A. Gal-Yam, and D. Poznanski, "Supernova SN 2011fe from an exploding carbon-oxygen white dwarf star," *Nature*, vol. 480, pp. 344–347, Dec. 2011.

[67] F. K. Röpke, M. Kromer, I. R. Seitenzahl, R. Pakmor, S. A. Sim, S. Taubenberger, F. Ciaraldi-Schoolmann, W. Hillebrandt, G. Aldering, P. Antilogus, C. Baltay, S. Benitez-Herrera, S. Bongard, C. Buton, A. Canto, F. Cellier-Holzem, M. Childress, N. Chotard, Y. Copin, H. K. Fakhouri, M. Fink, D. Fouchez, E. Gangler, J. Guy, S. Hachinger, E. Y. Hsiao, J. Chen, M. Kerschhaggl, M. Kowalski, P. Nugent, K. Paech, R. Pain, E. Pecontal, R. Pereira, S. Perlmutter, D. Rabinowitz, M. Rigault, K. Runge, C. Saunders, G. Smadja, N. Suzuki, C. Tao, R. C. Thomas, A. Tilquin, and C. Wu, "Constraining Type Ia Supernova Models: SN 2011fe as a Test Case," *ApJ*, vol. 750, p. L19, May 2012.

[68] R. Pereira, R. C. Thomas, G. Aldering, P. Antilogus, C. Baltay, S. Benitez-Herrera, S. Bongard, C. Buton, A. Canto, F. Cellier-Holzem, J. Chen, M. Childress, N. Chotard, Y. Copin, H. K. Fakhouri, M. Fink, D. Fouchez, E. Gangler, J. Guy, W. Hillebrandt, E. Y. Hsiao, M. Kerschhaggl, M. Kowalski, M. Kromer, J. Nordin, P. Nugent, K. Paech, R. Pain, E. Pécontal, S. Perlmutter, D. Rabinowitz, M. Rigault, K. Runge, C. Saunders, G. Smadja, C. Tao, S. Taubenberger, A. Tilquin, and C. Wu, "Spectrophotometric time series of SN 2011fe from the Nearby Supernova Factory," *A&A*, vol. 554, p. A27, June 2013.

[69] G. Aldering, P. Antilogus, S. Bailey, C. Baltay, A. Bauer, N. Blanc, S. Bongard, Y. Copin, E. Gangler, S. Gilles, R. Kessler, D. Kocevski, B. C. Lee, S. Loken, P. Nugent, R. Pain, E. Pécontal, R. Pereira, S. Perlmutter, D. Rabinowitz, G. Rigaudier, R. Scalzo, G. Smadja, R. C. Thomas, L. Wang, B. A. Weaver, and Nearby Supernova Factory,

"Nearby Supernova Factory Observations of SN 2005gj: Another Type Ia Supernova in a Massive Circumstellar Envelope," *ApJ*, vol. 650, pp. 510–527, Oct. 2006.

[70] R. C. Thomas, G. Aldering, P. Antilogus, C. Aragon, S. Bailey, C. Baltay, E. Baron, A. Bauer, C. Buton, S. Bongard, Y. Copin, E. Gangler, S. Gilles, R. Kessler, S. Loken, P. Nugent, R. Pain, J. Parrent, E. Pécontal, R. Pereira, S. Perlmutter, D. Rabinowitz, G. Rigaudier, K. Runge, R. Scalzo, G. Smadja, L. Wang, B. A. Weaver, and Nearby Supernova Factory, "Nearby Supernova Factory Observations of SN 2006D: On Sporadic Carbon Signatures in Early Type Ia Supernova Spectra," *ApJ*, vol. 654, pp. L53–L56, Jan. 2007.

[71] R. A. Scalzo, G. Aldering, P. Antilogus, C. Aragon, S. Bailey, C. Baltay, S. Bongard, C. Buton, M. Childress, N. Chotard, Y. Copin, H. K. Fakhouri, A. Gal-Yam, E. Gangler, S. Hoyer, M. Kasliwal, S. Loken, P. Nugent, R. Pain, E. Pécontal, R. Pereira, S. Perlmutter, D. Rabinowitz, A. Rau, G. Rigaudier, K. Runge, G. Smadja, C. Tao, R. C. Thomas, B. Weaver, and C. Wu, "Nearby Supernova Factory Observations of SN 2007if: First Total Mass Measurement of a Super-Chandrasekhar-Mass Progenitor," *ApJ*, vol. 713, pp. 1073–1094, Apr. 2010.

[72] L. Zhou, J. Z. Huang, and R. J. Carroll, "Joint modelling of paired sparse functional data using principal components," *Biometrika*, vol. 95, pp. 601–619, 09 2008.

[73] G. James, T. Hastie, and C. Sugar, "Principal component models for sparse functional data," *Biometrika*, vol. 87, pp. 587–602, 09 2000.

[74] L. Aldoroty, J. Yang, and S. He, "snlcpy," Apr. 2022.

[75] M. Childress, G. Aldering, P. Antilogus, C. Aragon, S. Bailey, C. Baltay, S. Bongard, C. Buton, A. Canto, F. Cellier-Holzem, N. Chotard, Y. Copin, H. K. Fakhouri, E. Gangler, J. Guy, E. Y. Hsiao, M. Kerschhaggl, A. G. Kim, M. Kowalski, S. Loken, P. Nugent, K. Paech, R. Pain, E. Pecontal, R. Pereira, S. Perlmutter, D. Rabinowitz, M. Rigault, K. Runge, R. Scalzo, G. Smadja, C. Tao, R. C. Thomas, B. A. Weaver,

and C. Wu, "Host Galaxy Properties and Hubble Residuals of Type Ia Supernovae from the Nearby Supernova Factory," *ApJ*, vol. 770, p. 108, June 2013.

[76] K. Barbary, S. Bailey, G. Barentsen, T. Barclay, R. Biswas, K. Boone, M. Craig, U. Feindt, B. Friesen, D. Goldstein, S. W. Jha, D. O. Jones, F. Mondon, S. Papadogiannakis, D. Perrefort, J. Pierel, S. Rodney, B. Rose, C. Saunders, B. Sipőcz, C. Sofiatti, R. C. Thomas, J. van Santen, M. Vincenzi, D. Wang, and M. Wood-Vasey, "Sncosmo," Mar. 2022. If you use SNCosmo, please cite it using these metadata.

[77] J. J. Moré, "The Levenberg-Marquardt algorithm: Implementation and theory," in *Numerical Analysis* (G. A. Watson, ed.), (Berlin, Heidelberg), pp. 105–116, Springer Berlin Heidelberg, 1978.

[78] J. J. Moré and S. J. Wright, *Optimization Software Guide*. Society for Industrial and Applied Mathematics, 1993.

[79] C. B. Markwardt, "Non-linear Least-squares Fitting in IDL with MPFIT," in *Astronomical Data Analysis Software and Systems XVIII* (D. A. Bohlender, D. Durand, and P. Dowler, eds.), vol. 411 of *Astronomical Society of the Pacific Conference Series*, p. 251, Sept. 2009.

[80] R. Scalzo, G. Aldering, P. Antilogus, C. Aragon, S. Bailey, C. Baltay, S. Bongard, C. Buton, F. Cellier-Holzem, M. Childress, N. Chotard, Y. Copin, H. K. Fakhouri, E. Gangler, J. Guy, A. G. Kim, M. Kowalski, M. Kromer, J. Nordin, P. Nugent, K. Paech, R. Pain, E. Pecontal, R. Pereira, S. Perlmutter, D. Rabinowitz, M. Rigault, K. Runge, C. Saunders, S. A. Sim, G. Smadja, C. Tao, S. Taubenberger, R. C. Thomas, B. A. Weaver, and Nearby Supernova Factory, "Type Ia supernova bolometric light curves and ejected mass estimates from the Nearby Supernova Factory," *MNRAS*, vol. 440, pp. 1498–1518, May 2014.

[81] R. Scalzo, G. Aldering, P. Antilogus, C. Aragon, S. Bailey, C. Baltay, S. Bongard, C. Buton, A. Canto, F. Cellier-Holzem, M. Childress, N. Chotard, Y. Copin, H. K.

Fakhouri, E. Gangler, J. Guy, E. Y. Hsiao, M. Kerschhaggl, M. Kowalski, P. Nugent, K. Paech, R. Pain, E. Pecontal, R. Pereira, S. Perlmutter, D. Rabinowitz, M. Rigault, K. Runge, G. Smadja, C. Tao, R. C. Thomas, B. A. Weaver, C. Wu, and T. Nearby Supernova Factory, "A Search for New Candidate Super-Chandrasekhar-mass Type Ia Supernovae in the Nearby Supernova Factory Data Set," *ApJ*, vol. 757, p. 12, Sept. 2012.

[82] E. S. Walker, C. Baltay, A. Campillay, C. Citrenbaum, C. Contreras, N. Ellman, U. Feindt, C. González, M. L. Graham, E. Hadjiyska, E. Y. Hsiao, K. Krisciunas, R. McKinnon, K. Ment, N. Morrell, P. Nugent, M. M. Phillips, D. Rabinowitz, S. Rostami, J. Serón, M. Stritzinger, M. Sullivan, and B. E. Tucker, "First results from the la silla-quest supernova survey and the carnegie supernova project," *The Astrophysical Journal Supplement Series*, vol. 219, p. 13, jul 2015.

[83] L. Hu, X. Chen, and L. Wang, "Spectroscopic Studies of Type Ia Supernovae Using LSTM Neural Networks," *arXiv e-prints*, p. arXiv:2202.02498, Feb. 2022.

[84] Y.-C. Pan, "High-velocity Type Ia Supernova Has a Unique Host Environment," *ApJ*, vol. 895, p. L5, May 2020.

[85] J. M. Silverman, J. Vinkó, G. H. Marion, J. C. Wheeler, B. Barna, T. Szalai, B. W. Mulligan, and A. V. Filippenko, "High-velocity features of calcium and silicon in the spectra of Type Ia supernovae," *MNRAS*, vol. 451, pp. 1973–2014, Aug. 2015.

[86] M. R. Siebert, R. J. Foley, D. O. Jones, and K. W. Davis, "A possible distance bias for type Ia supernovae with different ejecta velocities," *MNRAS*, vol. 493, pp. 5713–5725, Apr. 2020.

[87] D. Foreman-Mackey, D. W. Hogg, D. Lang, and J. Goodman, "emcee: The MCMC Hammer," *PASP*, vol. 125, p. 306, Mar. 2013.

[88] S. Hachinger, P. A. Mazzali, M. Sullivan, R. S. Ellis, K. Maguire, A. Gal-Yam, D. A. Howell, P. E. Nugent, E. Baron, J. Cooke, I. Arcavi, D. Bersier, B. Dilday, P. A.

James, M. M. Kasliwal, S. R. Kulkarni, E. O. Ofek, R. R. Laher, J. Parrent, J. Surace, O. Yaron, and E. S. Walker, "The UV/optical spectra of the Type Ia supernova SN 2010jn: a bright supernova with outer layers rich in iron-group elements," *MNRAS*, vol. 429, pp. 2228–2248, Mar. 2013.

[89] K. Maguire, M. Sullivan, R. C. Thomas, P. E. Nugent, D. A. Howell, A. Gal-Yam, I. Arcavi, S. Ben-Ami, S. Blake, J. Botyanszki, C. Buton, J. Cooke, R. S. Ellis, I. M. Hook, M. M. Kasliwal, Y.-C. Pan, R. Pereira, P. Podsiadlowski, A. Sternberg, N. Suzuki, D. Xu, O. Yaron, J. S. Bloom, S. B. Cenko, S. R. Kulkarni, N. Law, E. O. Ofek, D. Poznanski, and R. M. Quimby, "PTF10ops - a subluminous, normal-width lightcurve Type Ia supernova in the middle of nowhere," *MNRAS*, vol. 418, pp. 747–758, aug 2011.

[90] A. M. Khokhlov, "The structure of detonation waves in supernovae," *MNRAS*, vol. 239, pp. 785–808, Aug. 1989.

[91] P. Hoeflich, "Accelerated Lambda Iteration in Rapidly Expanding Envelopes," *arXiv e-prints*, pp. astro–ph/0207103, July 2002.

[92] V. N. Gamezo, A. M. Khokhlov, E. S. Oran, A. Y. Chtchelkanova, and R. O. Rosenberg, "Thermonuclear Supernovae: Simulations of the Deflagration Stage and Their Implications," *Science*, vol. 299, pp. 77–81, Jan. 2003.

[93] F. K. Röpke, W. Hillebrandt, W. Schmidt, J. C. Niemeyer, S. I. Blinnikov, and P. A. Mazzali, "A Three-Dimensional Deflagration Model for Type Ia Supernovae Compared with Observations," *ApJ*, vol. 668, pp. 1132–1139, Oct. 2007.

[94] P. Höflich, C. L. Gerardy, R. A. Fesen, and S. Sakai, "Infrared Spectra of the Subluminous Type Ia Supernova SN 1999by," *ApJ*, vol. 568, pp. 791–806, Apr. 2002.

[95] L. Wang and J. C. Wheeler, "Spectropolarimetry of supernovae," *Annual Review of Astronomy and Astrophysics*, vol. 46, no. 1, pp. 433–474, 2008.

[96] L. Wang, D. Baade, and F. Patat, "Spectropolarimetric diagnostics of thermonuclear supernova explosions," *Science*, vol. 315, no. 5809, pp. 212–214, 2007.

[97] K. Maeda, S. Benetti, M. Stritzinger, F. K. Röpke, G. Folatelli, J. Sollerman, S. Taubenberger, K. Nomoto, G. Leloudas, M. Hamuy, M. Tanaka, P. A. Mazzali, and N. Elias-Rosa, "An asymmetric explosion as the origin of spectral evolution diversity in type Ia supernovae," *Nature*, vol. 466, pp. 82–85, July 2010.

[98] J. R. Maund, P. Höflich, F. Patat, J. C. Wheeler, P. Zelaya, D. Baade, L. Wang, A. Clocchiatti, and J. Quinn, "The Unification of Asymmetry Signatures of Type Ia Supernovae," *ApJ*, vol. 725, pp. L167–L171, Dec. 2010.

[99] A. V. Filippenko, M. W. Richmond, T. Matheson, J. C. Shields, E. M. Burbidge, R. D. Cohen, M. Dickinson, M. A. Malkan, B. Nelson, J. Pietz, D. Schlegel, P. Schmeer, H. Spinrad, C. C. Steidel, H. D. Tran, and W. Wren, "The Peculiar Type IA SN 1991T: Detonation of a White Dwarf?," *ApJ*, vol. 384, p. L15, Jan. 1992.

[100] A. V. Filippenko, M. W. Richmond, D. Branch, M. Gaskell, W. Herbst, C. H. Ford, R. R. Treffers, T. Matheson, L. C. Ho, A. Dey, W. L. W. Sargent, T. A. Small, and W. J. M. van Breugel, "The Subluminous, Spectroscopically Peculiar Type 1a Supernova 1991bg in the Elliptical Galaxy NGC 4374," *AJ*, vol. 104, p. 1543, Oct. 1992.

[101] D. Branch, M. A. Troxel, D. J. Jeffery, K. Hatano, M. Musco, J. Parrent, E. Baron, L. C. Dang, D. Casebeer, N. Hall, and W. Ketchum, "Comparative Direct Analysis of Type Ia Supernova Spectra. III. Premaximum," *PASP*, vol. 119, pp. 709–721, July 2007.

[102] J. M. Silverman and A. V. Filippenko, "Berkeley Supernova Ia Program - IV. Carbon detection in early-time optical spectra of Type Ia supernovae," *MNRAS*, vol. 425, pp. 1917–1933, Sept. 2012.

[103] J. Goodman and J. Weare, "Ensemble samplers with affine invariance," *Communications in Applied Mathematics and Computational Science*, vol. 5, pp. 65–80, Jan. 2010.

APPENDIX A

PHOTOMETRIC FILTERS

λ_B	$R_B(\lambda)$	λ_V	$R_V(\lambda)$	λ_R	$R_R(\lambda)$	λ_I	$R_I(\lambda)$
3600	0.0	4700	0.0	5500	0.0	7000	0.0
3700	0.031	4800	0.033	5600	0.247	7100	0.09
3800	0.137	4900	0.176	5700	0.78	7200	0.356
3900	0.584	5000	0.485	5800	0.942	7300	0.658
4000	0.947	5100	0.811	5900	0.998	7400	0.865
4100	1.0	5200	0.986	6000	1.0	7500	0.96
4200	1.0	5300	1.0	6100	0.974	7600	1.0
4300	0.957	5400	0.955	6200	0.94	7700	0.998
4400	0.895	5500	0.865	6300	0.901	7800	0.985
4500	0.802	5600	0.75	6400	0.859	7900	0.973
4600	0.682	5700	0.656	6500	0.814	8000	0.97
4700	0.577	5800	0.545	6600	0.76	8100	0.958
4800	0.474	5900	0.434	6700	0.713	8200	0.932
4900	0.369	6000	0.334	6800	0.662	8300	0.904
5000	0.278	6100	0.249	6900	0.605	8400	0.86
5100	0.198	6200	0.18	7000	0.551	8500	0.81
5200	0.125	6300	0.124	7100	0.497	8600	0.734
5300	0.078	6400	0.075	7200	0.446	8700	0.59
5400	0.036	6500	0.041	7300	0.399	8800	0.392
5500	0.008	6600	0.022	7400	0.35	8900	0.203
5600	0.0	6700	0.014	7500	0.301	9000	0.07

		6800	0.011	7600	0.257	9100	0.008
		6900	0.008	7700	0.215	9200	0.0
		7000	0.006	7800	0.177		
		7100	0.004	7900	0.144		
		7200	0.002	8000	0.116		
		7300	0.001	8100	0.089		
		7400	0.0	8200	0.066		
				8300	0.051		
				8400	0.039		
				8500	0.03		
				8600	0.021		
				8700	0.014		
				8800	0.008		
				8900	0.006		
				9000	0.003		
				9100	0.0		

Table A.1: Photometric filters used in this analysis. λ_X columns indicate wavelength, and $R_X(\lambda)$ columns indicate the transmission function in photon fractions [14].

APPENDIX B

STATISTICS

B.1 Error propagation

The most straightforward way to propagate error for a function $f(x_0, x_1, ..., x_n)$ is:

$$\sigma_f = \sqrt{\sum_{i=0}^{n} \left(\frac{\partial f}{\partial x_i}\sigma_{x_i}\right)^2}, \tag{B.1}$$

where σ_{x_i} is the error for variable x_i. Note that this formula *assumes the variables are all independent*. If variables cannot be assumed to be independent, then the error propagation formula for $f(x_0, x_1, ..., x_n)$ is

$$\sigma_f^2 = \mathbf{JCJ^T}, \tag{B.2}$$

where $\mathbf{J}$ is the Jacobian matrix of $f(x_0, x_1, ..., x_n)$ and $\mathbf{C}$ is the covariance matrix of the variables x_i. Equation B.1 represents this matrix formula if all off-diagonal entries of $\mathbf{C}$ are 0.

B.2 Least squares fitting

In general, when minimizing χ^2 to fit a model,

$$\chi^2 = \sum_{i=0}^{k} \left(\frac{X_i - \mu_i}{\sigma_i}\right)^2 \tag{B.3}$$

where X_i is the data, μ_i is the model, and σ_i is the error for the data. k is the number of data points. The fit can be weighted by error in all axes. As an example, if we have a linear model that we want to fit to our data,

$$y(x) = mx + b, \tag{B.4}$$

then the χ^2 to be minimized is

$$\chi^2 = \sum_{i=0}^{k} \frac{(X_i - (mx_i + b))^2}{\sigma_i}. \tag{B.5}$$

To determine the appropriate weights, follow the procedure in Appendix B.1, taking derivatives with respect to each data measurement. Then,

$$\chi^2 = \sum_{i=0}^{k} \frac{(X_i - (mx_i + b))^2}{\sigma_y^2 + m^2\sigma_x^2}. \tag{B.6}$$

B.3 Maximum likelihood estimation

Maximum likelihood estimation (MLE) is a method of estimating parameters of a prior probability distribution and data by maximizing a likelihood function. The likelihood function is representative of the probability of the data occurring, given the parameters of the function (i.e., $\mathcal{L}(\theta|x_i)$, where θ are the fit parameters and x_i are realizations of the random variables associated with the data). It is related to the probability density by:

$$\mathcal{L}(\theta|x_i) = \prod_i f(x_i|\theta). \tag{B.7}$$

The final parameter estimates $\hat{\theta}$ are set such that

$$\hat{\theta} = \text{argmax}\mathcal{L}(\theta|x_i). \tag{B.8}$$

However, it is often difficult to work with functions in this form, so the function that is maximized is almost always the log likelihood:

$$\log \mathcal{L}(\theta|x_i) = \log\left(\prod_i f(x_i|\theta)\right) = \sum_i f(x_i|\theta). \tag{B.9}$$

In this work, the probability distribution is assumed to be Gaussian, such that $\theta = (\mu, \sigma)$

and has a density function:

$$f(x;\mu,\sigma) = \frac{1}{\sqrt{2\pi\sigma^2}} \exp\Big(-\frac{1}{2}\Big(\frac{x-\mu}{\sigma}\Big)^2\Big). \tag{B.10}$$

Then, the log likelihood to be maximized is

$$\log \mathcal{L}(\theta|x_i) = -\frac{1}{2}\Big(\sum_i \frac{(y_i - Y)^2}{\bar{\sigma_i^2}} + \log(2\pi\bar{\sigma_i^2})\Big) \tag{B.11}$$

where y_i are the data, Y is the model, and $\bar{\sigma^2} = \sigma_i^2 + f^2Y^2$. σ_i^2 is the variance of the data, and the "extra" f term is included because we assume the variance has been underestimated. If the log likelihood of Equation B.10 is taken using $\bar{\sigma^2} = \sigma_i^2 + f^2Y^2$ as the variance the entire time, then f becomes $e^{2\log f}$, but this does not matter because both are constants.

B.4 Markov chain Monte Carlo

Monte Carlo methods are a class of computational algorithms that rely on random draws from a reasonable domain to initialize the algorithm, does some computation on those draws, and aggregates the results.

Markov chain Monte Carlo (MCMC) [103] methods are a type of Monte Carlo experiment that constructs a Markov chain as a part of the computation on the random draws. This means that each ith draw depends on on the state of the previous $i-1$th draw. Samples are drawn from a probability distribution, and over many iterations, an algorithm "walks" toward increasingly more probable draws. In its simplest form, the walk does this by calculating the probability of the draw, comparing that probability to another value, and then either accepting or rejecting the draw depending on if the probability is higher or lower than the comparison value. If the step is rejected, the walk repeats that draw until it accepts a new position.

MCMC methods can be combined with maximum likelihood functions (MLE, Section B.3). In the case of this work, "proposal" values (fit parameters) are drawn from a uniform dis-

tribution, and these values are input into a maximum likelihood function associated with a distance modulus model.

APPENDIX C

HUBBLE RESIDUAL MCMC DIAGNOSTIC PLOTS

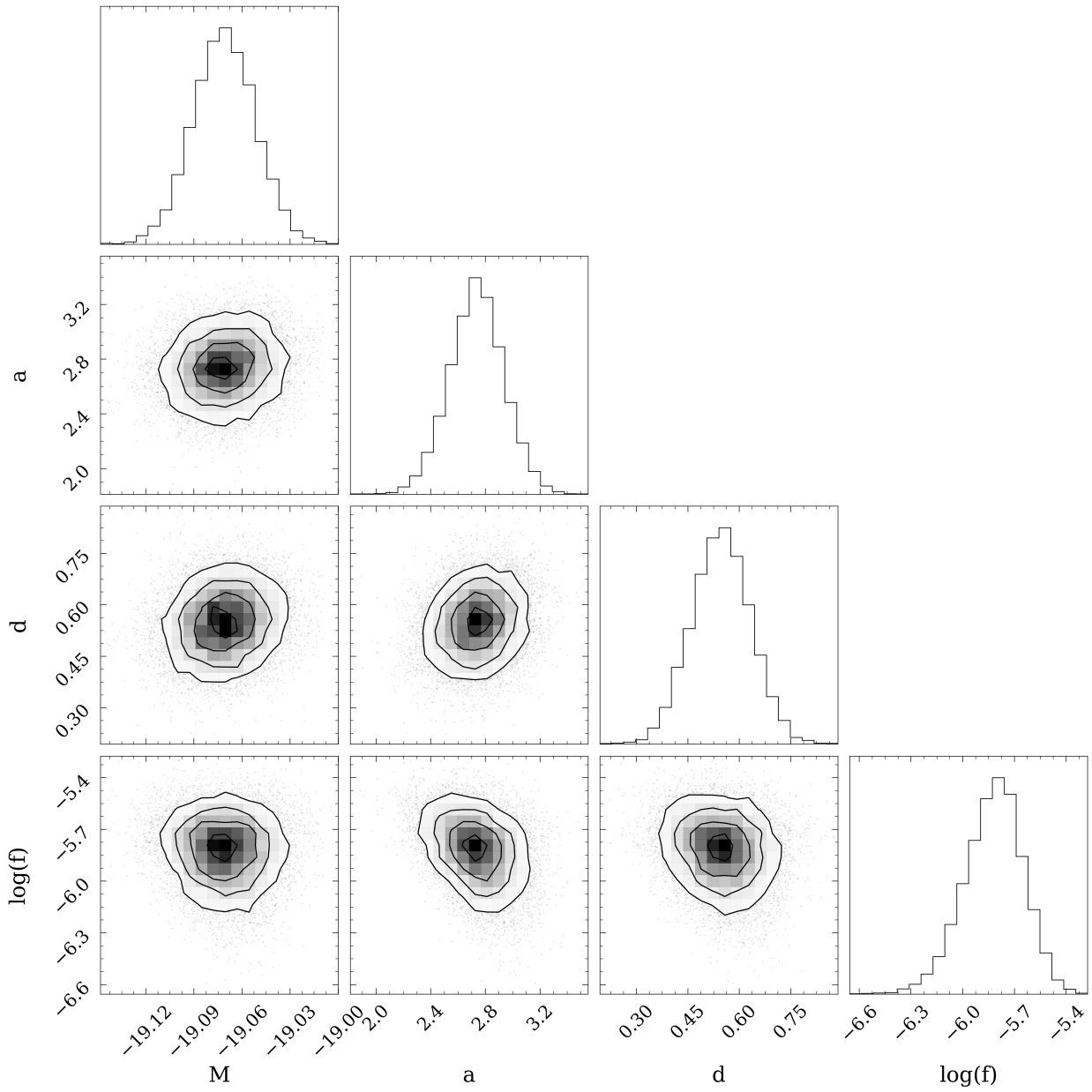

Figure C.1: Corner plot showing correlation between parameters for the MCMC trials for the Tripp distance modulus model (Figure 4.19,[12, 13]), where all SNe have been standardized together. Burn-in has been removed.

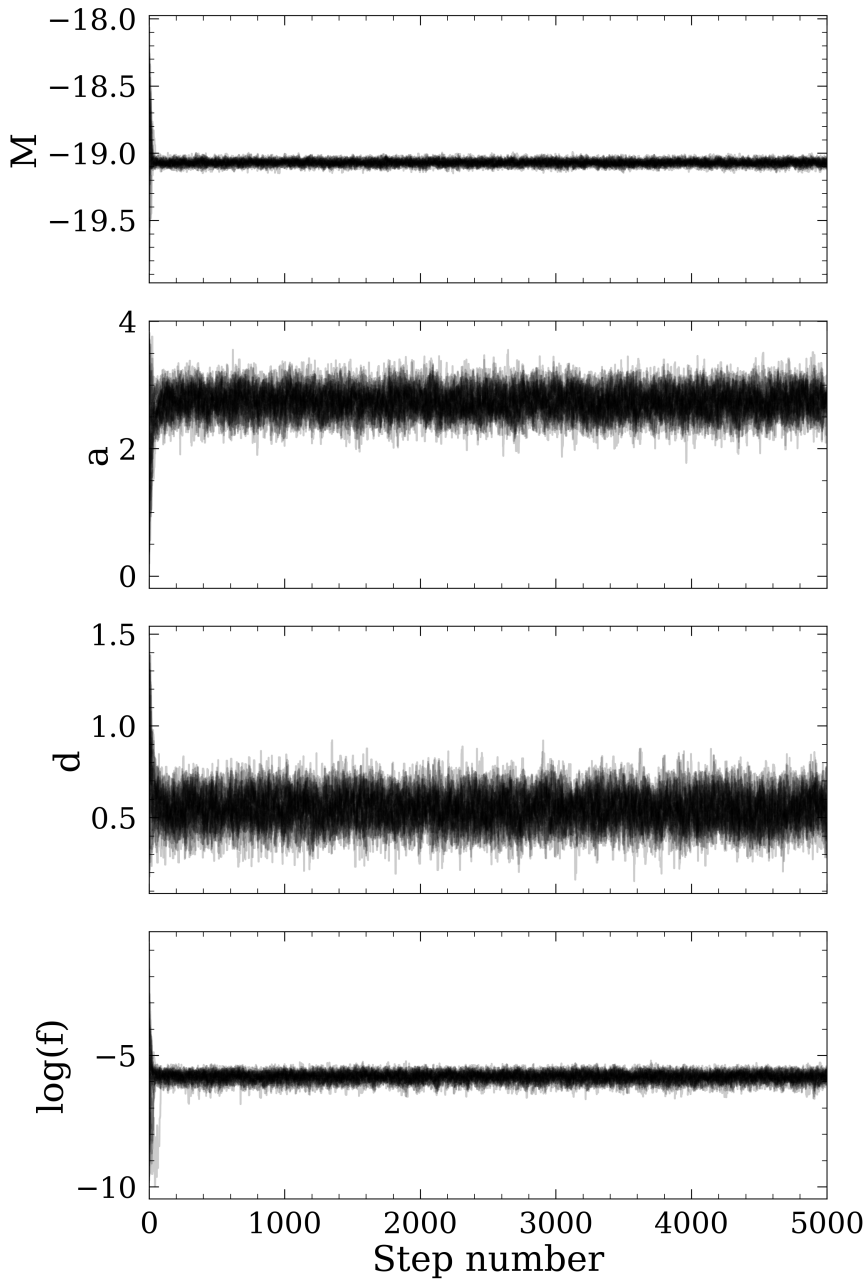

Figure C.2: Parameter as a function of step number for the MCMC trials for the Tripp [12, 13] distance modulus model, where all SNe have been standardized together. Burn-in is not removed.

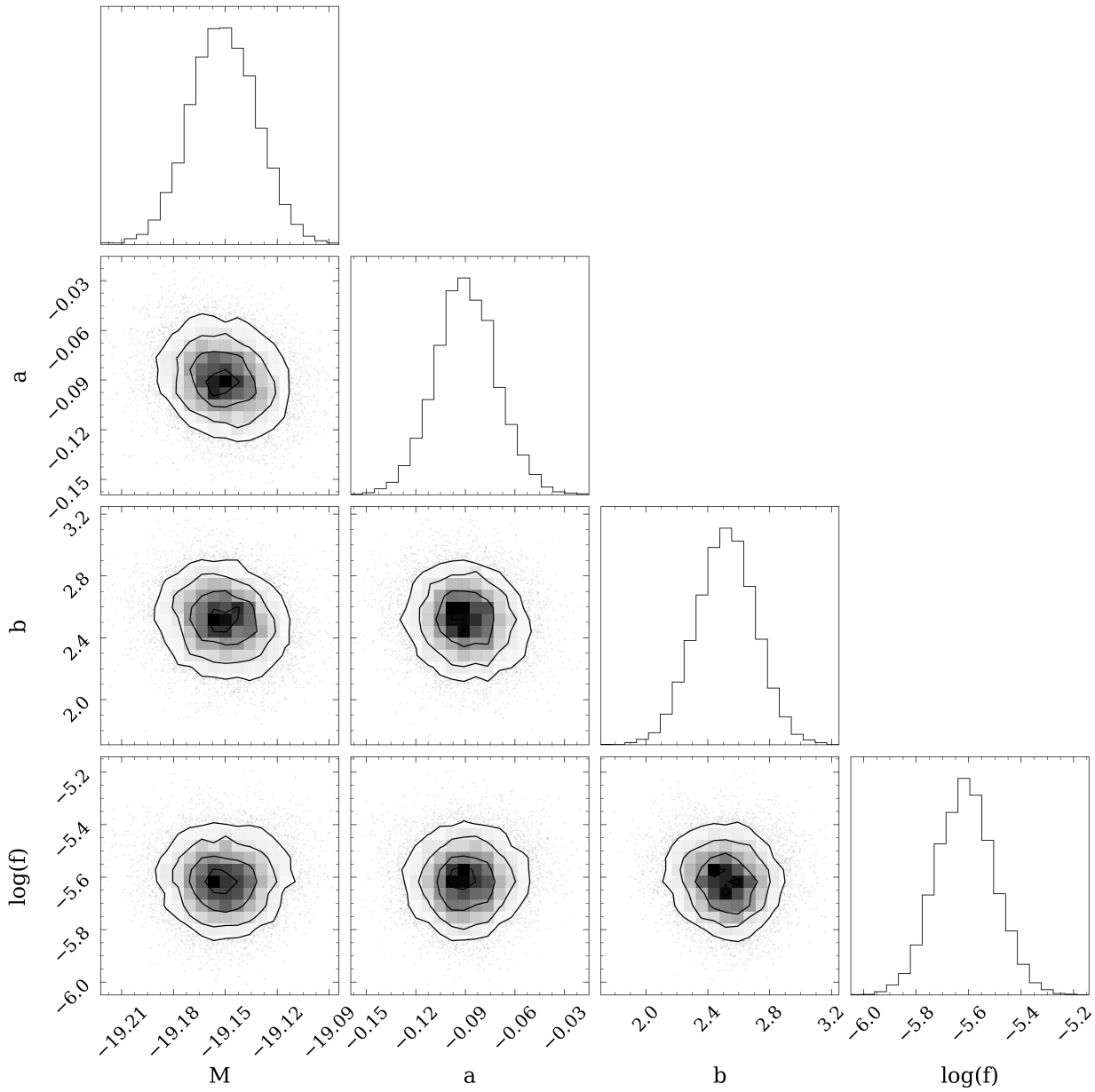

Figure C.3: The same as Figure C.1, but for the SALT3 [3] distance modulus model (Equation 3.29.

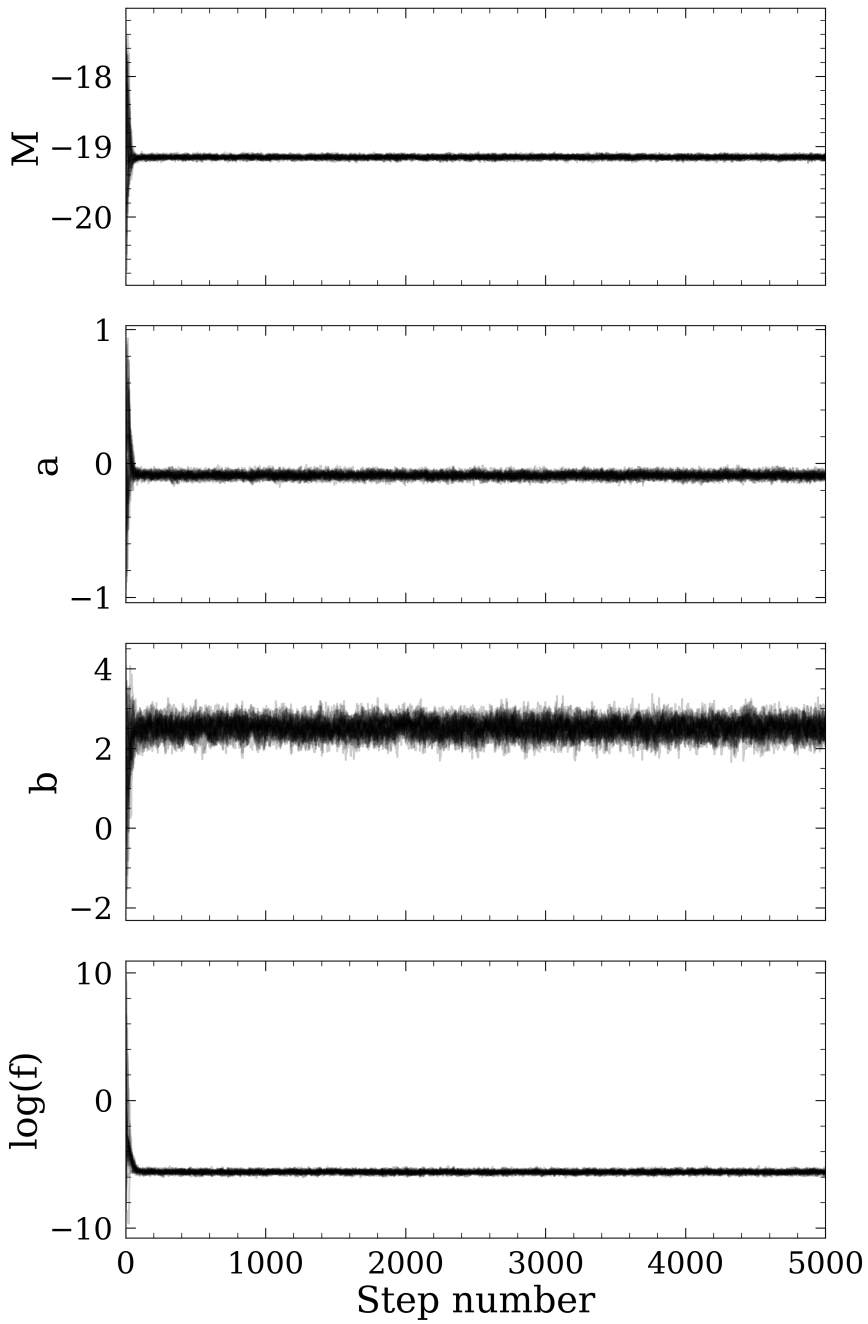

Figure C.4: The same as Figure C.2, but for the SALT3 [3] distance modulus model (Equation 3.29).

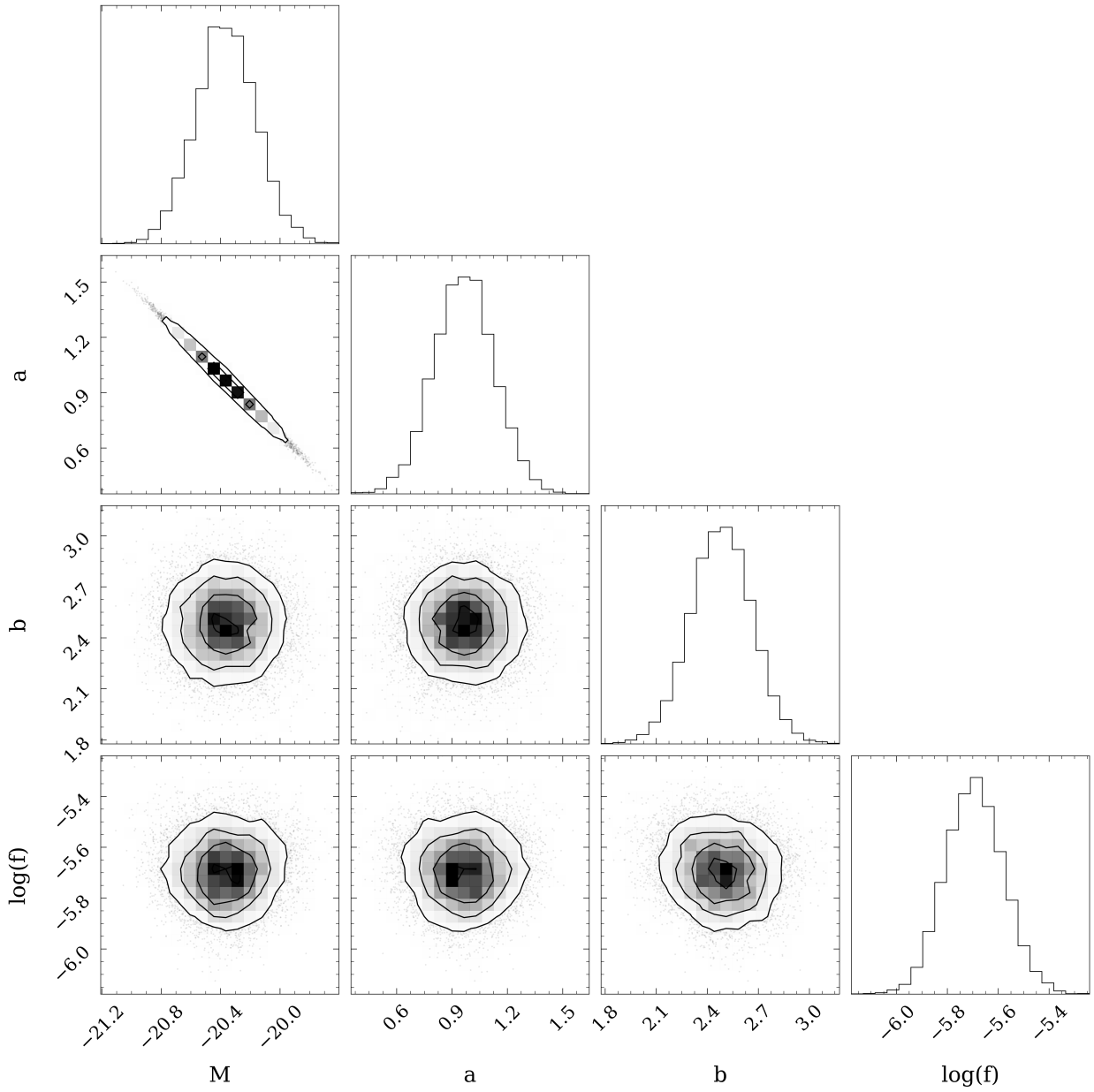

Figure C.5: The same as Figure C.1, but for the F R(Ni II) distance modulus model (Equation 3.30.

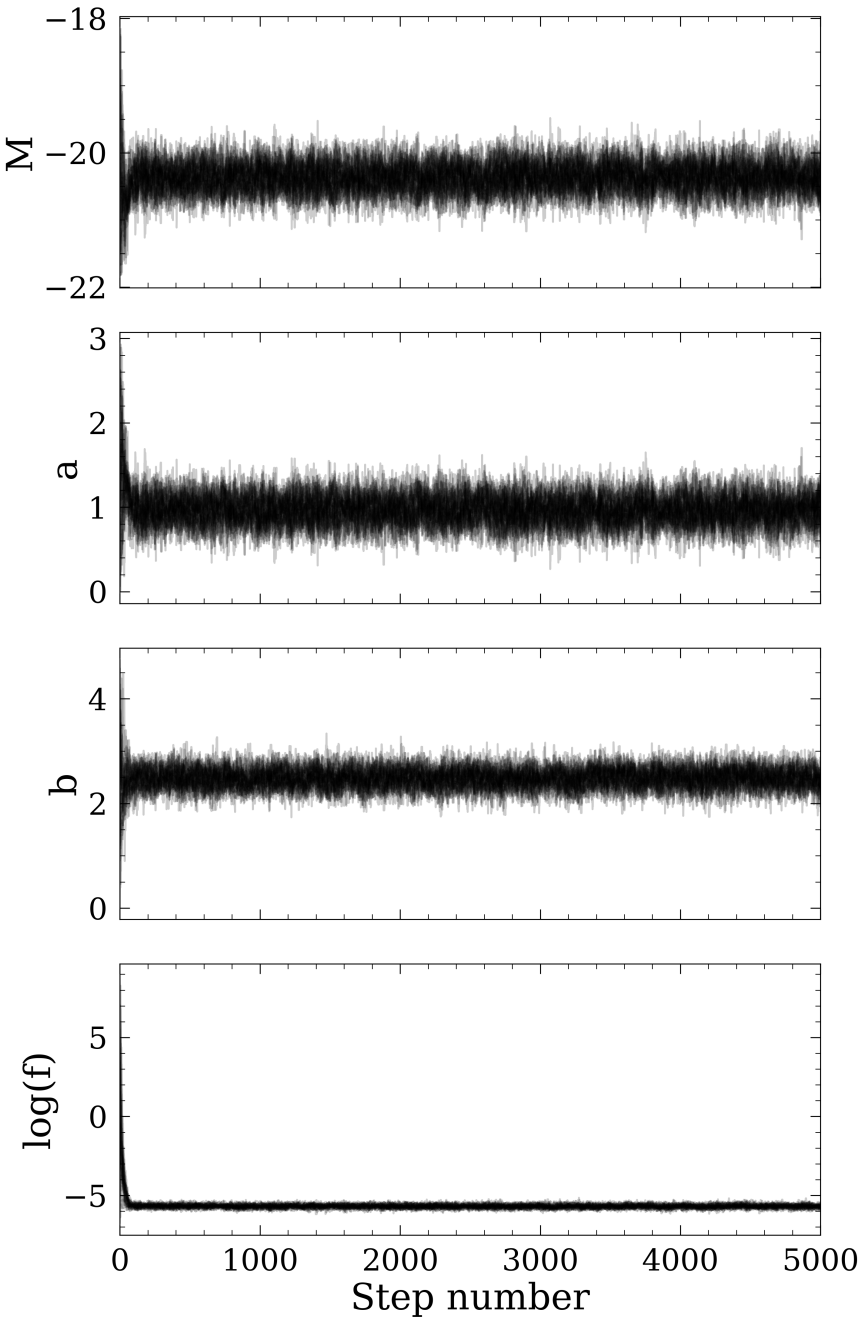

Figure C.6: The same as Figure C.2, but for the F R(Ni II) distance modulus model (Equation 3.30).

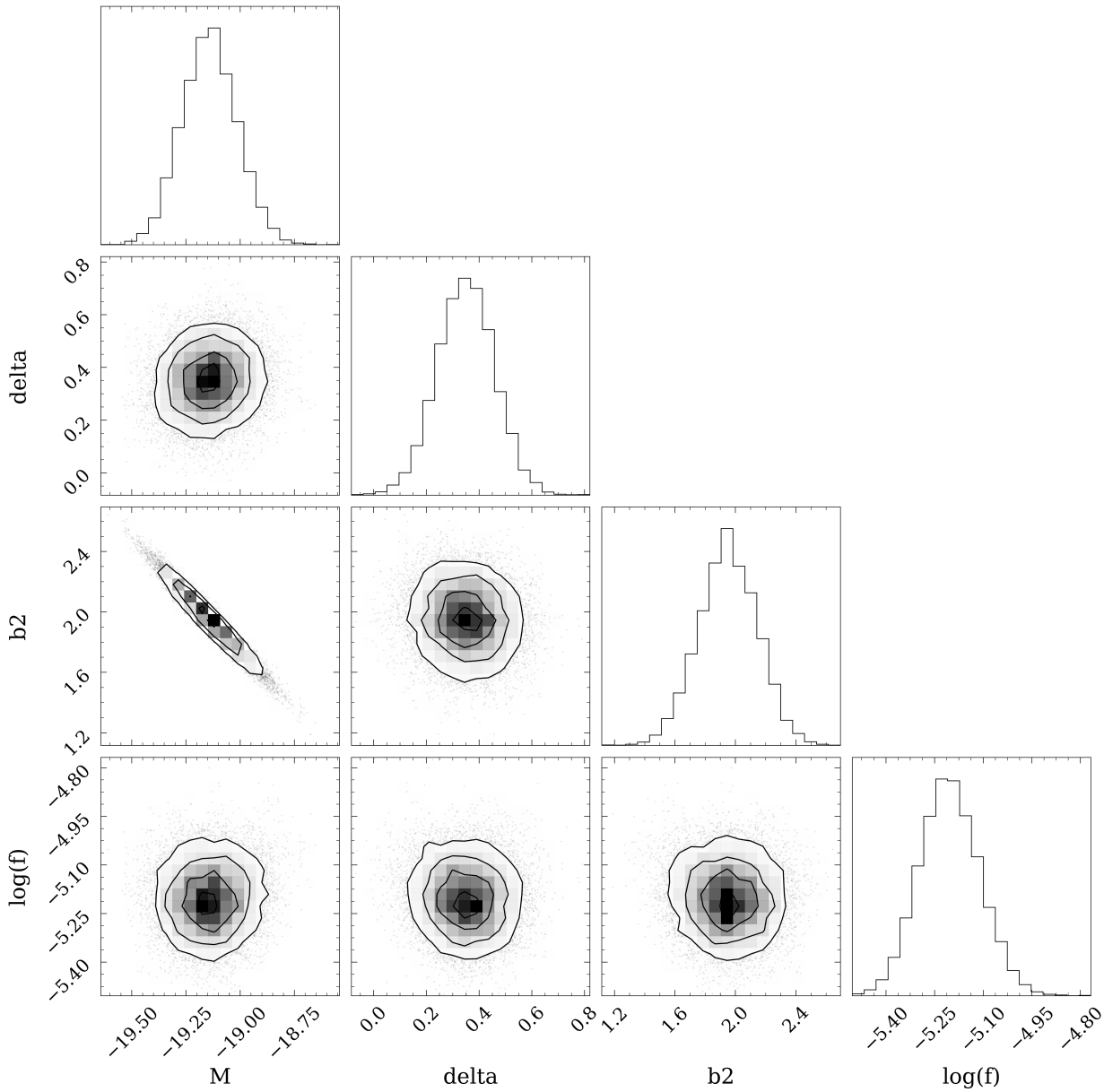

Figure C.7: The same as Figure C.1, but for the H18 distance modulus model (Equation 3.31.

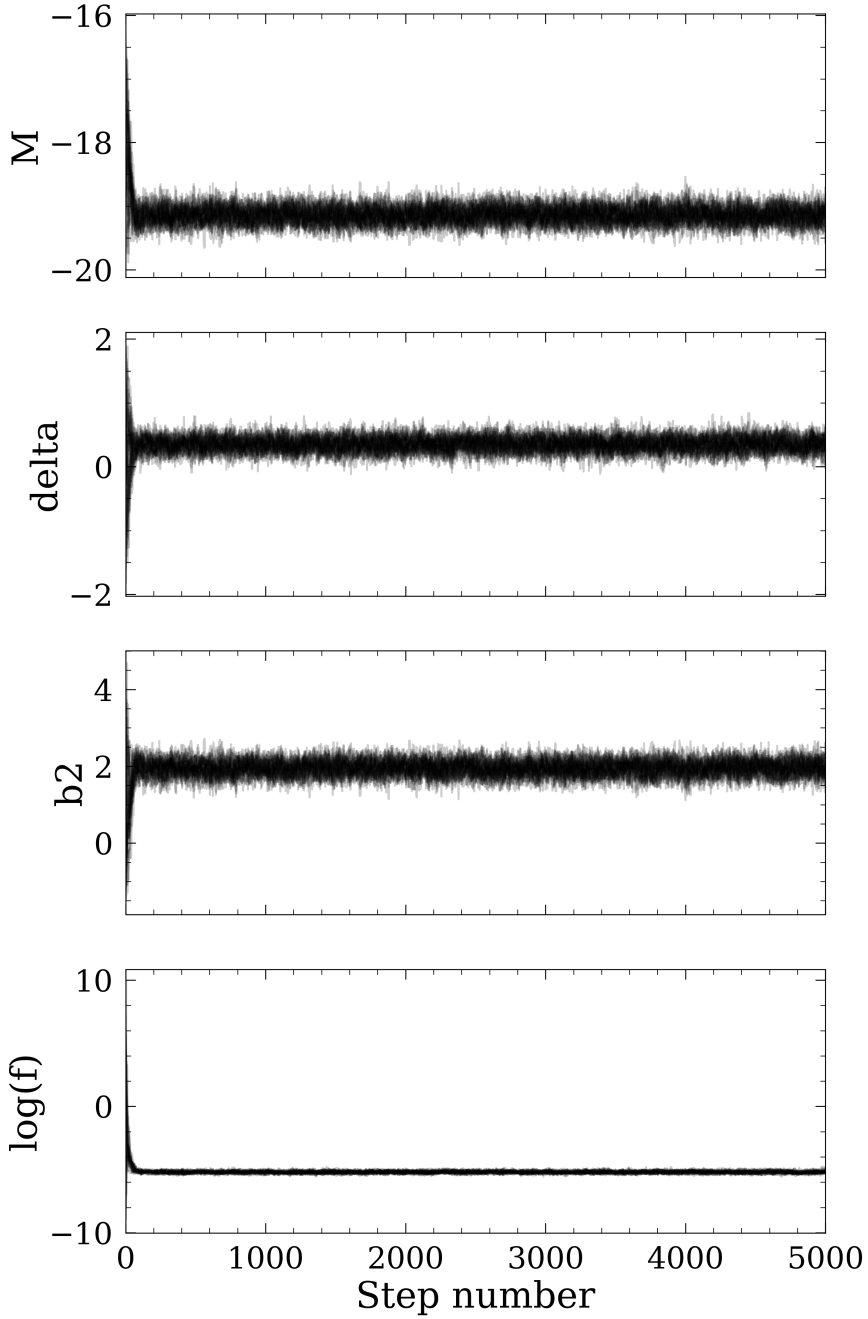

Figure C.8: The same as Figure C.2, but for the H18 distance modulus model (Equation 3.31.

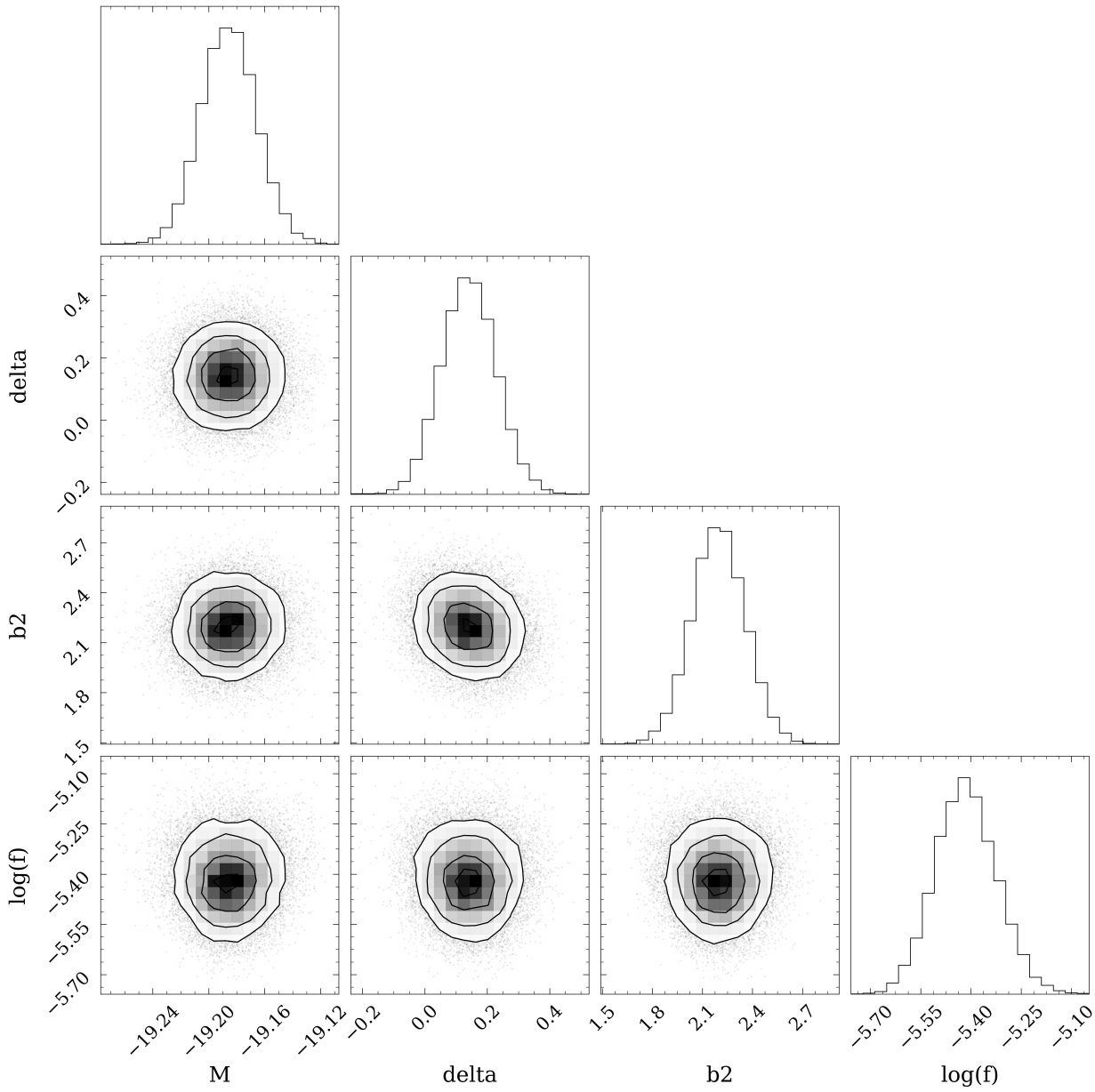

Figure C.9: The same as Figure C.1, but for the A23 distance modulus model (Equation 3.32.

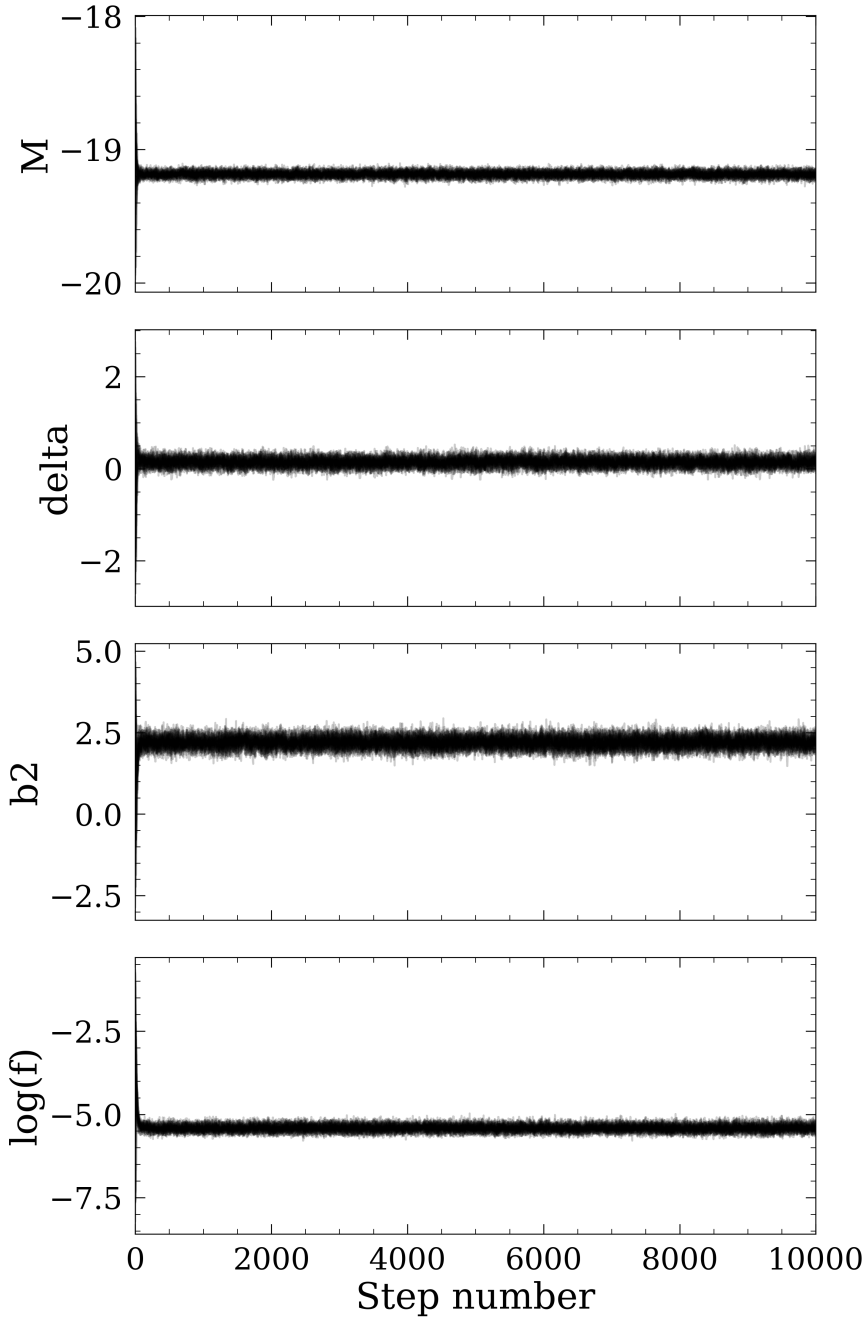

Figure C.10: The same as Figure C.2, but for the A23 distance modulus model (Equation 3.32).

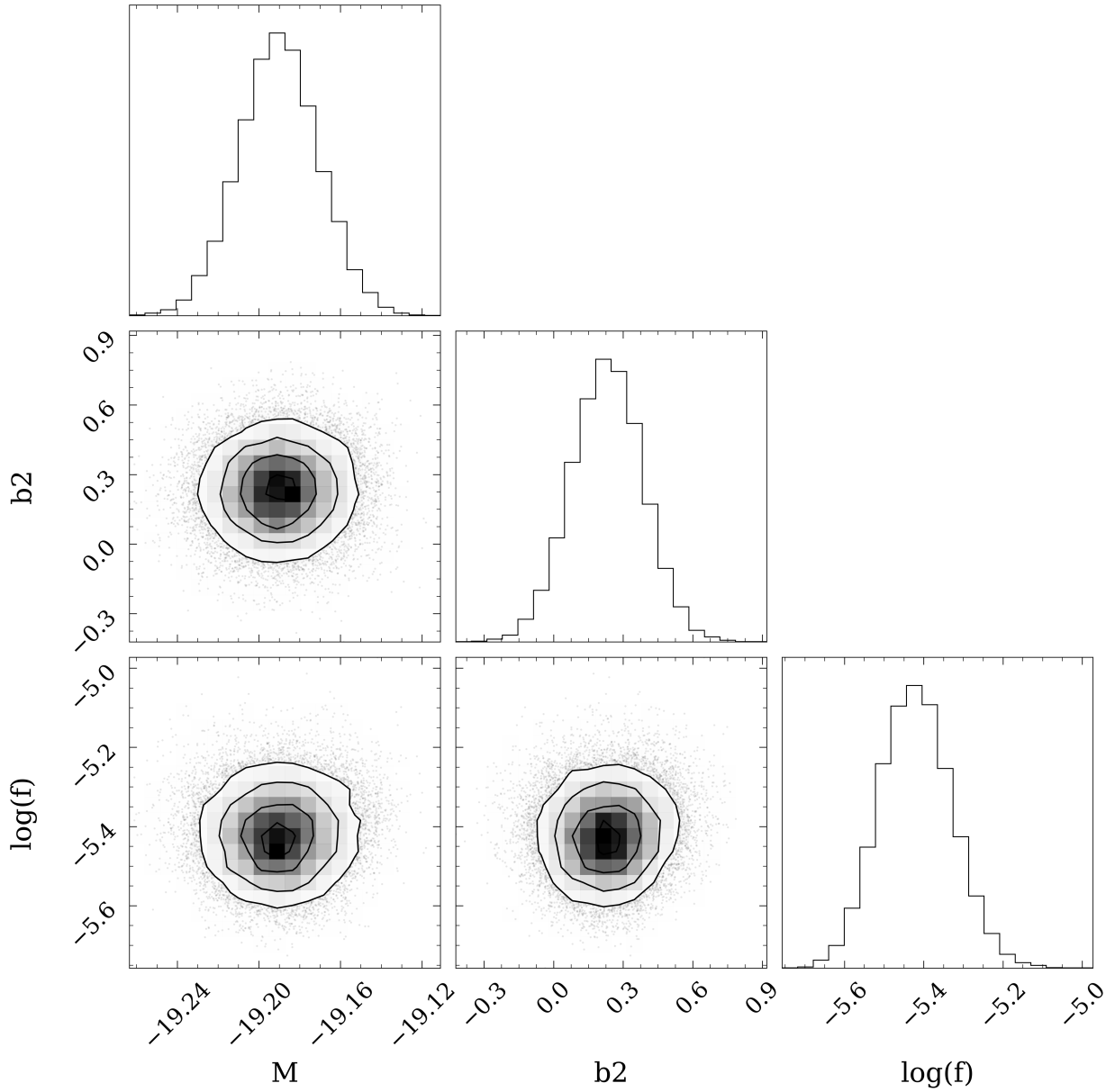

Figure C.11: The same as Figure C.1, but for the decline rate-free CMAGIC distance modulus model (Equation 3.33).

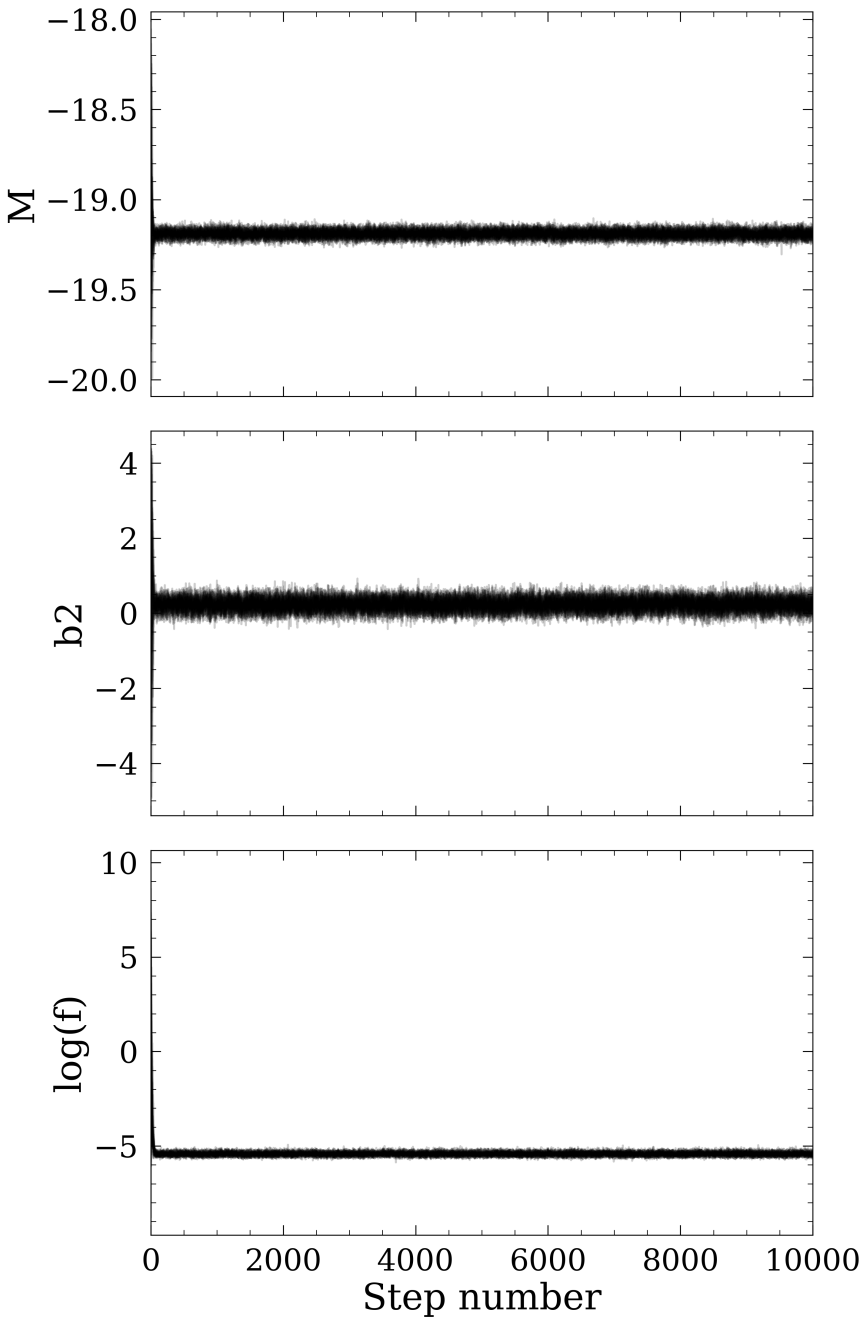

Figure C.12: The same as Figure C.2, but for the decline rate-free CMAGIC distance modulus model (Equation 3.33.